

---

ETD Archive

---

2019

# Design, Control, and Optimization of Robots with Advanced Energy Regenerative Drive Systems

Poya Khalaf

Follow this and additional works at: <https://engagedscholarship.csuohio.edu/etdarchive>

 Part of the [Mechanical Engineering Commons](#)

**How does access to this work benefit you? Let us know!**

---

## Recommended Citation

Khalaf, Poya, "Design, Control, and Optimization of Robots with Advanced Energy Regenerative Drive Systems" (2019). *ETD Archive*. 1125.

<https://engagedscholarship.csuohio.edu/etdarchive/1125>

This Dissertation is brought to you for free and open access by EngagedScholarship@CSU. It has been accepted for inclusion in ETD Archive by an authorized administrator of EngagedScholarship@CSU. For more information, please contact [library.es@csuohio.edu](mailto:library.es@csuohio.edu).

**DESIGN, CONTROL, AND OPTIMIZATION OF  
ROBOTS WITH ADVANCED ENERGY  
REGENERATIVE DRIVE SYSTEMS**

**POYA KHALAF**

**Bachelor of Science in Mechanical Engineering**

**Shiraz University**

**August 2010**

**Master of Science in Mechanical Engineering**

**Iran University of Science and Technology**

**August 2012**

submitted in partial fulfillment of requirements for the degree  
**DOCTOR OF PHILOSOPHY IN MECHANICAL ENGINEERING**

at the

**CLEVELAND STATE UNIVERSITY**

**MAY 2019**

We hereby approve this dissertation for  
POYA KHALAF  
Candidate for the Doctor of Philosophy in Mechanical Engineering degree  
for the Department of Mechanical Engineering  
and the CLEVELAND STATE UNIVERSITY'S  
College of Graduate Studies by

---

Hanz Richter, Ph.D, Dissertation Committee Chairperson  
Department of Mechanical Engineering

---

Antonie van den Bogert, Ph.D, Dissertation Committee Member  
Department of Mechanical Engineering

---

Eric Schearer, Ph.D, Dissertation Committee Member  
Department of Mechanical Engineering

---

Dan Simon, Ph.D, Dissertation Committee Member  
Department of Electrical Engineering and Computer Science

---

Ulrich Zurcher, Ph.D, Dissertation Committee Member  
Department of Physics

Date of Defense: March 6, 2019

This student has fulfilled all requirements for the Doctor of Engineering degree

---

Chandra Kothapalli, Ph.D, Doctoral Program Director

## ACKNOWLEDGMENTS

I would like to thank my adviser, Dr. Hanz Richter, for his support and guidance during my time at Cleveland State University. Dr. Richtre, I have learned so much from you and have grown as an engineer and as a person. I am forever grateful to have had you as my academic and life mentor throughout these past four and half years.

I would also like to thank my committee and other faculty members that I have had the privilege of working with: Dr. Dan Simon, Dr. Antonie van den Bogert, Dr. Eric Schearer, Dr. Ulrich Zurcher, Dr. Elizabeth Hardin, and Dr. Deborah Espy. Thank you for all your knowledge and guidance.

I would like to thank the National Science Foundation for supporting this project through grants No. 1344954 and No. 1536035.

To my colleges: Holly Warner, Humberto De Las Casas Zolezzi, Erivelton Gualter dos Santos, Amin Ghorbanpour, and Santino Bianco. Its been an honor to work along side you and I wish you all the best in you future endeavors.

A big thanks to my mother, Shahnaz, father, Hossein, and sisters, Shiva and Aida, for your continuous support throughout my life. Thank you for making me the person I am today. I love and miss you all so much.

Last but not least, to my wife, Samira. There are no words that can express how grateful I am to have you in my life. I would not have been here without you. Thank you for standing beside me through the thick and thin.

# DESIGN, CONTROL, AND OPTIMIZATION OF ROBOTS WITH ADVANCED ENERGY REGENERATIVE DRIVE SYSTEMS

POYA KHALAF

## ABSTRACT

We investigate the control and optimization of robots with ultracapacitor based regenerative drive systems. A subset of the robot joints are conventional, in the sense that external power is used for actuation. Other joints are energetically self-contained passive systems that use ultracapacitors for energy storage. An electrical interconnection known as the star configuration is considered for the regenerative drives that allows for direct electric energy redistribution among joints, and enables higher energy utilization efficiencies. A semi-active virtual control strategy is used to achieve control objectives.

We find closed-form expressions for the optimal robot and actuator parameters (link lengths, gear ratios, etc.) that maximize energy regeneration between any two times, given motion trajectories. In addition, we solve several trajectory optimization problems for maximizing energy regeneration that admit closed-form solutions, given system parameters. Optimal solutions are shown to be global and unique. In addition, closed-form expressions are provided for the maximum attainable energy. This theoretical maximum places limits on the amount of energy that can be recovered. Numerical examples are provided in each case to demonstrate the results.

For problems that don't admit analytical solutions, we formulate the general nonlinear optimal control problem, and solve it numerically, based on the direct collocation method. The optimization problem, its numerical solution and an experimental evaluation are demonstrated using a PUMA manipulator with custom regenerative drives. Power flows, stored regenerative energy and efficiency are evaluated. Experimental results show that when following optimal trajectories, a reduction of about

10 – 22% in energy consumption can be achieved.

Furthermore, we present the design, control, and experimental evaluation of an energy regenerative powered transfemoral prosthesis. Our prosthesis prototype is comprised of a passive ankle, and an active regenerative knee joint. A novel varying impedance control approach controls the prosthesis in both the stance and swing phase of the gait cycle, while explicitly considering energy regeneration. Experimental evaluation is done with an amputee test subject walking at different speeds on a treadmill. The results validate the effectiveness of the control method. In addition, net energy regeneration is achieved while walking with near-natural gait across all speeds.

# TABLE OF CONTENTS

	Page
ABSTRACT	iv
LIST OF FIGURES	ix
LIST OF TABLES	xvi
I BACKGROUND AND MOTIVATION	1
1.1 Introduction . . . . .	1
1.2 Incorporating Energy Regeneration in Lower Limb Powered Prosthesis . . . . .	3
1.3 Joint-to-Joint Energy Transfer in Energy Regenerative Robots . . . . .	6
1.4 Ultracapacitors . . . . .	8
1.5 Literature Review . . . . .	9
1.6 Problem Statement . . . . .	13
1.7 Specific Aims . . . . .	14
1.8 Organization of this Dissertation . . . . .	15
II MODELING AND CONTROL FRAMEWORK FOR ROBOTS WITH REGENERATIVE DRIVE SYSTEMS	18
2.1 Introduction . . . . .	18
2.2 Manipulator Model . . . . .	19
2.3 Semi-Active and Fully-Active Joints . . . . .	19
2.4 Star and Distributed Configurations . . . . .	20
2.5 Semi-active Actuator Modeling . . . . .	20
2.6 Augmented Model . . . . .	22

2.7	Semi-Active Virtual Control Strategy . . . . .	23
2.8	Regenerated Energy . . . . .	24
III PARAMETRIC OPTIMIZATION PROBLEMS		28
3.1	Introduction . . . . .	28
3.2	Problem Formulation . . . . .	28
3.3	Optimization of the Parameter Vector . . . . .	30
	3.3.1 Optimization for a Single Semi-Active Joint . . . . .	31
	3.3.2 Optimization for All Semi-Active Joints . . . . .	34
	3.3.3 Practical Considerations . . . . .	37
3.4	Optimizing the Actuator Parameters . . . . .	38
	3.4.1 Optimizing the Gear Ratio . . . . .	38
	3.4.2 Optimization with Respect to the DC Motor Parameter	40
3.5	Simulation Studies . . . . .	40
3.6	Remarks . . . . .	49
IV TRAJECTORY OPTIMIZATION PROBLEMS		52
4.1	Introduction . . . . .	52
4.2	Some Results from the Calculus of Variations and Optimal Control Theory . . . . .	52
4.3	External Force/Moment Trajectory Optimization . . . . .	55
4.4	A More General Trajectory Optimization . . . . .	60
4.5	Linear Optimal Control Problem . . . . .	64
4.6	General Optimal Control Problem . . . . .	72
	4.6.1 Problem Formulation . . . . .	73
	4.6.2 Numerical Optimization Results . . . . .	76
4.7	Remarks . . . . .	79



V	EXPERIMENTAL EVALUATION OF OPTIMAL TRAJECTORIES FOR THE PUMA 500 ROBOT	82
5.1	Introduction . . . . .	82
5.2	Parameter Identification for the PUMA 500 Robot . . . . .	84
5.3	Experimental Setup . . . . .	88
5.4	Overview of robust passivity-based control . . . . .	89
5.5	Experimental Results . . . . .	91
5.6	Remarks . . . . .	103
VI	DEVELOPMENT AND EXPERIMENTAL EVALUATION OF A POW- ERED PROSTHETIC KNEE	106
6.1	Introduction . . . . .	106
6.2	The Regenerative Prosthesis Model . . . . .	107
6.3	Variable Impedance Control Method . . . . .	109
6.3.1	Swing Phase . . . . .	110
6.3.2	Stance Phase . . . . .	111
6.3.3	Controller Tuning Procedure . . . . .	112
6.4	The Prosthesis Prototype and Experimental Setup . . . . .	113
6.5	Test Results . . . . .	115
6.6	Remarks . . . . .	120
VII	CONCLUSION	122
7.1	Statement of Contributions . . . . .	122
7.2	Future Perspectives . . . . .	127
	APPENDICES	147
A.	Equation Derivation . . . . .	148
B.	System Models . . . . .	154

## LIST OF FIGURES

Figure		Page
1	Powered lower limb prostheses: a)Empower, b)ODYSSEY, c)Power Knee, d)Vanderbilt leg. . . . .	4
2	Phases of positive and negative power during able-bodied gait, a) knee joint, b) ankle joint. Adapted from [117]. . . . .	6
3	a) Ultracapacitor schematic b) Ragone plot for different energy storing devices. Ultracapacitors fill the gap between batteries and conventional capacitors. Adapted from [32]. . . . .	9
4	Schematic of fully-active and semi-active joints. Fully-active joints use external power for actuation, while semi-active joints are passive and have self-contained energy storage. . . . .	20
5	a) distributed configuration, b) star configuration. In the distributed configuration each semi-active joint has a separate storage element, in the star configuration all the semi-active joints are connected to a common storage element. The star configuration allows for energy transfer from one semi-active joint to another. . . . .	21
6	Bond graph of electro-mechanical semi-active joint in the distributed and star configurations. . . . .	22
7	Energy regenerative double inverted pendulum and cart system. Joint 3 is fully-active, while Joint 1 and Joint 2 are semi-active. . . . .	40
8	Reference trajectories of the double inverted pendulum and cart system.	41

9	Simulation results with the initial parameter vector and actuator parameters: top left) regenerated energy, top right) voltage ratio, lower left) power flows for Joint 1, lower right power flows for Joint 2. Distributed configuration: solid lines, star configuration: dotted lines. . . . .	43
10	Simulation results for Case 1: top left) regenerated energy, top right) voltage ratio, lower left) power flows for Joint 1, lower right power flows for Joint 2. Distributed configuration: solid lines, star configuration: dotted lines. . . . .	44
11	Sankey diagram for the external energy balance in Case 1. The overall mechanical energy is represented by $\Delta E_m$ , $\Sigma_e$ and $\Sigma_m$ are the electrical and mechanical losses respectively, $W_{act}$ is the work done by the fully-active joints, and $\Delta E_{sj}$ is the energy going to (i.e., regenerated) or coming from (i.e., consumed) the $j$ -th semi-active actuator. . . . .	45
12	Simulation results for Case 3: top left) regenerated energy, top right) voltage ratio, lower left) power flows for Joint 1, lower right power flows for Joint 2. Distributed configuration: solid lines, star configuration: dotted lines. . . . .	46
13	Sankey diagram for the external energy balance in Case 3. The overall mechanical energy is represented by $\Delta E_m$ , $\Sigma_e$ and $\Sigma_m$ are the electrical and mechanical losses respectively, $W_{act}$ is the work done by the fully-active joints, and $\Delta E_{sj}$ is the energy going to (i.e. regenerated) or coming from (i.e. consumed) the $j$ -th semi-active actuator. . . . .	47
14	Simulation results for Case 4: top left) regenerated energy, top right) voltage ratio, lower left) power flows for Joint 1, lower right power flows for Joint 2. Distributed configuration: solid lines, star configuration: dotted lines. . . . .	48

15	Sankey diagram for the external energy balance in Case 4. The overall mechanical energy is represented by $\Delta E_m$ , $\Sigma_e$ and $\Sigma_m$ are the electrical and mechanical losses respectively, $W_{act}$ is the work done by the fully-active joints, and $\Delta E_{sj}$ is the energy going to (i.e., regenerated) or coming from (i.e., consumed) the $j$ -th semi-active actuator. . . . .	48
16	Simulation results for Case 5: top left) regenerated energy, top right) voltage ratio, lower left) power flows for Joint 1, lower right power flows for Joint 2. Distributed configuration: solid lines, star configuration: dotted lines. . . . .	49
17	Sankey diagram for the external energy balance in Case 5. The overall mechanical energy is represented by $\Delta E_m$ , $\Sigma_e$ and $\Sigma_m$ are the electrical and mechanical losses respectively, $W_{act}$ is the work done by the fully-active joints, and $\Delta E_{sj}$ is the energy going to (i.e., regenerated) or coming from (i.e., consumed) the $j$ -th semi-active actuator. . . . .	50
18	Reference trajectories for the cart double pendulum system. . . . .	58
19	Simulation results for initial case with no external moments applied: top left) regenerated energy, top right) voltage ratio, lower left) power flows for Joint 1, lower right power flows for Joint 2. Distributed configuration: solid lines, star configuration: dotted lines. . . . .	59
20	Optimum moment trajectory (N.m), $\mathcal{T}_2^*$ , calculated from Eq. (4.20), that maximizes energy regeneration in Joint 2 of the cart double pendulum system. . . . .	60
21	Simulation results with the optimal moment trajectory, $\mathcal{T}_2^*$ , applied: top left) regenerated energy, top right) voltage ratio, lower left) power flows for Joint 1, lower right power flows for Joint 2. Distributed configuration: solid lines, star configuration: dotted lines. . . . .	61

22	Sankey diagram for the external energy balance with the optimal moment trajectory, $\mathcal{T}_2^*$ , applied. The overall mechanical energy is represented by $\Delta E_m$ , $\Sigma_e$ and $\Sigma_m$ are the electrical and mechanical losses respectively, $W_{act}$ is the work done by the fully-active joints, and $\Delta E_{sj}$ is the energy going to (i.e., regenerated) or coming from (i.e., consumed) the $j$ -th semi-active actuator. . . . .	61
23	Optimum motion trajectory for Joint 3, $q_3^d$ (m), that maximizes energy regeneration in Joint 1 and Joint 2. . . . .	65
24	Simulation results with optimized trajectory for Joint 3: top left) regenerated energy, top right) voltage ratio, lower left) power flows for Joint 1, lower right) power flows for Joint 2. Distributed configuration: solid lines, star configuration: dotted lines. . . . .	65
25	Sankey diagram when the trajectory of Joint 3 is optimized. The overall mechanical energy is represented by $\Delta E_m$ , $\Sigma_e$ and $\Sigma_m$ are the electrical and mechanical losses respectively, $W_{act}$ is the work done by the fully-active joints, and $\Delta E_{sj}$ is the energy going to (i.e., regenerated) or coming from (i.e., consumed) the $j$ -th semi-active actuator. . . . .	66
26	a) Example of a vehicle suspension system, used to demonstrate the linear optimal control problem for maximizing energy regeneration. b) The profile for $w$ is selected to model a bump in the road. . . . .	71
27	a) $K(t)$ derived from integrating backwards Eq. (4.65), b) $S(t)$ derived from integrating backwards Eq. (4.66). . . . .	72
28	Simulation results for seat suspension system with optimal control : top left) regenerated energy, top right) system states, lower left) voltage ratio, lower right) semi-active joint power flows. . . . .	73

29	a) The PUMA 500 robot used as a case study for finding optimal trajectories that maximize energy regeneration. Coordinate frames for modeling the PUMA robot are assigned using the Denavit-Hartenberg convention.	
	b) Starting position (Point A) and the final position (Point B) for the PUMA robot. . . . .	75
30	Optimal trajectories and controls found for the PUMA 560 robot, a) optimal trajectories from point A (starting point) to point B (final point), and from point B to point A, b) the optimal virtual controls ( $\tau^d$ ). Controls are bound between $[-175, 175]$ Nm, $[-303, 303]$ Nm and $[-167, 167]$ Nm for Joints 1, 2, and 3 respectively. . . . .	78
31	Power flows for the joints of the the PUMA 500 robot when following the optimal trajectories. Power is consumed when positive, and regenerated when negative. . . . .	79
32	Initial (Point A) and final (Point B) configurations for the three studied cases. first row) Case 1, second row) Case 2, third row) Case 3, first column) initial configuration, second column) final configuration. . . . .	83
33	Excitation trajectories found for the purpose of parameter identification.	87
34	Comparison of the measured ( $\tau_{exp}^d$ ) and modeled ( $\tau_{model}^d$ ) virtual control post optimization. . . . .	88
35	Schematic of the experimental setup. Current sensors are used to measure currents on both sides of each motor driver. Voltage on the capacitor side is measured directly via the dSPACE system. The dSPACE system is also used for controlling the robot. The motor drivers are all connected to a common ultracapacitor (star configuration). Dotted lines indicate signals, solid lines indicate wiring. . . . .	89

36	first column) Optimal reference trajectories (dotted lines) and actual trajectories (solid lines) followed by the PUMA 500 robot. Trajectories go from point $A$ to point $B$ , and vice versa. second column) Control torque commands ( $\tau^d$ ) applied to the robot joints. . . . .	93
37	Capacitor voltage for the three studied cases during the movement of the robot. . . . .	94
38	Power flows for the motor side and capacitor side of the motor driver in Case 1 for a) Joint 1, b) Joint 2 and c) Joint 3. Positive power indicates energy consumption and negative power indicates energy regeneration. The theoretical power flow is also shown for comparison. . . . .	96
39	Power flows for the motor side and capacitor side of the motor driver in Case 2 for a) Joint 1, b) Joint 2 and c) Joint 3. Positive power indicates energy consumption and negative power indicates energy regeneration. The theoretical power flow is also shown for comparison. . . . .	97
40	Power flows for the motor side and capacitor side of the motor driver in Case 3 for a) Joint 1, b) Joint 2 and c) Joint 3. Positive power indicates energy consumption and negative power indicates energy regeneration. The theoretical power flow is also shown for comparison. . . . .	98
41	Sankey diagram showing the overall energy balance for the PUMA 500 robot when following optimal trajectories in Case 1 from a) $A$ to $B$ and b) $B$ to $A$ . The overall mechanical energy of the robot is represented by $\Delta E_m$ , $\Sigma_e$ and $\Sigma_m$ are the electrical and mechanical losses respectively, $\Delta E_{Driver}$ is the energy going to (i.e., regenerated) or coming from (i.e., consumed) the motor driver. . . . .	101
42	Optimum and neighboring trajectories followed by the robot when going from point $A$ to point $B$ in Case 1. Neighboring trajectories are tested to show the effectiveness of the optimization. . . . .	102

43	Effect of chattering on energy regeneration. . . . .	103
44	Prosthetic knee prototype with ottobock triton vertical shock foot. . . .	107
45	The prosthetic leg with the regenerative drive mechanism and its bond graph representation. The first three joints of the prosthesis are actuated by the human subject and are considered fully-active. The knee joint is regenerative and considered semi-active. . . . .	108
46	Prosthetic leg system overview indicating power and information paths.	113
47	Test subject walking with the prosthesis prototype (Copyright Cleveland FES Center, Cleveland, USA). . . . .	115
48	Average knee angle for three walking speeds. The slow, preferred, and fast walking speeds are 0.6, 0.75, and 0.9 meters per second, respectively. The gray bands show one standard deviation from the average trajectories.	117
49	Power flows for the slow (0.6 <i>m/s</i> ), preferred (0.75 <i>m/s</i> ), and fast (0.9 <i>m/s</i> ) walking speeds. The gray bands show one standard deviation from the average trajectories. Positive power indicates power consumption. Negative power indicates power regeneration. . . . .	118
50	Average energy regenerated in each gait cycle for three walking speeds. Regenerated energies are reported for the capacitor side and the motor side of the motor driver. . . . .	119
51	Bond graph of electro-mechanical semi-active joint in the distributed and star configurations. . . . .	148



## LIST OF TABLES

Table		Page
I	Peak power and work done for four test subjects walking at different speeds. Negative power indicates power absorption, and positive power indicates power generation. Adapted from [117]. . . . .	7
II	Ultracapacitors provided by Maxwell Technologies [70]. . . . .	9
III	Different cases for the optimal gear ratio problem. . . . .	39
IV	Nominal values for $R$ , $a$ and $b$ taken from [17]. . . . .	77
V	Energy consumption for each joint of the PUMA 560 robot when the joints follow optimized trajectories. Positive energy indicates energy consumption, negative energy indicates energy regeneration. . . . .	80
VI	Starting and ending constraints (in joint space) for the three optimal trajectories. Trajectories start at point A ( $q_i, \dot{q}_i$ ) and terminate at time $t_f$ at point B ( $q_f, \dot{q}_f$ ). Initial and terminal joint velocities are zero for the three trajectories (i.e., $\dot{q}_i = [0, 0, 0]$ and $\dot{q}_f = [0, 0, 0]$ ). . . . .	84
VII	Measured values for $R$ and $a$ . . . . .	85
VIII	$\gamma$ values identified for the friction model. . . . .	87
IX	Energy consumption for the PUMA 500 robot when following optimal trajectories. Energy consumption is reported for the motor side and capacitor side of the motor driver when going from point $A$ to point $B$ and vice versa. Negative energy indicates energy regeneration. . . . .	99

X	Comparison of energy consumption for the PUMA 500 robot when following optimal and neighboring trajectories. Energy consumption is reported for the motor side of the motor driver when going from point <i>A</i> to point <i>B</i> in Case 1. Negative energy indicates energy being regenerated. The neighboring trajectories show a lower amount of total energy regeneration when compared to the optimal trajectory. . . . .	102
XI	Controller tuning parameters. . . . .	116

## CHAPTER I

### BACKGROUND AND MOTIVATION

#### 1.1 Introduction

Energy regeneration technologies have gained much attention due to their potential to reduce the energy consumption of modern engineering systems. Lower energy consumption allows devices to work for longer periods of time with lower operational costs. These factors are crucial in the design of systems such as electric and hybrid vehicles [66], powered prostheses [54] and exoskeletons [38], autonomous spacecraft [91], and others. The concept of energy regeneration is understood here to be the process of recovering energy that would be otherwise dissipated, and redistributing or storing it for later use.

At present, regenerative energy technologies are being used in a wide range of systems. In the automotive industry, hybrid and electric cars use regenerative braking [123], in the railway industry, high speed and underground trains are equipped with regenerative braking [77]. These technologies are also being used in excavators [60], suspension systems [124], elevators [122], and many other systems.

We are motivated by the application of regenerative technologies in robotic systems. Incorporating regenerative design features in robotic systems is justified when a significant potential for energy recovery exists. Two applications which are the main focus of this dissertation include fast-moving, multi-joint industrial robots and powered prostheses. Excess energy can be stored from the robot joints when

decelerating and reused when the robot joints are accelerating, thus reducing the overall energy consumption. For an industrial manufacturing line with many robotic systems, this can lead to a significant reduction in electric power costs. For powered prostheses, energy regeneration can increase operating times, therefore making them more practical for daily use.

In addition, robots with regenerative drive systems offer unique opportunities for joint-to-joint mechanical energy redistribution by electrical means. Strictly speaking, energy transfer among joints may naturally occur in robotic manipulators via inertial coupling. However, this kind of indirect energy transfer is governed by the structure, mass properties, and joint trajectories of the robot. In many cases, these factors are predefined and the joint-to-joint energy flow cannot be managed or controlled. For example, the structure of a Cartesian robot prevents any energy flow from one joint to another. Bidirectional power (4-quadrant) drive electronics offer the opportunity to configure pathways for joint-to-joint energy transfer and management. Excess energy regenerated from a joint decelerating can be conveyed to another joint that is accelerating and demanding energy. In a regenerative Cartesian robot, this allows for direct energy transfer between joints. Such capabilities can lead to significant reduction in the energy consumption of the overall robot.

We consider regenerative drive systems that use capacitive means for storing energy. The development of electrochemical double layer capacitors, so-called ultracapacitors or supercapacitors, in the past decade have enabled efficient means of storing and reusing energy [16]. Unlike batteries, ultracapacitors can be charged and discharged at high rates without damaging them, have considerably high power densities, are lightweight, inexpensive, and durable [55]. Because of these properties, ultracapacitors are being used in many applications involving energy regeneration [56, 85, 91, 95, 107, 125].

## 1.2 Incorporating Energy Regeneration in Lower Limb Powered Prosthesis

Normal human walking requires positive power output at the ankle and knee joints [117]. Energetically passive prostheses enable walking for people with lower limb amputations by using damping and spring-like elements [104]. Accordingly, passive prostheses cannot provide net positive energy. This results in an increase of energy consumption for amputees during walking. The literature reports a 20% increase in oxygen consumption for below knee amputees walking with different speeds on a treadmill [72], and lower walking speeds and higher levels of oxygen consumption for above and below knee amputees [113]. Powered prostheses have been shown to reduce the metabolic cost of transport by providing positive net work [4, 97, 99].

The majority of the research conducted on powered lower limb prostheses has occurred in the past decade due to enabling improvements in battery, DC motor and microcontroller technologies [61]. Although some efforts have been made to develop pneumatic [97, 106, 114] and hydraulic [19, 115] powered prostheses, for the purpose of this dissertation, we are concerned with electrically actuated powered prostheses. Here we mention the most prominent of these studies and refer the readers to the survey [116] for a more comprehensive list of papers regarding powered lower limb prosthesis.

The Power Knee (Ossur, Reykjavik, Iceland) is probably the most well known commercially available powered prosthetic knee. Since its introduction in 2007, there have been several studies comparing its performance with its passive counterparts, the C-Leg (Otto Bock, Duderstadt, Germany), and the Mauch SNS (Ossur, Reykjavik, Iceland) [36, 37, 119]. A powered prosthetic knee with an agonist-antagonist structure was developed at the MIT (Massachusetts Institute of Technology, Cambridge, MA). It reproduces natural gait while minimizing energy usage by means of series elastic elements [68, 69]. The Empower (Otto Bock, Duderstadt, Germany),



Figure 1: Powered lower limb prostheses: a)Empower, b)ODYSSEY, c)Power Knee, d)Vanderbilt leg.

previously known as the Biom (BionX Medical Technologies, Boston, Massachusetts), is a powered ankle prosthesis that was initially developed at MIT [3, 21, 35] and later acquired by Otto Bock. The SPARKy powered ankle prostheses, developed at Arizona State University (Tempe, AZ), uses elastic elements to store regenerated energy and reduce energy consumption [5, 39–42]. The research on SPARKy later led to the development of the ODYSSEY (SpringActive, Tempe, AZ). Vrije Universiteit Brussel (Brussels, Belgium) developed their powered ankle prosthesis known as the AMP Foot 2.0 [11, 12], which also uses a combination of elastic elements and electric motors to reduce energy consumption while providing the power necessary for forward propulsion. The Vanderbilt transfemoral prosthesis (Vanderbilt University, Nashville, TN) is among the first to include both a powered ankle and knee joint [61, 99, 100]. A study of the Vanderbilt prosthesis showed a reduction of 32% in metabolic energy expenditure, compared to passive transfemoral prosthesis when ascending stairs [64]. The Vanderbilt prosthesis has also been studied during activities such as upslope walking [98], and running [92]. Figure 1 shows some of the well known lower limb prosthesis designs.

One main drawback of powered prostheses that hinders their widespread use is their power consumption. For the Vanderbilt leg, which includes both a powered knee

and ankle, a walking distance of about 9-12 km and a battery life of approximately 1.8 hours of continual walking have been reported [98, 100]. The Empower ankle can provide a battery life of up to eight hours [79]. The Power Knee has a battery life of approximately twelve hours depending on usage and a charging time of three and one half hours [78]. Considering power consuming daily activities beyond the average walking pace for which these values are reported (fast walking or climbing stairs) the aforementioned powered prostheses would have to be recharged several times daily for an amputee with a moderately active lifestyle. Use of energy regeneration technologies in powered prostheses can provide longer battery life and more generous ranges of locomotion, making them more practical for daily use.

The potential to recover energy in powered lower limb prostheses can be understood by considering power flows occurring in able-bodied walking. During normal able-bodied gait, the knee has four (K1, K2, K3 and K4) and the ankle two (A1 and A2) major phases of positive and negative power [117, 118]. Figure 2 illustrates these phases, where negative power indicates power absorption (the joint acts as a brake and absorbs/dissipates power), and positive power indicates power generation (the joint acts as a motor, delivering power). The figure shows that the major power phases for the knee are negative while the majority of positive power is provided by the ankle. Table I shows the peak power and the work done for four subjects walking with different speeds. We can see that in Trial WN20A the net energy of the ankle is +32(J) while the net energy of the knee is -24(J). For Trial WN56B, these values are +25(J) and -38(J) for the ankle and knee, respectively.

In an energy regenerative powered prosthesis, the power dissipated by the knee has the potential to be stored and reused to reduce the overall energy consumption. Moreover, stored energy from the knee can be directly transferred to the ankle, thus providing pathways to manage and further reduce energy consumption. In a normal human leg, joint-to-joint energy transfer occurs through the tendons and muscles

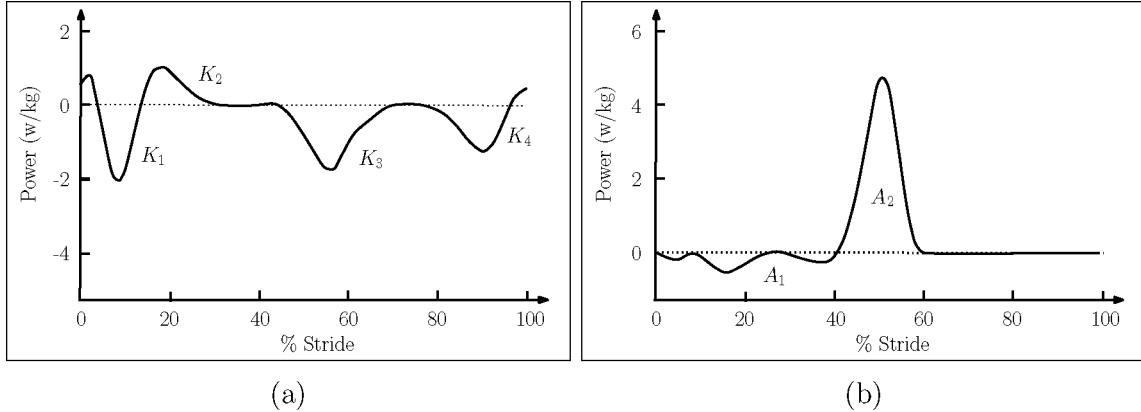


Figure 2: Phases of positive and negative power during able-bodied gait, a) knee joint, b) ankle joint. Adapted from [117].

[118], in a regenerative powered prosthesis, energy can be exchanged efficiently and directly between the prosthesis joints.

### 1.3 Joint-to-Joint Energy Transfer in Energy Regenerative Robots

Robots with regenerative drive systems offer the capability to directly manage and control energy transfer between robot joints. In a limited sense, indirect energy transfer occurs in robotic manipulators via inertial coupling. In human and animal locomotion, in addition to inertial coupling, the muscles and tendons partially transfer energy from one joint to another [118]. This kind of indirect energy flow between robot joints is governed by the structure properties of the of the system, and cannot be managed or controlled (e.g. Cartesian robot). Energy regenerative drive systems provide additional pathways to directly manage and control joint-to-joint energy transfer. Excess energy regenerated from one joint of the robot can be conveyed to another joint that is demanding energy. Such capabilities can lead to significant reductions in the energy consumption of the overall robot.

This is especially true for lower limb powered prostheses. Figure 2 and Table I show that in able bodied walking, the knee joint has excess amount of energy while the ankle joint mostly consumes energy. For example, in Trial WN21B, 14 J of energy



Table I: Peak power and work done for four test subjects walking at different speeds. Negative power indicates power absorption, and positive power indicates power generation. Adapted from [117].

Trial Code	Cadence (steps/min)	A1		A2		K1	
		Power (w)	Work (J)	Power (w)	Work (J)	Power (w)	Work (J)
<i>Fast</i>							
WN20A	124	-40	-6	340	38	-107	-6
WN56B	125	-40	-8	410	33	-180	-13
<i>Natural</i>							
WB21B	104	-40	-8	220	25	-11	-1
WN23C	97	-43	-12	170	18	-94	-7
<i>Slow</i>							
WN21H	85	-65	-8	260	37	-100	-8
WN34A	92	-55	-11	150	27	-23	-1
Trial Code	Mass (kg)	K2		K3		K4	
		Power (w)	Work (J)	Power (w)	Work (J)	Power (w)	Work (J)
<i>Fast</i>							
WN20A	78.5	85	11	-145	-24	-40	-5
WN56B	86.5	66	7	-160	-18	-140	-14
<i>Natural</i>							
WB21B	77.7	0	0	-80	-8	-50	-9
WN23C	69.0	16	1	-37	-4	-56	-7
<i>Slow</i>							
WN21H	77.7	46	5	-120	-13	-30	-6
WN34A	74.6	0	0	-100	-12	-48	-7

is consumed by the ankle and  $-18$  J of energy is dissipated by the knee. In a powered transfemoral prosthesis equipped with regenerative drive systems, the excess energy from the knee can be stored and transferred to the ankle to further reduce the energy cost of the prosthesis. In Trial WN21B, the net energy balance of the knee-ankle is  $-4$  J in one gait cycle. In other words, assuming no losses, the energy dissipated at the knee can power the ankle joint and provide a surplus of energy for certain gait patterns. However, energy regeneration has unavoidable inefficiencies which reduce

the energy advantage, but a lot is to be gained in terms of battery life by regenerating excess energy and enabling direct joint-to-joint energy transfer.

## 1.4 Ultracapacitors

Ultracapacitors, also known as supercapacitors, or electrochemical double layer capacitors, provide an efficient means of storing and reusing energy [16]. Ultracapacitors are lightweight and durable, have high power densities (i.e., high power-to-mass ratios) and the ability to rapidly charge and discharge without damage. Due to their many benefits, ultracapacitors are being used in a wide range of applications involving energy regeneration, including regenerative braking systems [26], electric cars and buses [76, 95], satellites [91], suspension systems [56], and many more. We use four quadrant drive systems that have ultracapacitors to store regenerated energy and also provide energy to the robot joints.

Ultracapacitors generally consist of two electrodes and an ion-permeable separator which are immersed in an electrolyte solution [9, 74, 87]. Figure 3a shows the schematic of an ultracapacitor cell. The electrodes are constructed from a porous material with high specific surface area. Higher surface area electrodes, and thinner dielectrics, give ultracapacitors significantly larger capacitance and energy density compared to conventional capacitors [32]. The Ragone plot in Fig. 3b compares the power densities and energy densities of different energy storing devices. Capacitors are known for high power densities, batteries are known for high energy densities, and ultracapacitors fill the gap between batteries and conventional capacitors. Table II lists commercially available ultracapacitors provided by Maxwell Technologies.

Moreover, recent development of graphene-based ultracapacitors have demonstrated energy densities larger than 64 W-hr/kg [49]. This puts ultracapacitors close to today's lithium-ion batteries, which have energy densities 100 to 250 Whr/kg, and promises a bright future for this technology.

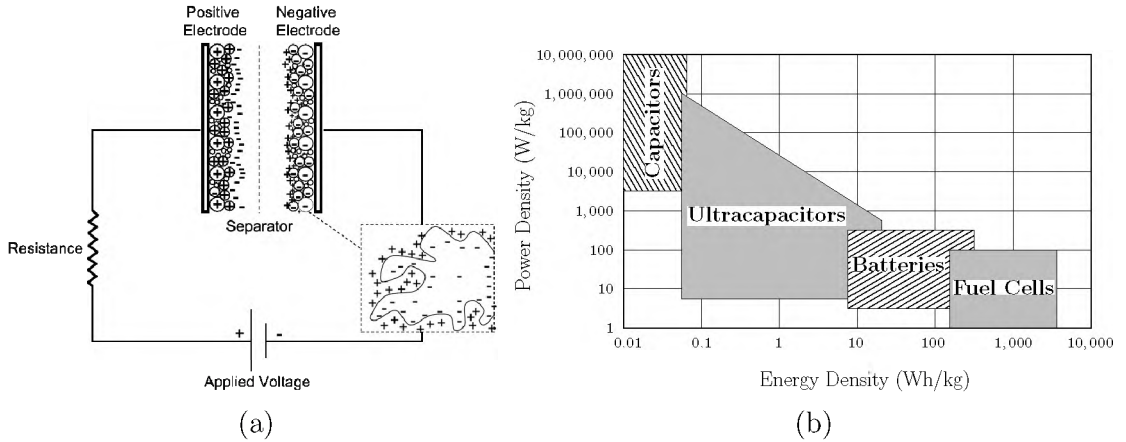






Figure 3: a) Ultracapacitor schematic b) Ragone plot for different energy storing devices. Ultracapacitors fill the gap between batteries and conventional capacitors. Adapted from [32].

Table II: Ultracapacitors provided by Maxwell Technologies [70].

Specifications	HC Series	BC Series	K2 Series	Modules
				
Capacitance (F)	1 – 150	310 – 350	650 – 3400	5.8 – 500
Voltage (V)	2.3 – 2.7	2.7	2.7 – 2.85	16 – 160
ESR <sub>DC</sub> (mΩ)	14 – 700	2.2 – 3.2	0.28 – 0.8	2.1 – 240
Leakage current (mA)	0.006 – 0.500	0.3 – 0.45	1.5 – 18	3.0 – 170
E <sub>max</sub> (Wh/kg)	0.7 – 4.7	5.2 – 5.9	4.1 – 7.4	2.3 – 4.0
P <sub>max</sub> (W/kg)	2400 – 7000	9500 – 14000	12000 – 14000	3600 – 6800

## 1.5 Literature Review

The research literature is replete with papers discussing energy regeneration and the use of ultracapacitors in systems such as road vehicles [55, 66, 95, 107], industrial electric motor drive systems [29, 30, 85], vibration control and shock absorber systems [2, 48, 56, 125], aerospace applications [91] and so on. However, research regarding use of these technologies in robotic systems is scarce. Here we offer a review of the related research and refer readers to the recent survey [10] for a more comprehensive study of the literature.

Nakamura et al. [75] aimed to reduce the energy consumption of space robot systems by storing regenerated energy as kinetic energy in a momentum wheel. The proposed approach reduces energy loss by avoiding recharging the regenerated energy back into the batteries. Numerical simulations showed that the amount of energy saved was significantly large compared with the heat loss due to electric resistance of the motors. Similarly, Gale et al. [25] investigated the feasibility of using a flywheel energy storage system (FESS) to recover otherwise dissipated energy in an six degree of freedom (DOF) robotic manipulator. The flywheel is considered as an additional joint of the robotic system and is controlled to maintain the DC bus voltage at a constant reference value. Excess mechanical energy is initially converted to electrical energy in the DC bus, and then converted back to mechanical energy to be stored in the flywheel. Only simulation results are provided and the authors point out the need for experimental evaluations to further investigate the effectiveness of the approach. Xu et al. [121] took a similar approach and simulated a crane robot that uses a FESS to recover energy.

Izumi et al. [46] considered a DC servo system capable of regenerating excess energy into a conventional capacitor. They formulated and solved a point-to-point trajectory optimization problem for this servo system by minimizing the dissipated energy. Experimental results showed storage of excess energy in the capacitor while the motor was decelerating. In a later work Izumi et al. [45] considered a two-link vertically articulated manipulator with energy regeneration. A point-to point optimal trajectory problem minimizing dissipated energy was solved for this robot. Simulation results showed that the optimal trajectory reduces energy consumption compared to the conventional non-optimized trajectory. While conventional capacitors were used, the authors pointed out the need for larger capacitances.

Fujimoto [24] found energy minimizing trajectories for bipedal running. The problem was formulated as an optimal control problem and solved numerically for a

five link planar biped robot. The analysis took into account the possibility of energy regeneration. The optimal knee trajectory showed regions of positive and negative power. Based on the optimization results it was concluded that the use of energy regeneration mechanisms, such as elastic actuators or back-drivable actuators combined with bidirectional power converters, can be used to reduce the overall energy consumption. Other works in that follow this research direction have focused on minimizing the cost of transport in bipedal and quadrupedal robots by optimizing joint trajectories, controls, and system parameters (e.g. link length, actuator placement, etc.) [8, 31, 120]. Incorporating energy regeneration into these systems can open up possibilities for further optimization in energy consumption efficiency.

Hansen et al. [33] considered a KUKA robot and found trajectories that minimize the amount of external electrical energy supplied to the motor drivers. The motor drivers are coupled together through a common DC bus, allowing power to flow from one joint of the robot to another. However their work does not include a capacitor to store excess energy. Thus energy regenerated by the robot joints is wasted unless at the same time other joints utilize the regenerated energy. The authors pointed out the use of a storage capacitor as a future development. Joint trajectories are described by B-splines and are optimized using a gradient based optimization method. Experimental results showed a 10% decrease in total energy consumption for the robot.

Seok et al. [89] present design principles for minimizing energy consumption in legged robotic systems for implementation on the MIT Cheetah robot (Massachusetts Institute of Technology, Cambridge, MA). The authors identify three main sources of energy dissipation in locomotion: actuator Joule losses, friction in the transmission, and interaction with the environment. Design principles such as using high torque density actuators, energy regenerative elements, low loss transmissions, and a low leg inertia are then devised to improve energy efficiency at the source of energy loss.

An elastic element is used in series with the motor to store recovered energy. A low impedance power flow path is also said to increase power generation and regeneration efficiency. In addition, the authors point to the trade-off in choosing the transmission ratio to reduce energy consumption, a high transmission ratio reduces the Joule losses, but at the expense of increasing losses due to friction and environment interaction.

In the powered prosthesis field, as early as the 1980s, a group at MIT developed a transfemoral prosthesis that used conventional capacitors to store regenerated energy [43, 90, 101]. They aimed to design the system so that no external power would be required for operation and the power required for the prosthesis would be regenerated during passive portions of the gait. The results suggested the use of larger capacitances, which were not available at the time.

The SPARKy powered ankle prostheses [38–40, 42], uses energy storing elastic elements in series with an electric motor to reduce peak power demand of the motor and the overall energy consumption of the system. They conclude that by tuning the spring stiffness and the transmission mechanism, the motor power can be amplified up to four times and the system’s energy consumption can be cut in half.

Tucker et al. [103] developed an analytical model of a regenerative powered transfemoral prosthesis. Energy is regenerated by controlling the actuator damping during passive regions of operation. A regeneration manifold is found that limits actuator damping that result in energy regeneration.

Everarts et al. [22] also use an elastic element in series with an electric motor, to reduce the peak power and regenerate energy, in a powered ankle prosthesis. They emphasize that a variable stiffness actuator is needed to comply with different gaits and cadences. They then proposed the use of a variable transmission in series with the motor and an elastic element to change the overall stiffness of the actuator. Simulation studies are provided to validate the approach.

Richter [81] proposed a unifying framework for modeling and control of robots

with regenerative drive systems. Based on this framework, several papers have focused on the use of evolutionary algorithms and other numerical methods to find optimal system parameters that optimize a combination of motion tracking and energy enhancing objectives [18, 20, 27, 80, 82, 84, 111, 112].

## 1.6 Problem Statement

Most of the research on energy regenerative robotic systems is concerned with specific systems and models, and the results derived from these works are not general, and cannot be directly applied to other systems and models. The framework proposed by Richter [81] enables a systematic treatment of robot motion, control, and systems optimization, with explicit consideration of energy regeneration. It is capable of capturing various regenerative actuators in various domains (electromechanical, hydraulic, etc.), that can be implemented in industrial robots, powered prostheses, and many other robotic systems. This framework is used as an underlying basis for all the results developed in this dissertation.

Based on this framework, we consider robots with regenerative electro-mechanical drive systems, where a fairly general model is used to express the dynamic behavior of the actuators. The results of this dissertation are valid for any robotic systems that can be captured by the framework and the generic actuator model.

Our goal is to explore the possibilities and limitations of robots with energy regenerative drive systems. We aim to derive bounds on the amount of energy that can be regenerated, given control and motion objectives for a robotic system. To achieve this goal, optimization problems are considered based on the aforementioned framework to find optimum robot parameters and joint trajectories that maximize energy regeneration.

When possible, closed-form solutions are sought that provide insight into the regenerative capabilities of the system, can be used as guidelines for designing efficient

energy enhancing robots, and can be applied to a wide range of robotic systems. When closed form solutions are not feasible, we resort to numerical methods to find solutions to the optimization problems.

While most efforts have focused on theory and simulations, experimental evaluations of the effectiveness of energy regeneration are very scarce in the robotics literature. We focus on two main applications, industrial robotic manipulators, and lower limb powered prosthesis, and provide experimental results to evaluate the extent to which energy regeneration can reduce the overall energy consumption of these systems.

## 1.7 Specific Aims

The objectives of this dissertation are as follows:

**Objective 1: Extend the baseline framework developed by Richter [81].** We aim to investigate possible configurations for the electrical interconnection between regenerative actuators, specifically, configurations that allow for direct joint-to-joint energy transfer. We aim to extend the baseline framework to include the new configuration, and use it to formulate optimization problems that will shed light on the advantages of different configurations, and possibilities of direct joint-to-joint energy transfer.

**Objective 2: Investigate parameter optimization problems for energy regenerative robots.** Using the extended framework, and assuming given motion trajectories, closed-form expressions are sought for the optimal manipulator parameters (link masses, link lengths, etc.) and actuator parameters (gear ratios, etc.) that maximize energy regeneration between any two times.



**Objective 3: Investigate trajectory optimization problems for energy regenerative robots.** Assuming a fairly generic model for the robot and the drive system, based on the aforementioned framework, we investigate motion and force/moment trajectories that maximize energy regeneration between any two times, given a set of system parameters.

**Objective 4: Experimentally evaluate energy regeneration in an industrial robotic manipulator.** We aim to demonstrate the results of point-to-point trajectory optimization, using the PUMA 500 robot as a case study. We also aim to evaluate the effectiveness of energy regeneration, by preparing an experimental setup, and measuring power flows at key locations. Moreover, a definition for quantifying the effectiveness of energy regeneration needs to be developed.

**Objective 5: Design, control, and experimentally evaluate an energy regenerative powered transfemoral prosthesis.** The prosthesis prototype, in addition to providing natural gait for the amputee, should reduce energy consumption of the prosthesis, by explicitly considering energy regeneration in both hardware and control design.

## 1.8 Organization of this Dissertation

Chapter II presents the framework developed in [81] for analyzing robots with regenerative drive systems. We extend this framework to include a configuration for direct joint-to-joint energy transfer, and provide equations expressing the amount of energy regenerated. This chapter provides the underlying basis for the optimization problems formulated in subsequent chapters.

Chapter III formulates and solves several parameter optimization problems pertaining to energy regenerative robots. Assuming the robot follows predefined

trajectories, closed-form expressions are found for the robot and actuator parameters, that maximize energy regeneration. Optimal solutions are shown to be global and unique. In addition, closed-form expressions are provided for the maximum attainable energy, which places a theoretical limit on the amount of energy that can be recovered.

Chapter IV considers trajectory optimization problems for robots with energy regeneration. Optimization problems are formulated using the aforementioned framework to maximize energy regeneration assuming given system parameters. Closed-form solutions are obtained for the optimal external force/moment trajectory. Also, a more general trajectory optimization problem is studied which maximizes energy regeneration with respect to any variable satisfying a set of conditions. For each problem, the solutions are shown to be global and unique. Explicit expressions for the maximum attainable energy regeneration are derived, and simulation examples are provided to demonstrate the results. Furthermore, we solve the linear optimal control problem, where closed-form solutions are provided for linear time invariant systems. We also consider the general nonlinear optimal control problem, for cases where the robotic system cannot be modeled linearly. In the general case, deriving closed-form analytical solutions is not always possible, and numerical methods must be used to find the optimal solution. The PUMA 500 robot is used as a case study to demonstrate the results.

Chapter V presents the experimental evaluation of optimal trajectories which maximize energy regeneration for the PUMA 500 robot. The nonlinear optimal control problem formulated in Chapter IV is solved numerically, using an experimentally identified model for the robot. Optimal trajectories are implemented on the PUMA robot via a robust control method. An experimental setup is provided to measure power flows and evaluate the effectiveness of energy regeneration.

Chapter VI presents the design, control, and experimental evaluation of an energy regenerative powered prosthesis. The prosthesis prototype is comprised of an

ultracapacitor based regenerative knee and a passive ankle joint. We present a new varying impedance control method that allows walking at different speeds with the prosthesis, while reducing energy consumption by regenerating energy. The prosthesis is evaluated experimentally in a clinical setting, with an amputee test subject walking on a treadmill.

## CHAPTER II

# MODELING AND CONTROL FRAMEWORK FOR ROBOTS WITH REGENERATIVE DRIVE SYSTEMS

### 2.1 Introduction

We present the framework proposed by Richter [81] for modeling, optimization, and control of serial robots with energy regenerative drive systems. Based on this framework, we consider robotic manipulators where a subset of the joints are conventional, in the sense that external power is used for actuation, while the remaining joints are energetically self-contained passive systems that use ultracapacitors for energy storage. A relatively generic model is considered that can be used to capture a wide range of drive systems in other domains (hydraulic, pneumatic, etc.). The framework also develops a control strategy known as semi-active virtual control (SVC), which provides a simple method for controlling the energy regenerative joints.

We extend the concepts of this framework to account for electrical interconnections that allow direct energy redistribution among regenerative joints. Moreover, equations for the amount of energy storage in the ultracapacitors are derived explicitly, which leads to the tractable optimization problems presented in subsequent chapters.

## 2.2 Manipulator Model

We consider general serial robots modeled with the dynamic equation:

$$D^\circ(q)\ddot{q} + C(q, \dot{q})\dot{q} + \mathcal{R}^\circ(q, \dot{q}) + g(q) + \mathcal{T} = \tau \quad (2.1)$$

where  $q$  is the  $n \times 1$  vector of joint coordinates,  $D(q)$  is the inertia matrix,  $C(q, \dot{q})$  is a matrix accounting for Coriolis and centrifugal effects,  $\mathcal{R}(q, \dot{q})$  is a general non-linear damping term,  $\mathcal{T}$  is the vector of external forces and moments reflected to the manipulator joints,  $g(q)$  is the gravity vector and  $\tau$  is the vector of joint forces and moments applied by a set of actuators.

## 2.3 Semi-Active and Fully-Active Joints

In this context, robot actuators are either conventional (termed *fully-active*) or regenerative (termed *semi-active*). A fully-active actuator is conventional in the sense that it exchanges mechanical power with the robot and draws electric power from an external source (similar to typical electric drives). On the other hand, semi-active actuators have self-contained energy storage. They are passive systems and only exchange mechanical power with the robot [81]. Figure 4 depicts the concepts of fully-active and semi-active actuators. Semi-active actuators are composed of a storage device to provide energy to the robot and possibly store excess energy, a power conversion element (PCE) to regulate power and to convert power between different domains, and a mechanical stage to interface with the robot. Without loss of generality, the first  $e$  joints of the robotic manipulator are assumed to be semi-active, while the remaining  $n - e$  joints are fully-active. In addition, for simplicity, the terms *actuators* and *joints* will be used interchangeably.

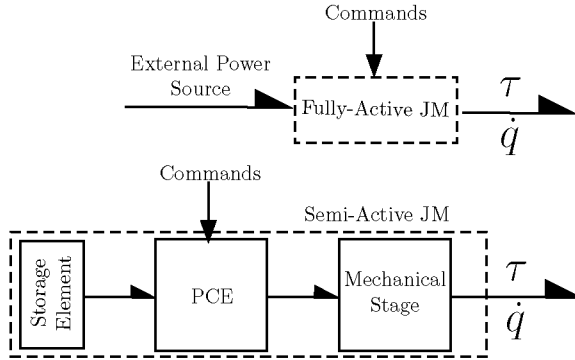


Figure 4: Schematic of fully-active and semi-active joints. Fully-active joints use external power for actuation, while semi-active joints are passive and have self-contained energy storage.

## 2.4 Star and Distributed Configurations

Depending on the arrangement of the storage elements for semi-active joints, two possible configurations are the *distributed configuration* and *star configuration*; other configurations can be a combination of these two. In the distributed configuration, each semi-active joint has a separate storage element, which is only connected to other storage elements through dynamic interaction with the robot. In contrast, in the star configuration, all the semi-active joints are connected in parallel with a single storage element. Figure 5 illustrates the distributed and star configurations for the semi-active joints. The star configuration provides a way to transfer power from one joint to another joint requiring energy using the common storage element as an energy reservoir.

## 2.5 Semi-active Actuator Modeling

Bond graphs [50] are used to facilitate the representation and equation derivation. We consider electro-mechanical semi-active actuators with an ultracapacitor as the storing element and a DC motor/generator as the PCE. The bond graph model however, can capture a wide variety of actuators in different domains (hydraulic, pneumatic, etc.). Figure 6 shows the bond graph model of the semi-active JM in both the

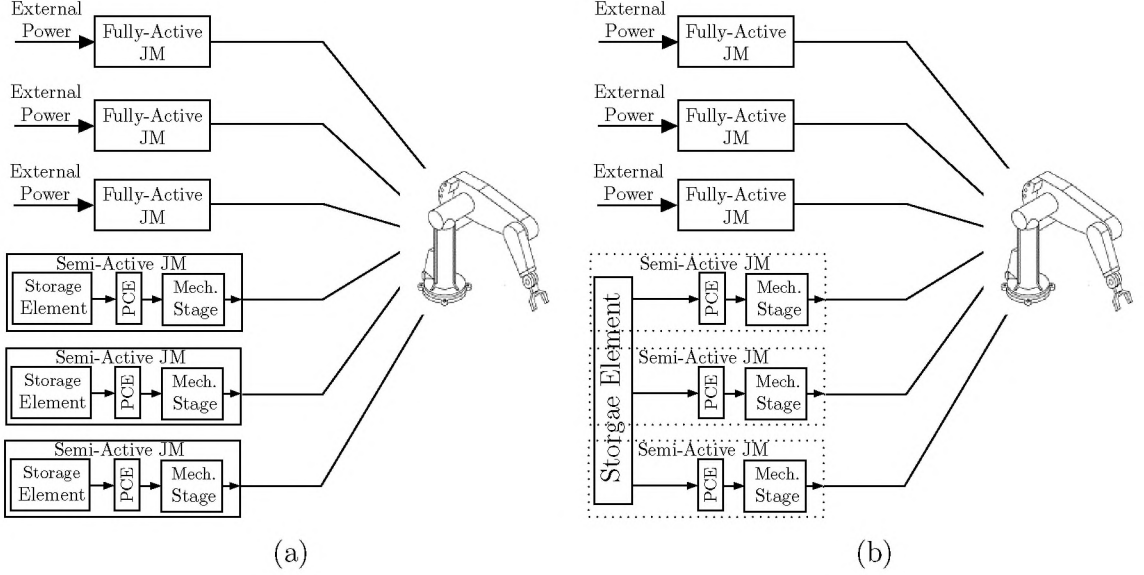


Figure 5: a) distributed configuration, b) star configuration. In the distributed configuration each semi-active joint has a separate storage element, in the star configuration all the semi-active joints are connected to a common storage element. The star configuration allows for energy transfer from one semi-active joint to another.

star and distributed configurations. Each link of the robot with a semi-active joint is connected to a transmission where  $n_j$  is the velocity ratio,  $m_j$  is the inertia, and  $b_j$  is the viscous damping coefficient. The output of the transmission is connected to a DC motor/generator with torque constant  $\alpha_j$  (which equals the back-emf constant) and resistance  $R_j$ . The inertial and frictional effects of the motor/generator are assumed to have been reflected to the link side, and already included in  $m_j$  and  $b_j$ . Note that  $b_j$  is not necessarily constant and it can be a nonlinear function. Power transferred to the electrical side of the motor/generator is distributed as resistive losses and stored energy in the ultracapacitor  $C$ . An ideal four-quadrant motor driver is used to control the amount and direction of voltage applied to the DC motor where  $r_j$  is the converter voltage ratio (motor voltage divided by capacitor voltage). Since the motor driver does not boost the capacitor voltage,  $r_j$  is assumed to be constrained to  $[-1, 1]$ . A value  $r_j < 0$  is used to apply reverse voltage to the DC motor terminals even though the capacitor voltage is always positive. Ultracapacitors typically have

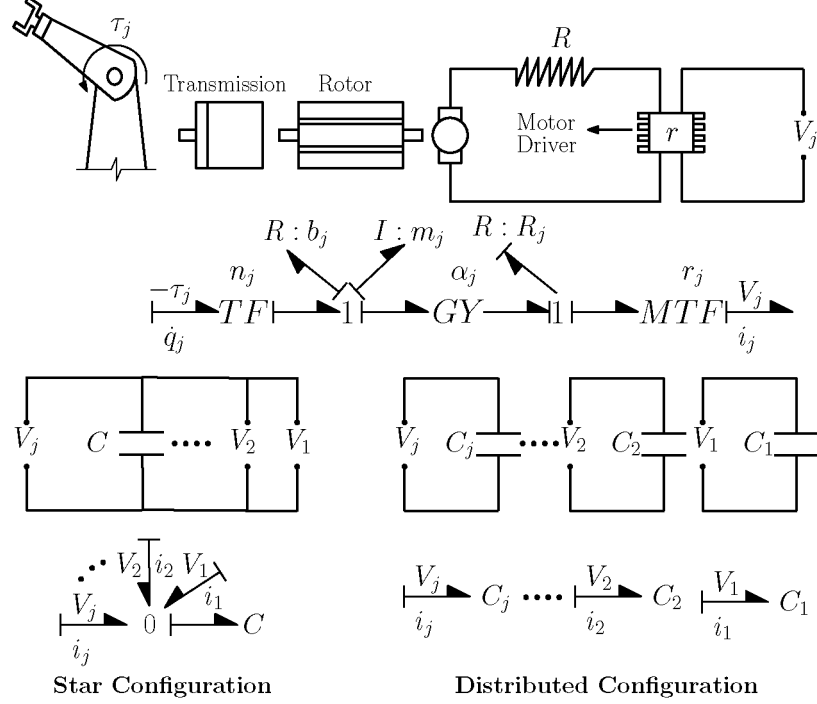


Figure 6: Bond graph of electro-mechanical semi-active joint in the distributed and star configurations.

very low internal resistances (on the order of  $\text{m}\Omega$ ), therefore we have omitted the effects of internal resistance in the capacitor model.

## 2.6 Augmented Model

The interfacing torque or force,  $\tau_j$ , for the  $j$ -th semi-active joint is derived from the bond graph model in Fig. 6 (detailed derivation can be found in Appendix A) as

$$\tau_j = -m_j n_j^2 \ddot{q}_j - (b_j n_j^2 + \frac{a_j^2}{R_j}) \dot{q}_j + \frac{a_j r_j}{R_j} V_{cap} \quad (2.2)$$

where  $a_j = \alpha_j n_j$  and  $V_{cap}$  is the capacitor voltage. For the distributed configuration,  $V_{cap}$  is the capacitor voltage of the  $j$ -th semi-active joint ( $V_{cap} = y_j / C_j$ ), and for the star configuration,  $V_{cap}$  is the voltage of the central capacitor ( $V_{cap} = y / C$ ). Replacing  $\tau_j$  from Eq. (2.2) into equation Eq. (2.1) and absorbing the terms containing  $\dot{q}$  and  $\ddot{q}$



into the right-hand side, the augmented model is obtained as

$$D(q)\ddot{q} + C(q, \dot{q})\dot{q} + \mathcal{R}(q, \dot{q}) + g + \mathcal{T} = u \quad (2.3)$$

where  $D$  and  $\mathcal{R}$  are

$$\begin{aligned} D_{ij} &= D_{ij}^\circ & i &\neq j \\ \mathcal{R}_j &= \mathcal{R}_j^\circ & j &\notin \{1, \dots, e\} \\ D_{jj} &= D_{jj}^\circ + m_j n_j^2 & j &\in \{1, \dots, e\} \\ \mathcal{R}_j &= \mathcal{R}_j^\circ + (b_j n_j^2 + \frac{a_j^2}{R_j}) & j &\in \{1, \dots, e\} \end{aligned} \quad (2.4)$$

and

$$u = \begin{cases} u_j & \text{Joint } j \text{ is fully-active} \\ \frac{a_j r_j}{R_j} V_{cap} & \text{Joint } j \text{ is semi-active} \end{cases} \quad (2.5)$$

Fully-active joints are directly controlled with  $u_j$ , which is typically an analog input voltage to a torque-mode servo amplifier. For the semi-active joints, only the voltage ratio  $r_j$  is available as a control variable. Control is achieved with the semi-active virtual control method summarized next.

## 2.7 Semi-Active Virtual Control Strategy

To control a robot with fully-active and semi-active joints, a *virtual control law* ( $\tau^d$ ) is first designed for  $u$  in the augmented model (Eq. (2.3)). For fully-active joints, this law is enforced directly, using externally-powered servo drives. For semi-active joints, the control input  $r_j$  is adjusted such that the following *virtual matching* relation holds:

$$\frac{a_j r_j}{R_j} V_{cap} = \tau_j^d \quad (2.6)$$

The virtual control ( $\tau^d$ ) can be any feedback law compatible with the desired motion control objectives for the augmented model. If virtual matching (Eq. (2.6)) holds exactly at all times, any properties that apply to the virtual design such as stability, tracking performance, robustness, etc. will be propagated to the actual system [81]. The modulation law for exact virtual matching is simply obtained by solving for  $r_j$  from Eq. (2.6). Virtual matching is always possible as long as there is a positive voltage in the capacitor, and it will hold exactly whenever  $a_j/R_j$  is precisely known, and the calculated  $r_j$  is within  $[-1, 1]$ . Also, note that the virtual control law (Eq. (2.6)) and the augmented model (Eq. (2.3)) were derived *without the need to model the ultracapacitor*. Ultracapacitor models are in general complex and nonlinear and do not cover all the aspects of the ultracapacitor’s performance [6, 7, 13, 28]. Placing the capacitor voltage in feedback of the virtual control law allows the analysis and control of ultracapacitor based dynamic systems without modeling complexities associated with ultracapacitors. Furthermore, as with any system with finite on-board power storage, operation must be stopped once charge (indicated by  $V_{cap}$ ) drops below an acceptable threshold and the system recharged. It is important to note that self-sustained operation or even charge buildup can occur, depending on system parameters and trajectories [52, 53, 81, 83].

## 2.8 Regenerated Energy

The energy regenerated or consumed by the  $j$ -th semi-active joint can be derived from the bond graph representation of Fig. 6 as

$$\Delta E_j = \int_{t_1}^{t_2} V_j i_j dt \quad (2.7)$$

where  $V_j$  is equal to the capacitor voltage  $V_{cap}$ , and

$$i_j = \frac{r_j}{R_j} (a_j \dot{q}_j - r_j V_{cap}) \quad (2.8)$$

Note again that  $V_{cap}$  is the capacitor voltage of the  $j$ -th semi-active joint in the distributed configuration, and the voltage of the central capacitor in the star configuration. Replacing for  $i_j$  and  $V_j$  in Eq. (2.7),

$$\Delta E_j = \int_{t_1}^{t_2} \frac{r_j}{R_j} (a_j V_{cap} \dot{q}_j - r_j V_{cap}^2) dt \quad (2.9)$$

Assuming exact virtual matching (Eq. (2.6)),  $\Delta E_j$  can be written in terms of  $\tau^d$  as

$$\Delta E_j = \int_{t_1}^{t_2} \left( \tau_j^d \dot{q}_j - \frac{R_j}{a_j^2} (\tau_j^d)^2 \right) dt \quad (2.10)$$

A value of  $\Delta E_j > 0$  indicates energy regeneration and  $\Delta E_j < 0$  indicates energy consumption in the specified time interval. For the distributed configuration,  $\Delta E_j$  represents the energy regenerated in the capacitor of the  $j$ -th semi-active joint, and for the star configuration, by adding the energy contributions of all the semi-active joints, the energy regenerated in the central capacitor can found as

$$\Delta E = \int_{t_1}^{t_2} \sum_{j=1}^e \left( \tau_j^d \dot{q}_j - \frac{R_j}{a_j^2} (\tau_j^d)^2 \right) dt \quad (2.11)$$

As a result of SVC, the above derivation is independent of the ultracapacitor model and is a only a function of the control law  $\tau^d$ , joint velocities  $\dot{q}$ , and joint parameters  $R$  and  $a$ . In other words, SVC decouples the dynamics of the robot and energy regeneration from the dynamics of the ultracapacitor.

In addition, by comparing Eq. (2.10) and Eq. (2.11), we can see that *the energy regenerated in the central capacitor of the star configuration, is equal to the sum*

of all energies regenerated in the capacitors of the distributed configuration. As a direct result of SVC under perfect virtual matching, the overall energy regeneration is independent of the configuration used, and is only a function of the actuator parameters  $(a_j, R_j)$ , joint trajectory  $(q_j)$ , and the designed control  $(\tau^d)$ . when choosing one configuration over the other, more practical issues such as cost, size limitations, and discharge or overcharge prevention, can be overriding factors. One clear advantage of the star configuration is the possibility of power redistribution among semi-active joints. Intuitively, power surpluses from decelerating joints may be channeled to other joints currently demanding power, thus preventing the discharge or overcharge of the capacitors, and allowing for the use of smaller capacitances in the regenerative system design.

With some algebraic manipulation detailed in Appendix A, the energy regenerated in the distributed configuration (Eq. (2.10)) can be expressed as

$$\Delta E_{sj} = \int_{t_1}^{t_2} \left( -\tau_j \dot{q}_j - \frac{dK_j}{dt} - P_{Rj} - b_j n_j^2 \dot{q}_j^2 \right) dt \quad (2.12)$$

where  $K_j$  is the kinetic energy and  $P_{Rj}$  is the power dissipated in the resistive elements of the semi-active joint. It can be inferred from this equation that the energy stored in the capacitor is a result of the work done by the interface torque  $-\tau_j$ , the change of kinetic energy of the semi-active joint and the energy dissipated in the resistive elements and mechanical friction. A similar relation can also be derived for the star configuration:

$$\Delta E_s = \int_{t_1}^{t_2} \sum_{j=1}^e \left( -\tau_j \dot{q}_j - \frac{dK_j}{dt} - P_{Rj} - b_j n_j^2 \dot{q}_j^2 \right) dt \quad (2.13)$$

where the energy stored in the central capacitor is a result of the work done by the interface torque/force, change in kinetic energy, and energy dissipation in all the

semi-active joints.

An external energy balance for the entire robotic system in both configurations can be derived as:

$$W_{act} = W_{ext} + \Delta E_m^T + \Sigma_m^T + \Delta E_s + \Sigma_e \quad (2.14)$$

where  $W_{act}$  is the work done by the fully-active joints,  $W_{ext}$  is the work done by the external forces and moments,  $\Delta E_m^T$  and  $\Sigma_m^T$  are the total mechanical energy and mechanical losses of the robot and the semi-active joints, respectively,  $\Delta E_s$  is the energy stored in the capacitor(s) and  $\Sigma_e$  represents the Joule losses of the semi-active joints. This equation shows that the energy stored in the capacitor is the net result of  $W_{act}$ ,  $W_{ext}$  and  $\Delta E_m^T$  minus all losses. The derivation of Eq.(2.14) can be found in Appendix A. In Chapter III and IV, we formulate optimization problems based on maximizing Eq. (2.10) and Eq. (2.11).

## CHAPTER III

### PARAMETRIC OPTIMIZATION PROBLEMS

#### 3.1 Introduction

Using the framework presented in Chapter II, we formulate and solve relevant parametric optimization problems related to robots with regenerative drive systems. Given joint trajectories, the energy stored in the capacitor in a time interval is maximized with respect to robot parameters (link lengths, link masses, etc.) and actuator parameters (gear ratios, etc.). Closed-form solutions are found for each problem that are shown to be strong global maxima and unique. In addition, closed-form expressions are given for the maximum attainable energy, which places a theoretical limit on the amount of energy that can be regenerated. A numerical simulation with a double inverted pendulum and cart system is provided to demonstrate the results.

#### 3.2 Problem Formulation

We aim to find optimal parameters for the robotic system that maximize energy regeneration between any two fixed time instants, assuming the virtual control,  $\tau^d$ , has been designed such that the robot joints,  $q(t)$ , asymptotically track a given reference trajectory,  $q^d(t)$ . Taking this assumption into account and using the linear

parametrization property for robotic manipulators [96], Eq. (2.1) can be expressed as

$$\tau_j = Y_j(q^d, \dot{q}^d, \ddot{q}^d)\Theta + \mathcal{T}_j \quad (3.1)$$

where  $Y_{n \times p}$  is the regressor of the augmented manipulator evaluated along reference trajectories,  $Y_j$  is the  $j$ -th row of the regressor, and  $\theta_{p \times 1}$  is the parameter vector which contains all the physical parameters of the robotic manipulator (link lengths, link masses, etc.). For clarity, when referring to the  $\theta$  parameters, we use the term *parameter vector* and when referring to the actual masses and lengths that comprise the parameter vector, we use the term *physical parameters*.

Using Eq. (3.1) in conjunction with Eq. (2.2) and Eq. (2.6), any virtual control strategy that provides asymptotic tracking of reference trajectories satisfies

$$\tau_j^d = Y_j(q^d, \dot{q}^d, \ddot{q}^d)\Theta + m_j n_j^2 \ddot{q}_j^d + (b_j n_j^2 + \frac{a_j^2}{R_j}) \dot{q}_j^d + \mathcal{T}_j \quad (3.2)$$

In addition to the parameter vector,  $\Theta$ , Eq. (3.2) also contains the parameters related to the semi-active actuators (gear ratio, torque constant, etc.), we refer to these parameters as *actuator parameters*. Two problems leading to explicit solutions with global properties are considered: i. optimization of the parameter vector  $\Theta$ , and ii. optimization of the actuator parameters  $n_j$ , and  $\frac{a_j^2}{R_j}$ . For each problem, two objective functions are considered: i. optimization for a single semi-active joint, where we aim to maximize the contribution of the  $j$ -th semi-active joint to energy regeneration, and ii. optimization for all semi-active joints, where we aim to maximize energy regeneration contribution of all semi-active joints. These two objectives are

formulated as

$$\text{Objective (i)} \quad \max \quad \Delta E_{sj} = \int_{t_1}^{t_2} \left( \tau_j^d \dot{q}_j^d - \frac{R_j \tau_j^{d2}}{a_j^2} \right) dt \quad (3.3)$$

$$\text{Objective (ii)} \quad \max \quad \Delta E_s = \int_{t_1}^{t_2} \sum_{j=1}^e \left( \tau_j^d \dot{q}_j^d - \frac{R_j \tau_j^{d2}}{a_j^2} \right) dt \quad (3.4)$$

where  $\tau^d$  is derived from Eq. (3.2). For the distributed configuration, Objective (i) is equivalent to maximizing energy regeneration in the capacitor of the  $j$ -th semi-active joint, and Objective (ii) is equivalent to maximizing the sum of energies regenerated in the capacitors of all the semi active joints. Pertinent to the star configuration, Objective (i) is equivalent to maximizing the energy regeneration contribution of the  $j$ -th semi-active joint, and Objective (ii) is equivalent to maximizing the energy regenerated in the common capacitor.

Some notations used in subsequent sections are as follows:  $G(i_1 : i_2, j_1 : j_2)$  denotes the sub-matrix of  $G$  consisting of the intersection of rows  $i_1$  through  $i_2$  and columns  $j_1$  through  $j_2$ ,  $G(i_1 : i_2, j)$  denotes the intersection of rows  $i_1$  through  $i_2$  and column  $j$ ,  $G(:, j)$  and  $G(i, :)$  denote the  $j$ -th row and  $i$ -th column of  $G$  respectively, and  $V(i : j)$  denotes the sub-vector of  $V$  consisting of elements  $i$  through  $j$ .

### 3.3 Optimization of the Parameter Vector

In this section, we investigate closed-form solutions for the optimum parameter vector maximizing Objective (i) and Objective (ii).



### 3.3.1 Optimization for a Single Semi-Active Joint

The problem is formulated as in Eq. (3.3) where  $\tau_j^d$  is obtained from Eq. (3.2).

With some algebraic manipulation, Objective (i) can be written as:

$$\Delta E_{sj} = -\frac{R_j}{a_j^2} \theta^T \mathcal{G} \theta + \left( \mathcal{H} - \frac{2R_j}{a_j^2} I \right)^T \theta + \mathcal{W}_j \quad (3.5)$$

where vector  $\mathcal{H}$  is defined as

$$\mathcal{H} = \left[ \int_{t_1}^{t_2} Y_{j1} \dot{q}_j^d dt, \int_{t_1}^{t_2} Y_{j2} \dot{q}_j^d dt, \dots, \int_{t_1}^{t_2} Y_{jp} \dot{q}_j^d dt \right]^T \quad (3.6)$$

vector  $I$  as

$$I = \begin{bmatrix} \int_{t_1}^{t_2} \left( m_j n_j^2 \ddot{q}_j + \left( b_j n_j^2 + \frac{a_j^2}{R_j} \right) \dot{q}_j^d + \mathcal{T}_j \right) Y_{j1} dt \\ \int_{t_1}^{t_2} \left( m_j n_j^2 \ddot{q}_j + \left( b_j n_j^2 + \frac{a_j^2}{R_j} \right) \dot{q}_j^d + \mathcal{T}_j \right) Y_{j2} dt \\ \vdots \\ \int_{t_1}^{t_2} \left( m_j n_j^2 \ddot{q}_j + \left( b_j n_j^2 + \frac{a_j^2}{R_j} \right) \dot{q}_j^d + \mathcal{T}_j \right) Y_{jp} dt \end{bmatrix} \quad (3.7)$$

matrix  $\mathcal{G}$  as

$$\mathcal{G} = \begin{bmatrix} \int_{t_1}^{t_2} Y_{j1}^2 dt & \cdots & \int_{t_1}^{t_2} Y_{j1} Y_{jp} dt \\ \vdots & \ddots & \vdots \\ \int_{t_1}^{t_2} Y_{jp} Y_{j1} dt & \cdots & \int_{t_1}^{t_2} Y_{jp}^2 dt \end{bmatrix} \quad (3.8)$$

and  $\mathcal{W}_j$  as

$$\begin{aligned} \mathcal{W}_j = & \int_{t_1}^{t_2} \left( m_j n_j^2 \ddot{q}_j + \left( b_j n_j^2 + \frac{a_j^2}{R_j} \right) \dot{q}_j^d + \mathcal{T}_j \right) \dot{q}_j \\ & - \frac{R_j}{a_j^2} \left( m_j n_j^2 \ddot{q}_j + \left( b_j n_j^2 + \frac{a_j^2}{R_j} \right) \dot{q}_j^d + \mathcal{T}_j \right)^2 dt \end{aligned} \quad (3.9)$$

From Eq. (3.5), we can see that the objective function is quadratic in  $\theta$ , and hence the optimization problem admits a unique global maximum, provided  $\mathcal{G}$  is positive definite. A closer inspection of  $\mathcal{G}$  reveals that it has the form of a Gram

matrix. The Gram matrix is a square matrix

$$G(A_1 \cdots A_k) = [g_{\Gamma\Lambda}] \quad (3.10)$$

consisting of pairwise inner products  $g_{\Gamma\Lambda} = \langle A_\Gamma, A_\Lambda \rangle$  of elements (vectors) of a Hilbert space [34]. All Gram matrices are positive-semidefinite. If  $A_1 \cdots A_k$  are linearly independent, then the Gram matrix is positive-definite. We assume that regressor entries evaluated on trajectories are functions in  $L_2[t_1, t_2]$ , a Hilbert space with an inner product defined as

$$\langle f, g \rangle = \int_{t_1}^{t_2} f(t)g(t)dt \quad (3.11)$$

Thus  $\mathcal{G}$  is always positive-definite and invertible as long as  $Y_{j1} \cdots Y_{jp}$  are linearly independent.

Kawasaki et al. [51] show that starting from any regressor for a robotic manipulator, a minimal regressor with linearly independent columns can always be derived. This method can be applied to a single row of the regressor matrix to derive linearly independent elements  $Y_{ji}$ . Note that if any of the elements  $Y_{ji}$  are zero, then the stored energy is independent of the parameter  $\theta_i$  and the optimization problem is ill-defined. We consider the case where the optimization is with respect to the whole parameter vector, and the case where the optimization is with respect to only a part of the parameter vector.

### Optimization with Respect to the Whole Parameter Vector

From the above discussion we conclude that as long as the elements  $Y_{ji} \neq 0$  optimization with respect to the whole parameter vector is well defined and admits a unique global maximum. By taking the derivative of Eq. (3.5) with respect to  $\theta$  and

equating it to zero, the optimal parameter vector,  $\theta^*$ , is obtained as

$$\theta^* = \frac{a_j^2}{2R_j} \mathcal{G}^{-1} \left( \mathcal{H} - \frac{2R_j}{a_j^2} I \right) \quad (3.12)$$

Replacing  $\theta^*$  into Eq. (3.5), we can find the maximum attainable energy regeneration as

$$\Delta E_{sj}^* = \frac{a_j^2}{4R_j} \left( \mathcal{H} - \frac{2R_j}{a_j^2} I \right)^T \mathcal{G}^{-1} \left( \mathcal{H} - \frac{2R_j}{a_j^2} I \right) + \mathcal{W}_j \quad (3.13)$$

Equation (3.13) provides a limit on the maximum amount of energy that can be regenerated by varying the parameter vector. If this value is negative, capacitors will always discharge, regardless of how the parameter vector is chosen, signaling fundamental limitations (induced by the reference trajectories, external forces and actuator parameters).

### Optimization with Respect to Part of the Parameter Vector

In certain cases, varying all the elements of the parameter vector may be physically unfeasible or impractical (changing friction coefficients). In addition, the objective function might be independent of some  $\theta_i$  (pertaining to  $Y_{ji} = 0$ ). For these cases, it is necessary to consider the problem of optimizing with respect to part of the parameter vector. The parameter vector  $\theta$ , can be rearranged as  $\theta_{p \times 1} = [\bar{\theta}_{z \times 1}^T, \theta_0^T]^T$ , where  $\bar{\theta} = \theta(1 : z)$  contains the entries to be optimized.  $\mathcal{G}$  can also be partitioned as

$$\mathcal{G} = \left[ \begin{array}{c|c} \mathcal{G}_{11} & \mathcal{G}_{12} \\ \hline \mathcal{G}_{21} & \mathcal{G}_{22} \end{array} \right] \quad (3.14)$$

where  $\mathcal{G}_{11} = \mathcal{G}(1 : z, 1 : z)$ ,  $\mathcal{G}_{12} = \mathcal{G}_{21}^T = \mathcal{G}(1 : z, z + 1 : p)$ , and  $\mathcal{G}_{22} = \mathcal{G}(z + 1 : p, z + 1 : p)$ . Vector  $\mathcal{H}$  can be partitioned as  $\mathcal{H} = [\mathcal{H}_1^T, \mathcal{H}_2^T]^T$ , where  $\mathcal{H}_1 = \mathcal{H}(1 : z)$  and  $\mathcal{H}_2 = \mathcal{H}(z + 1 : p)$ . Similarly, vector  $I$  can also be partitioned as  $I = [I_1^T, I_2^T]^T$ ,

where  $I_1 = I(1 : z)$  and  $I_2 = I(z + 1 : p)$ . Equation (3.5) then becomes

$$\begin{aligned} \Delta E_{s_j} = & -\frac{R_j}{a_j^2} \bar{\theta}^T \mathcal{G}_{11} \bar{\theta} + \left( \mathcal{H}_1 - \frac{2R_j}{a_j^2} (I_1 + \mathcal{G}_{12} \theta_0) \right)^T \bar{\theta} \\ & \frac{R_j}{a_j^2} \theta_0^T \mathcal{G}_{22} \theta_0 + \left( \mathcal{H}_2 - \frac{2R_j}{a_j^2} I_2 \right)^T \theta_0 + \mathcal{W}_j \end{aligned} \quad (3.15)$$

Equation (3.15) is also quadratic in  $\bar{\theta}$ , and thus admits a global unique maximum, as long as  $\mathcal{G}_{11}$  is positive definite. Similarly,  $\mathcal{G}_{11}$  is in the form of the Gram matrix and is always positive definite if the sub-matrix of the regressor  $\bar{Y} = Y(j, 1 : z)$  has linearly independent entries. A regressor matrix satisfying these conditions is always possible to find [51]. If any of the elements of the sub-matrix  $\bar{Y}_{ji}$  are zero, then the stored energy is independent of the parameter  $\theta_i$  and the optimization problem is ill-defined. The  $\theta_i$  pertaining to zero elements of  $\bar{Y}$  should be placed in  $\theta_0$ .

Taking the derivative of Eq. (3.15) with respect to  $\bar{\theta}$  and equating to zero, the optimal parameters  $\bar{\theta}^*$  is obtained as

$$\bar{\theta}^* = \frac{a_j^2}{2R_j} \mathcal{G}_{11}^{-1} \left( \mathcal{H}_1 - \frac{2R_j}{a_j^2} (I_1 + \mathcal{G}_{12} \theta_0) \right) \quad (3.16)$$

### 3.3.2 Optimization for All Semi-Active Joints

The problem is formulated as in Eq. (3.4) where  $\tau_j^d$  is replaced from Eq. (3.2), and asymptotic tracking of reference trajectories is assumed. With some algebraic manipulation, Eq. (3.4) can be written as:

$$\Delta E_s = -\frac{1}{2} \theta^T \hat{\mathcal{G}} \theta + \sum_{j=1}^e \left( \mathcal{H} - \frac{2R_j}{a_j^2} I \right)^T \theta + \sum_{j=1}^e \mathcal{W}_j \quad (3.17)$$

where  $\hat{\mathcal{G}}$  is defined as

$$\hat{\mathcal{G}} = \begin{bmatrix} \int_{t_1}^{t_2} \mathcal{V}_1^T \mathcal{V}_1 dt & \cdots & \int_{t_1}^{t_2} \mathcal{V}_1^T \mathcal{V}_p dt \\ \vdots & \ddots & \vdots \\ \int_{t_1}^{t_2} \mathcal{V}_p^T \mathcal{V}_1 dt & \cdots & \int_{t_1}^{t_2} \mathcal{V}_p^T \mathcal{V}_p dt \end{bmatrix} \quad (3.18)$$

and vector  $\mathcal{V}_i$  as

$$\mathcal{V}_i = \left[ \left( \frac{2R_1}{a_1^2} \right)^{\frac{1}{2}} Y_{1i} \quad \cdots \quad \left( \frac{2R_s}{a_s^2} \right)^{\frac{1}{2}} Y_{ei} \right]^T \quad (3.19)$$

Similar to the previous cases, Eq. (3.17) is quadratic with respect to  $\theta$  and the problem admits a global unique maximum provided  $\hat{\mathcal{G}}$  is positive definite. Matrix  $\hat{\mathcal{G}}$  is in the form of the Gram matrix and is always positive-definite assuming linear independence of the vectors  $\mathcal{V}_i$ . Furthermore, vectors  $\mathcal{V}_i$  are the columns of the sub-matrix  $Y(1 : e, 1 : p)$ , which can always be constructed to have linearly independent columns [51]. In addition, if any of the columns of  $Y(1 : e, 1 : p)$  are zero, the objective function is independent of the parameter pertaining to that column and the optimization problem is ill-defined.

### Optimization with Respect to the Whole Parameter Vector

By taking the derivative of Eq. (3.17) with respect to  $\theta$  and equating it to zero, the optimal parameter vector,  $\theta^*$ , is obtained as

$$\theta^* = \hat{\mathcal{G}}^{-1} \left( \sum_{j=1}^e \left( \mathcal{H} - \frac{2R_j}{a_j^2} I \right) \right) \quad (3.20)$$

Replacing  $\theta^*$  into Eq. (3.17), we find the maximum regenerated energy

$$\Delta E_s^* = \frac{1}{2} \sum_{j=1}^e \left( \mathcal{H} - \frac{2R_j}{a_j^2} I \right)^T \hat{\mathcal{G}} \left( \sum_{j=1}^e \mathcal{H} - \frac{2R_j}{a_j^2} I \right) + \sum_{j=1}^e \mathcal{W}_j \quad (3.21)$$

It is worth noting that the results of this section can be extended to the case

of maximizing energy regeneration for a subset of the semi-active joints by simply changing the value of  $e$  to the number of semi-active joints of interest.

### Optimization with Respect to Part of the Parameter Vector

Similar to previous cases,  $\theta$  is rearranged as  $\theta_{p \times 1} = [\bar{\theta}_{z \times 1}^T, \theta_0^T]^T$ , where  $\bar{\theta} = \theta(1 : z)$  contains the entries to be optimized,  $\hat{\mathcal{G}}$  is partitioned according to Eq. (3.14), and the vectors  $\mathcal{H}$  and  $I$  are partitioned as before. Equation (3.17) can be written as

$$\begin{aligned} \Delta E_{sj} = & -\frac{1}{2} \bar{\theta}^T \hat{\mathcal{G}}_{11} \bar{\theta} + \left( \sum_{j=1}^e \left( \mathcal{H}_1 - \frac{2R_j}{a_j^2} I_1 \right) - \hat{\mathcal{G}}_{12} \theta_0 \right)^T \bar{\theta} \\ & -\frac{1}{2} \theta_0^T \hat{\mathcal{G}}_{22} \theta_0 + \sum_{j=1}^e \left( \mathcal{H}_2 - \frac{2R_j}{a_j^2} I_2 \right)^T \theta_0 + \sum_{j=1}^e \mathcal{W}_j \end{aligned} \quad (3.22)$$

Equation (3.22) is quadratic with respect to  $\theta$  and has a global unique maximum if  $\hat{\mathcal{G}}_{11}$  is positive definite.  $\hat{\mathcal{G}}_{11}$  is in the form of the Gram matrix and is positive definite provided the sub-matrix  $\bar{Y} = Y(1 : e, 1 : z)$  has linearly independent columns, as previously discussed this condition can always be satisfied [51]. If any of the columns of the sub-matrix  $\bar{Y}$  are zero (i.e.  $\bar{Y}_i = \bar{Y}(:, i) = 0$ ), the objective function is independent of the parameter pertaining to  $\bar{Y}_i$ , and the optimization problem is ill-defined, that parameter should be placed in  $\theta_0$ . Taking the derivative of Eq. (3.22) with respect to  $\bar{\theta}$  and equating to zero, we find the optimal parameters  $\bar{\theta}^*$  as

$$\bar{\theta}^* = \hat{\mathcal{G}}_{11}^{-1} \left( \sum_{j=1}^e \left( \mathcal{H}_1 - \frac{2R_j}{a_j^2} I_1 \right) - \hat{\mathcal{G}}_{12} \theta_0 \right) \quad (3.23)$$

A close inspection of Eq. (3.20) and Eq. (3.12) reveals a relation between the optimal parameter vector resulting from optimization of all semi-active joints (denoted by  $\theta^*$  and derived from Eq. (3.20)), and the optimal parameter vector resulting from optimization of individual semi-active joints (denoted by  $\theta_{(j)}^*$  and derived from

Eq. (3.12)):

$$\theta^* = \left( \sum_{j=1}^e \frac{2R_j}{a_j^2} \mathcal{G}_{(j)} \right)^{-1} \left( \sum_{j=1}^e \frac{2R_j}{a_j^2} \mathcal{G}_{(j)} \theta_{(j)}^* \right) \quad (3.24)$$

where the square matrix  $\mathcal{G}_{(j)}$  refers to  $\mathcal{G}$  calculated from Eq. (3.8) for the case of maximizing energy regenerated by the  $j$ -th semi-active joint. It is related to  $\hat{\mathcal{G}}$  (Eq. (3.18)) via

$$\hat{\mathcal{G}} = \sum_{j=1}^e \frac{2R_j}{a_j^2} \mathcal{G}_{(j)} \quad (3.25)$$

Equation (3.24) indicates that  $\theta^*$  is a weighted average of  $\theta_{(j)}^*$ s where the weights are  $\frac{2R_j}{a_j^2} \mathcal{G}_{(j)}$ .

### 3.3.3 Practical Considerations

Up to this point, we have provided closed-form, global, and unique solutions to the problem of finding the optimal parameter vector that maximizes energy regeneration. In some cases, however, the optimal parameter vector might not be physically realizable. The problem of finding a set of physical parameters from the parameter vector is in general nonlinear and could have one, infinite, or no solutions. To guarantee a physically realizable parameter vector, constraints could be defined; however, feasibility constraints are in general non-convex, and solving an optimization problem with a quadratic convex objective function and non-convex constraints is by definition non-convex, and inherits all the problems associated with nonlinear non-convex optimization problems (non-uniqueness, local optima, etc.).

Infeasible solutions are still of significant value, since they provide a direction in which the parameter vector can be changed in order to increase energy regeneration. Since the objective functions expressed in Eq. (3.3) and Eq. (3.4) are convex with respect to the parameter vector, moving towards the respective global optimum will always increase energy regeneration.

Infeasible solutions could also be an indication of unsuitable reference trajec-

tories and/or a poor selection of actuator parameters. Equation (3.20) shows that varying the actuator parameters can move the optimal parameter vector in the parameter space, possibly from an unfeasible region into a feasible region. Modifying the actuator parameters and reference trajectories could be an alternative approach when encountered with unfeasible solutions.

### 3.4 Optimizing the Actuator Parameters

We present and explicitly solve the problem of maximizing energy regeneration with respect to  $j$ -th semi-active joint actuator parameters. These parameters include the gear ratio  $n_j$ , and the composite parameter  $\gamma = \frac{\alpha_j}{R_j}$ , referred to as the *DC motor parameter*. For the distributed configuration, the problem is formulated as in Eq. (3.3), and for the star configuration, since the actuator parameters of the  $j$ -th joint only show up in the  $j$ -th term of Eq. (3.4), the problem is equivalent to that of the distributed configuration.

#### 3.4.1 Optimizing the Gear Ratio

Taking the derivative of Eq. (3.3) with respect to the gear ratio,  $n_j$  (note that  $a_j = \alpha_j n_j$ ), and equating to zero, we find the optimum gear ratio

$$(n_j^*)^4 = \frac{- \int_{t_1}^{t_2} \frac{2R_j}{\alpha^2} (Y_j \theta + \mathcal{T}_j)^2 dt}{\int_{t_1}^{t_2} 2m_j \ddot{q}_j \dot{q}_j + 2 \left( b_j + \frac{\alpha^2}{R_j} \right) \dot{q}_j^2 - \frac{2R_j}{\alpha^2} \left( m_j \ddot{q}_j + \left( b_j + \frac{\alpha^2}{R_j} \right) \dot{q}_j \right)^2 dt} \quad (3.26)$$



In order for an optimal gear ratio to exist, the denominator of Eq. (3.26) must be negative. Assuming this is the case, the second order condition for optimality becomes

$$\frac{d^2 \Delta E_{sj}}{dn_j^2} = 4 \left( \int_{t_1}^{t_2} \left( m_j \ddot{q}_j + \left( b_j + \frac{\alpha_j^2}{R_j} \right) \dot{q}_j \right) \dot{q}_j dt - \int_{t_1}^{t_2} \frac{2R_j}{\alpha^2} \left( m_j \ddot{q}_j + \left( b_j + \frac{\alpha^2}{R_j} \right) \dot{q}_j \right)^2 dt \right) \quad (3.27)$$

In Eq. (3.27), the expression in the parenthesis is equal to the denominator of Eq. (3.26), hence if denominator of Eq. (3.26) is negative and a solution exists for  $n_j^*$ , this solution will be a maximum. The only points where the derivative does not exist is at  $n_j = 0$  and  $n_j = +\infty$ . As  $n_j \rightarrow 0$ ,  $\Delta E_{sj} \rightarrow -\infty$ , and as  $n_j \rightarrow +\infty$ , provided the denominator of Eq. (3.26) is negative,  $\Delta E_{sj} \rightarrow -\infty$ . Therefore we conclude that when the denominator of Eq. (3.26) is negative, the optimal gear ratio calculated from Eq. (3.26) is a global maximum. In the case where the denominator of Eq. (3.26) is positive, there is no real solution for  $n_j^*$ . This implies that  $d\Delta E_{sj}/dn_j$  is either strictly positive or strictly negative. As long as the denominator of Eq. (3.26) is positive,  $d\Delta E_{sj}/dn_j$  is strictly positive and  $\Delta E_{sj}$  is an increasing function with respect  $n_j$ . In this case, a larger gear ratio will result in a larger amount of energy regeneration. Table III summarizes each of these cases. Detailed derivations of Eq. (3.26) can be found in Appendix A.

Table III: Different cases for the optimal gear ratio problem.

Denominator of Eq. (3.26) is negative	Denominator of Eq. (3.26) is positive
A solution for $n_j^*$ exists, and is a global maximum	$\Delta E_{sj}$ is an increasing function with respect to $n_j$ , a larger gear ratio will result in a more energy regeneration.

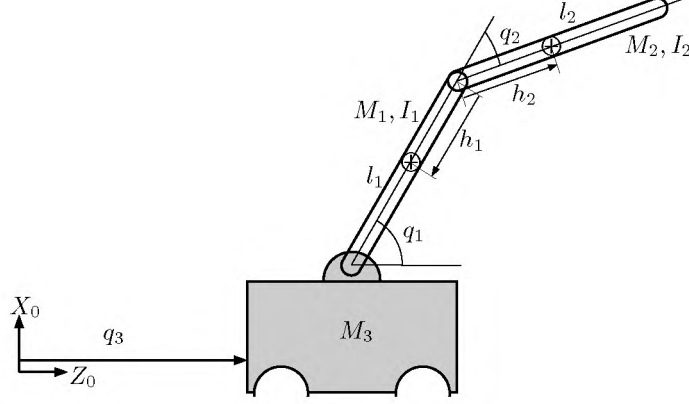


Figure 7: Energy regenerative double inverted pendulum and cart system. Joint 3 is fully-active, while Joint 1 and Joint 2 are semi-active.

### 3.4.2 Optimization with Respect to the DC Motor Parameter

Taking the derivative of Eq. (3.3) with respect to  $\gamma = \alpha^2/R_j$  and simplifying results in

$$\frac{d\Delta E_{sj}}{d\gamma} = \int_{t_1}^{t_2} \frac{1}{n_j^2 \gamma^2} (Y_j \theta + m_j n_j^2 \ddot{q}_j + b_j n_j^2 \dot{q}_j^d + \mathcal{T}_j)^2 dt \quad (3.28)$$

We see that the  $d\Delta E_{sj}/d\gamma > 0$ , indicating that  $\Delta E_{sj}$  is an increasing function with respect to  $\gamma$ , hence increasing  $\gamma$  will increase energy regeneration. This fact helps us greatly in the selection of DC machines to enhance energy regeneration.

## 3.5 Simulation Studies

To demonstrate the results of this chapter, we consider a double inverted pendulum and cart system, shown in Fig. 7. In this system,  $q_3$  is fully-active,  $q_1$  and  $q_2$  are semi-active, and no external forces or moments are applied. The regressor matrix  $Y$  and the parameter vector  $\theta$  for this system are given in Appendix B. An inverse dynamics controller [65] is used as the virtual design for asymptotic tracking. In the absence of uncertainties, inverse dynamics is a valid choice to meet the tracking objective. However, the results of this chapter are valid for any controller capable of achieving asymptotic tracking. The reference trajectories tracked by the controller

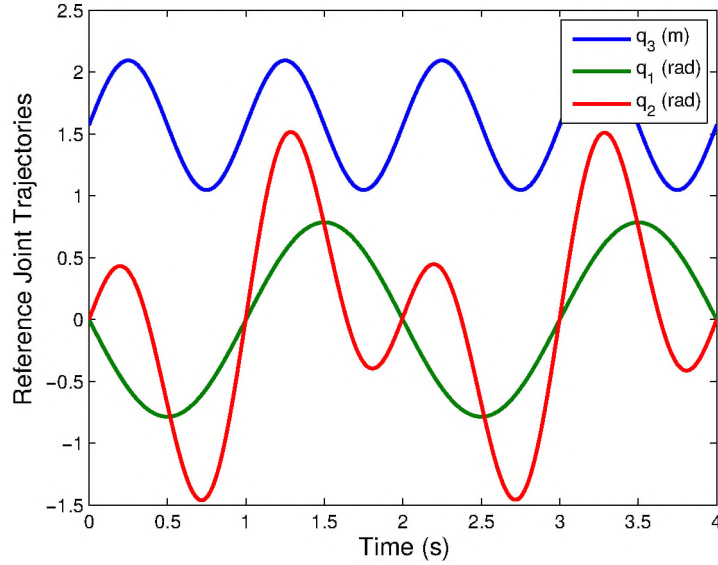


Figure 8: Reference trajectories of the double inverted pendulum and cart system.

are shown in Fig. 8. These trajectories have been chosen such that potential for energy recovery exists.

The initial parameter vector,  $\theta_0$ , for this system is

$$\theta_0 = \left[ -0.3, 0.1, 0.13, 0.05, 0.033, 0.01, 0.01, 0.01, 2.2 \right]^T \quad (3.29)$$

The actuator parameters for  $q_1$  and  $q_2$  are identical with  $R = 0.3\Omega$ ,  $\alpha = 0.0302 \text{ Nm/A}$ , and  $m = 1 \times 10^{-5} \text{ kg-m}^2$  (typical commercial values), the gear ratios are chosen to be  $n_1 = 10$  and  $n_2 = 30$ , and joint friction is assumed to be negligible.

The system is simulated with the initial parameter vector and actuator parameters in the distributed and star configurations. Figure 9 shows the regenerated energy for both configurations. Because of perfect matching in SVC, the energy regenerated in the common capacitor of the star configuration is equal to the sum of energies regenerated in the capacitors of the distributed configuration. Hence, for the sake of conciseness, we only present the energy regeneration results of the distributed configuration.

In the initial non-optimized case,  $-181.1$  J and  $-1.23$  J is regenerated by Joint 1 and Joint 2 respectively, for the period of the simulation. Note that negative energy regeneration indicates energy consumption. The converter voltage ratio ( $r$ ) for both semi-active joints and for both configurations are also shown. We can see that the capacitor voltage is sufficient to keep the voltage ratio between -1 and 1. Also, note that because of the short period of the simulation, the voltage ratio for the star and distributed configurations are almost identical. However, as the simulation time is increased, the capacitor voltages change by a significant amount, and the differences will become more clear. Power flows are computed for Joint 1 and Joint 2 in the distributed configuration based on Eq. (2.12), and are shown in Fig. 9. Negative power indicates power going from the semi-active actuator to cart pendulum system joints (power consumption), and positive power indicates power flowing from the cart pendulum system joints back to the semi-active actuator (power regeneration). Again, SVC dictates that power flows be identical for both configuration. Energy will be regenerated, when the power flowing back from the cart pendulum ( $-\tau\dot{q} > 0$ ) exceeds the losses ( $P_R$ ) and the changes in kinetic energy ( $dK/dt$ ) of the semi-active actuator. We can see from this figure that for Joint 1, excess power coming back from the cart pendulum system is all dissipated as Joule losses in the resistor, and for Joint 2, power flows back and forth between the capacitor of the semi-active actuator and the cart pendulum system.

For the first case, we maximize energy regeneration of Joint 1 ( $j = 1$ ) with respect to the first five elements of the parameter vector ( $z = 5, p = 9$ ). The optimal parameter vector is calculated directly from Eq. (3.16),

$$\theta_{case1}^* = \left[ -0.9, 0.3, 0.8, 0.3, 0.2, 0.01, 0.01, 0.01, 2.2 \right]^T \quad (3.30)$$

and simulation results are shown in Fig. 10. We can see that as a result of the

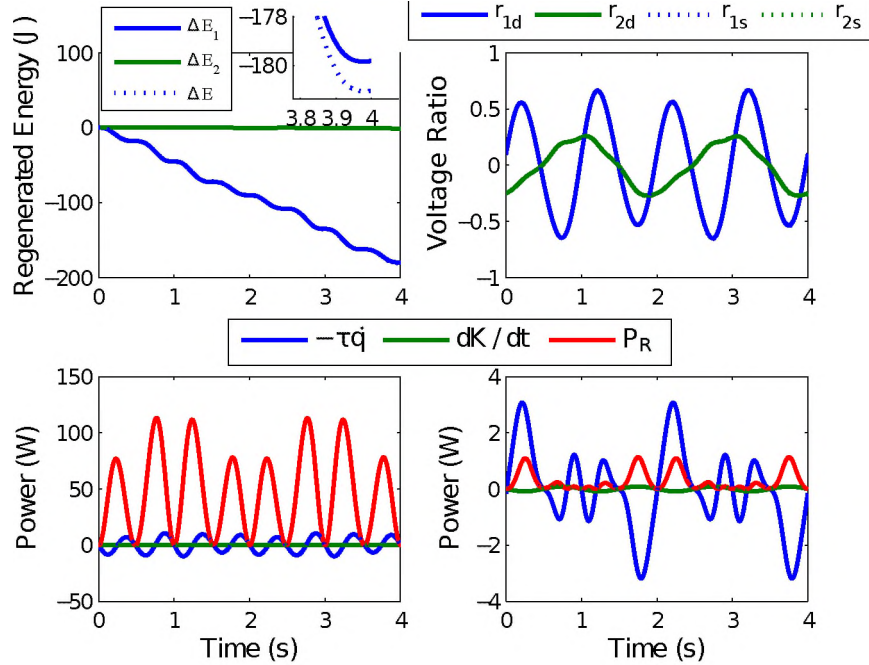


Figure 9: Simulation results with the initial parameter vector and actuator parameters: top left) regenerated energy, top right) voltage ratio, lower left) power flows for Joint 1, lower right) power flows for Joint 2. Distributed configuration: solid lines, star configuration: dotted lines.

optimization, Joule losses have decreased significantly and Joint 1 is regenerating energy, however Joint 2 is consuming energy at a faster rate compared to the previous case. At the end of simulation, Joint 1 regenerates 1.48 J, and Joint 2 regenerates  $-14.57$  J of energy.

The problem of finding physical parameters (link masses, link lengths, etc.) from the parameter vector does not admit a unique solution. For the cart pendulum system, feasibility conditions for extracting a set of realizable physical parameters

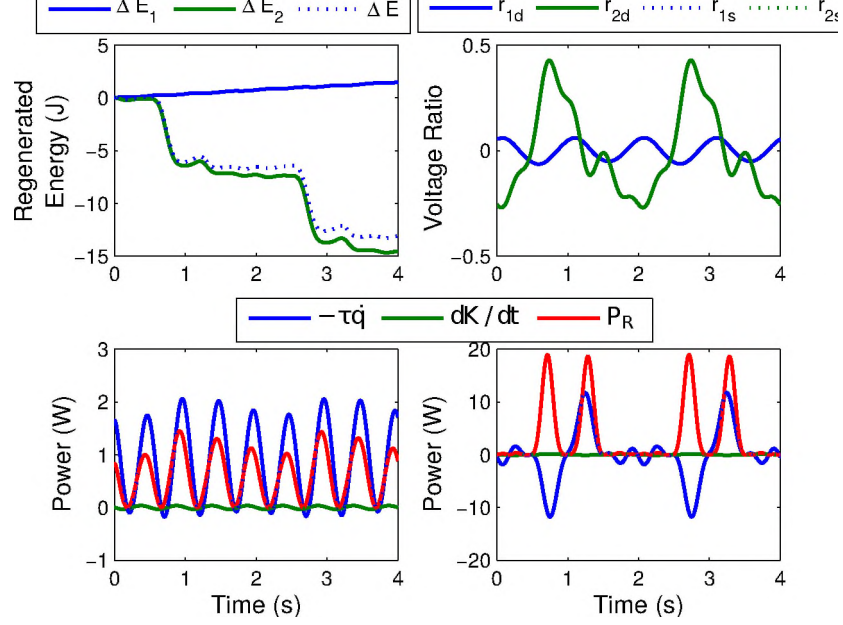


Figure 10: Simulation results for Case 1: top left) regenerated energy, top right) voltage ratio, lower left) power flows for Joint 1, lower right) power flows for Joint 2. Distributed configuration: solid lines, star configuration: dotted lines.

from the parameter vector can be derived as

$$-\theta_1\theta_5 - \theta_4\theta_2 > 0 \quad (3.31)$$

$$\theta_3\theta_5 - \theta_4^2 > 0$$

$$\theta_1 < 0$$

$$\theta(2:5) > 0$$

We can verify that  $\theta_{case1}^*$  satisfies the above conditions. After finding the physical parameters from  $\theta_{case1}^*$ , the external energy balance is calculated based on Eq. (2.14), and is shown in the Sankey diagram [102] of Fig. 11. We can see that most of the energy being injected into the system from Joint 2 and Joint 3 is being dissipated as electrical losses (86.28%) and only a small portion (7.84%) is stored in the capacitor of Joint 1.

For the second case, we maximize energy regeneration for both Joint 1 and

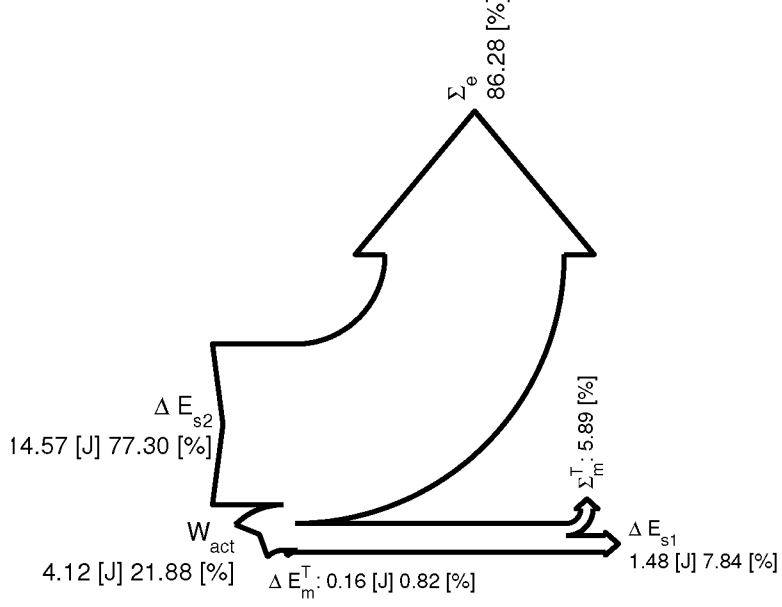


Figure 11: Sankey diagram for the external energy balance in Case 1. The overall mechanical energy is represented by  $\Delta E_m$ ,  $\Sigma_e$  and  $\Sigma_m$  are the electrical and mechanical losses respectively,  $W_{act}$  is the work done by the fully-active joints, and  $\Delta E_{sj}$  is the energy going to (i.e., regenerated) or coming from (i.e., consumed) the  $j$ -th semi-active actuator.

Joint 2 ( $e = 2$ ,  $z = 5$ ,  $p = 9$ ). The objective function is defined in Eq. (3.4), and the optimal parameters are calculated from Eq. (3.20)

$$\theta_{case2}^* = \begin{bmatrix} -0.187 & 0.071 & 0.177 & 0.075 & 0.011 & 0.01 & 0.01 & 0.01 & 2.2 \end{bmatrix}^T \quad (3.32)$$

From Eq. (3.31), we see that the parameter vector is not physically realizable. However, as explained in Section 3.3.3, the unfeasible solution provides the direction for changing the parameter vector to increase energy regeneration. To demonstrate this, we vary  $\theta_{case1}^*$  in the direction of the unfeasible parameter vector  $\theta_{case2}^*$ , until one of the feasibility conditions of Eq. (3.31) is violated. Doing so results in

$$\theta_{case3} = \begin{bmatrix} -0.324 & 0.116 & 0.299 & 0.12 & 0.048 & 0.01 & 0.01 & 0.01 & 2.2 \end{bmatrix}^T \quad (3.33)$$

Simulation results for Case 3 are shown in Fig. 12 and Fig. 13. Compared to Case 1,

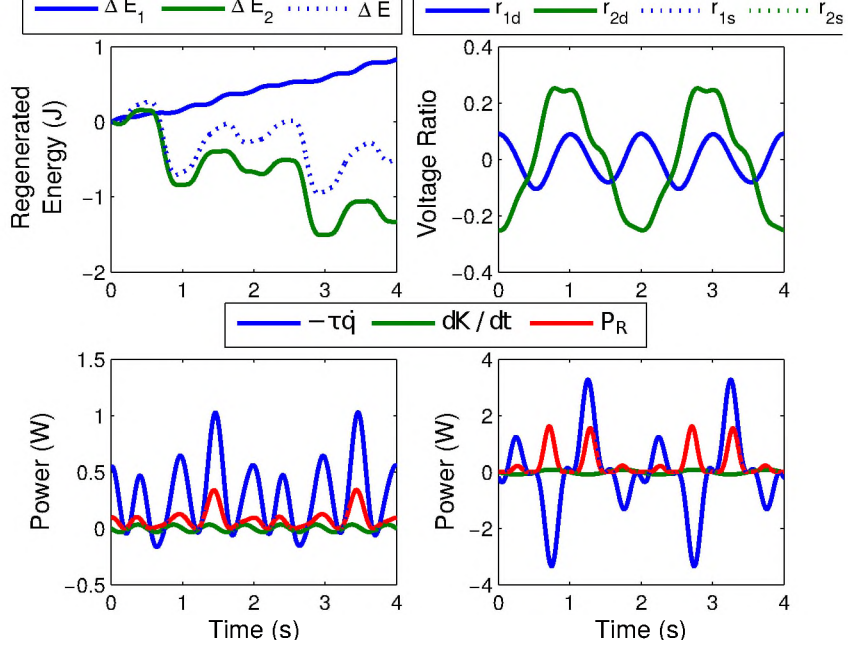


Figure 12: Simulation results for Case 3: top left) regenerated energy, top right) voltage ratio, lower left) power flows for Joint 1, lower right) power flows for Joint 2. Distributed configuration: solid lines, star configuration: dotted lines.

electrical losses for Joint 1 and Joint 2 have decreased, resulting in a significant decrease in total losses. At the end of simulation, Joint 1 and Joint 2 regenerate  $-1.82$  J and  $0.84$  J of energy respectively. The external energy input has also decreased significantly, from  $18.85$  J for Case 1 to  $3.38$  J for the current case. For Case 3, the losses consist of  $42.58\%$  of the input energy, which is a significant decrease compared to  $86.28\%$  for Case 1.

An alternative approach when facing unfeasible parameter vector solutions is varying the actuator parameters to move the optimal solution into a feasible region. For Case 4, we change the gear ratio of Joint 2 to 100. The resulting optimal parameter vector is calculated from Eq. (3.20) with  $e = 2$ ,  $z = 5$ , and  $p = 9$ ,

$$\theta_{case4}^* = \begin{bmatrix} -0.557 & 0.211 & 0.539 & 0.202 & 0.078 & 0.01 & 0.01 & 0.01 & 2.2 \end{bmatrix}^T \quad (3.34)$$

We can verify that  $\theta_{case4}^*$  satisfies the feasibility conditions. Simulation results are



shown in Fig. 14 and Fig. 15. An overall power balance shows that the electrical losses of Joint 2 have decreased compared to the previous cases. At the end of simulation, Joint 1 regenerates 1.25 J, Joint 2 regenerates  $-0.59$  J, and a total of 0.66 J of energy is gained.

The main advantage of using the star configuration over the distributed configuration is clear in this example. Using the distributed configuration results in a charge build up in the capacitor of Joint 1, and a decrease of charge in the capacitor of Joint 2. This trend will continue until the capacitor voltage of Joint 2 drops below the threshold required to maintain exact virtual control matching ( $|r| \leq 1$  in Eq. (2.6)). In the star configuration, energy regenerated by Joint 1 can be supplied to Joint 2 through the common capacitor, thus preventing violation of the virtual matching conditions, and allowing the system to work indefinitely. Note that energy is provided to the system through Joint 3, which is fully active. Also, in a real world situation, continuous charging of capacitors beyond their maximum capacity will cause damage

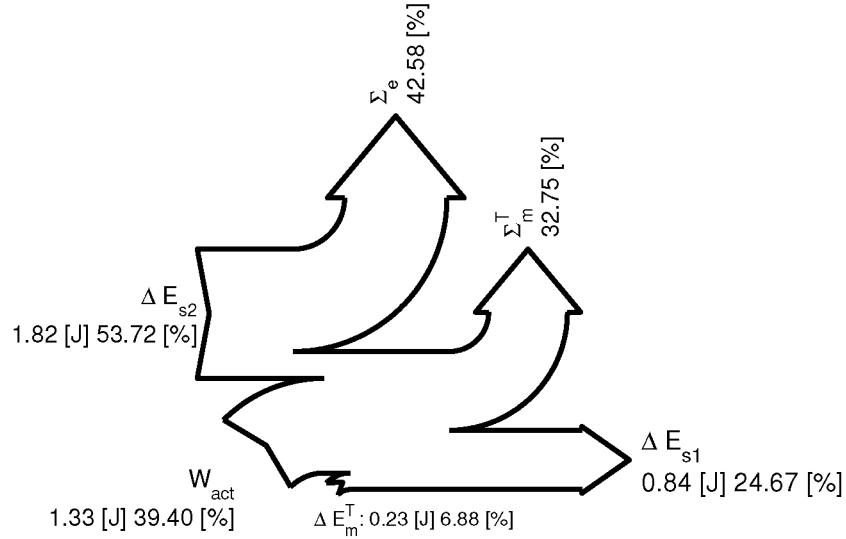


Figure 13: Sankey diagram for the external energy balance in Case 3. The overall mechanical energy is represented by  $\Delta E_m$ ,  $\Sigma_e$  and  $\Sigma_m$  are the electrical and mechanical losses respectively,  $W_{act}$  is the work done by the fully-active joints, and  $\Delta E_{sj}$  is the energy going to (i.e. regenerated) or coming from (i.e. consumed) the  $j$ -th semi-active actuator.

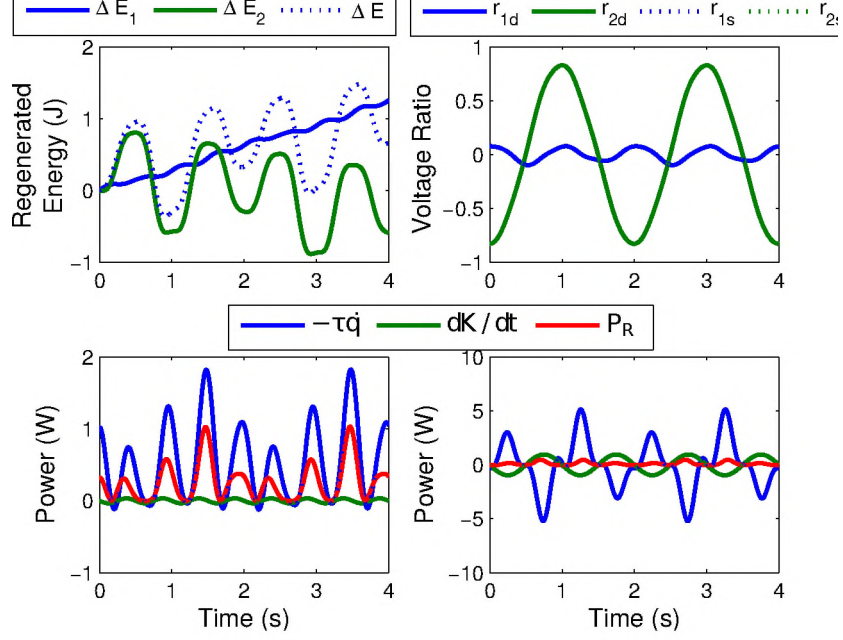


Figure 14: Simulation results for Case 4: top left) regenerated energy, top right) voltage ratio, lower left) power flows for Joint 1, lower right) power flows for Joint 2. Distributed configuration: solid lines, star configuration: dotted lines.

to them.

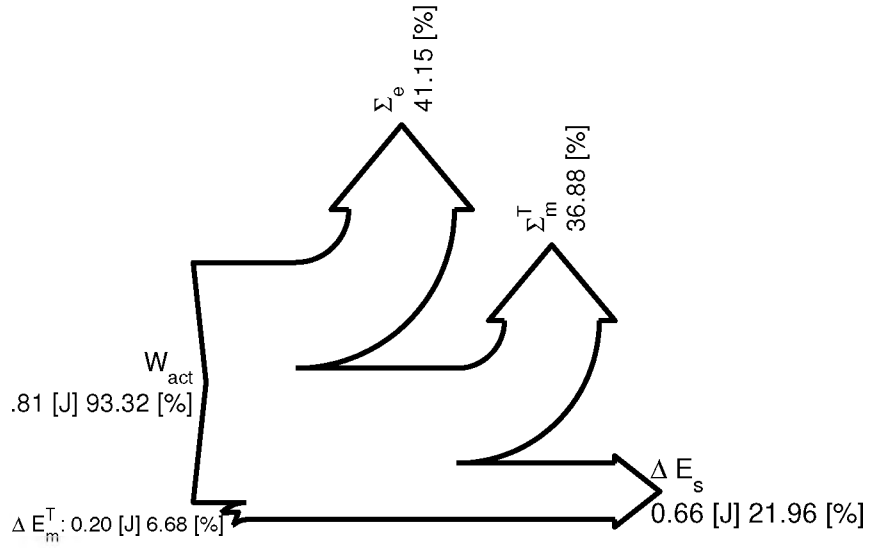


Figure 15: Sankey diagram for the external energy balance in Case 4. The overall mechanical energy is represented by  $\Delta E_m$ ,  $\Sigma_e$  and  $\Sigma_m$  are the electrical and mechanical losses respectively,  $W_{act}$  is the work done by the fully-active joints, and  $\Delta E_{sj}$  is the energy going to (i.e., regenerated) or coming from (i.e., consumed) the  $j$ -th semi-active actuator.

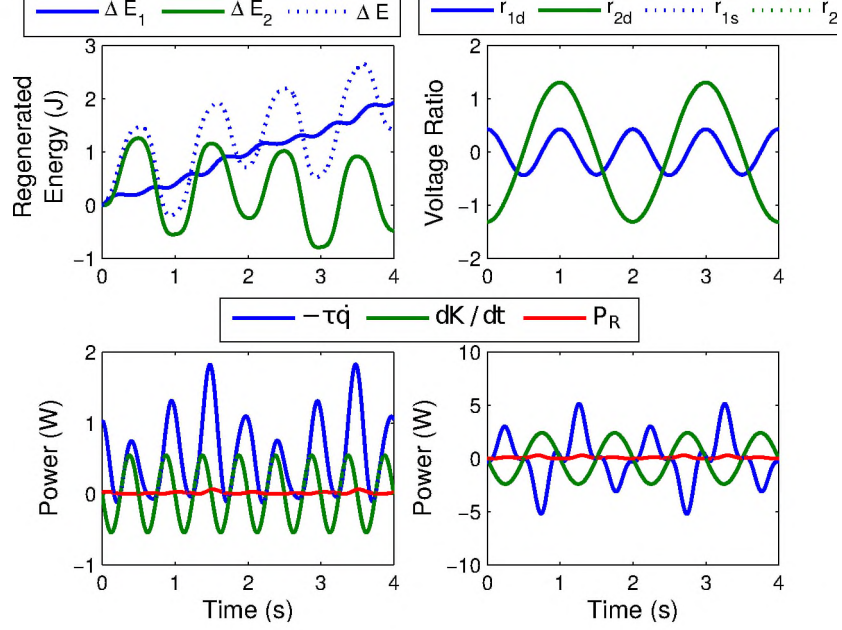


Figure 16: Simulation results for Case 5: top left) regenerated energy, top right) voltage ratio, lower left) power flows for Joint 1, lower right) power flows for Joint 2. Distributed configuration: solid lines, star configuration: dotted lines.

For Case 5, we optimize the gear ratios of Joint 1 and Joint 2. Assuming the parameter vector is equal to  $\theta_4^*$ , the optimal gear ratios are calculated from Eq. 3.26 as  $n_1^* = 39.89$  and  $n_2^* = 158.25$ . Simulation results are shown in Fig. 16 and Fig. 17. The overall power balance shows a further decrease in electrical losses compared to the previous cases. At the end of the simulation, Joint 1 and Joint 2 regenerate 1.93 J and  $-0.48$  J of energy respectively. Comparing the Sankey diagrams for Case 4 and Case 5, we see that both cases have the same input energy, however, in Case 5, the electrical losses have decreased from 41.15% to 14.98%. This 26.17% reduction in losses has been converted to an extra 26.17% of energy regeneration.

### 3.6 Remarks

In this chapter, we presented global closed-form solutions for maximizing energy regeneration with respect to the robot parameter vector or the actuator parameters. We found solutions for the star and distributed configurations, and showed that

the optimization problems under consideration are equivalent for both, but have different implications for each case. For instance, maximizing the energy regenerated in the capacitor of the  $j$ -th semi-active joint in the distributed configuration is equivalent to maximizing the energy regenerated by the  $j$ -th joint in the common capacitor of the star configuration. This is a direct result of the exact virtual matching associated with SVC. The main advantage of using the star configuration is that energy can be channeled through the common capacitor, from a joint with an excess of energy to a joint requiring energy, thus allowing for a longer periods of operation or possibly operating indefinitely.

We also saw that an optimal solution for the parameter vector does not necessarily lead to a feasible solution for the corresponding physical parameters. We can define constraints to overcome this problem, however, feasibility conditions are in general nonlinear and non-convex, and solving a convex problem with non-convex constraints is non-convex and in general hard to solve; this is a limitation of the

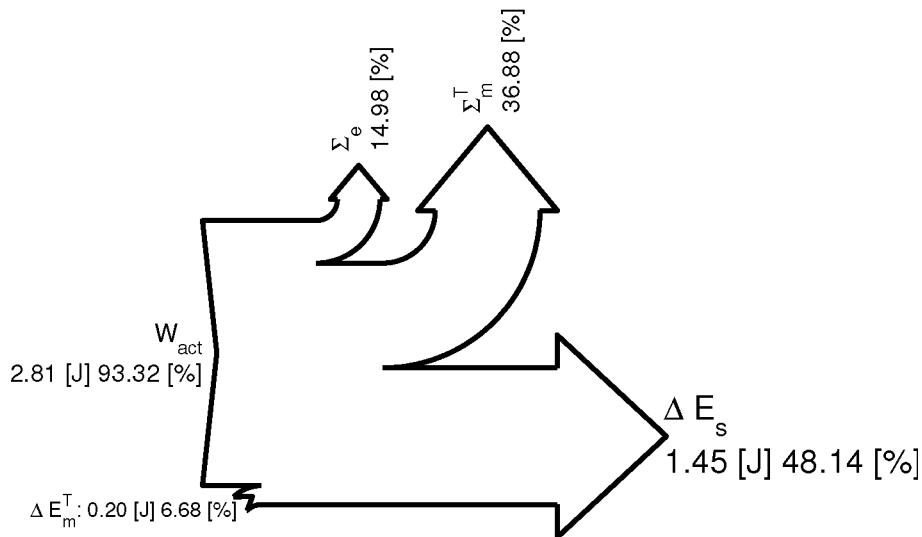


Figure 17: Sankey diagram for the external energy balance in Case 5. The overall mechanical energy is represented by  $\Delta E_m$ ,  $\Sigma_e$  and  $\Sigma_m$  are the electrical and mechanical losses respectively,  $W_{act}$  is the work done by the fully-active joints, and  $\Delta E_{sj}$  is the energy going to (i.e., regenerated) or coming from (i.e., consumed) the  $j$ -th semi-active actuator.

results. However, even when the feasibility conditions fail, the unfeasible solution provides a direction for varying the parameter vector that improves energy regeneration. In the example provided, the parameter vector is varied in the direction of the unfeasible solution until one or more of the feasibility conditions fail. The resulting parameter vector, however sub-optimal, improves energy regeneration significantly in comparison to the baseline parameters.

In addition, unfeasible solutions can be an indication of unsuitable reference trajectories or actuator parameters. An alternative approach when confronted with unsatisfactory solutions is to modify these trajectories and parameters. Closed-form expressions for the optimal parameter vector, provide information on how to move the parameter vector from an unfeasible region to a feasible region.

Closed-form expressions are also given for the optimal actuator parameters. We showed that when a solution for the optimal gear ratio exists, it is an unique and global maximum, and when the optimal gear ratio does not exist, stored energy increases monotonically with the gear ratio. Energy regeneration was also shown to be strictly increasing with respect to DC motor parameter  $\gamma$ . This is an important design factor for selecting DC machines for regenerative applications.

Moreover, with some trajectories and parameters, charge buildup may occur in the capacitors. A net charging trend could be desirable for extended operating times in systems with on-board storage; however, ultracapacitors become damaged if overcharged. To prevent over-charging, regenerated energy can be stored using an additional backup capacitor, or dissipated in a control resistor by using a simple thermostat-like switching logic.

The solutions presented here are straightforward to use and eliminate or reduce the need for heuristic numerical computations. They also provide valuable insight into the limits and practicality of regenerative energy systems.

## CHAPTER IV

### TRAJECTORY OPTIMIZATION PROBLEMS

#### 4.1 Introduction

We investigate trajectory optimization problems for robots with energy regenerative drive system. Given system parameters, and using the framework presented in Chapter II, force and motion trajectories are found that maximize energy regeneration of one or several semi-active joints. We strive to find closed-form solutions for these optimization problems; however, when analytical solutions are not attainable, we resort to numerical methods to find the optimal solutions. We also investigate the general linear and nonlinear optimal control problems, and provide simulations to demonstrate the results.

#### 4.2 Some Results from the Calculus of Variations and Optimal Control Theory

In this section, we provide a brief overview of some of the results pertaining to the calculus of variations theory, and the variational approach to optimal control. Readers are referred to [57] for a comprehensive discussion of both theories.

A functional,  $J$ , is defined as a rule of correspondence that assigns to functions  $x$  belonging to a certain class  $\Omega$ , a unique real number [57]. Calculus of variations deals with finding necessary and sufficient conditions for optimality of functionals. The

simplest form of a variational problem can be defined as finding the scalar function  $x^*$  for which the functional

$$J(x) = \int_{t_1}^{t_2} g(x, \dot{x}, t) dt \quad (4.1)$$

has a relative extremum, assuming  $t_1$  and  $t_2$  are fixed,  $x(t_1)$  and  $x(t_2)$  are defined, and the integrand  $g$  has continuous first and second partial derivatives with respect to all of its arguments. The necessary condition for optimality can then be derived as [57]

$$\frac{\partial g}{\partial x}(x^*, \dot{x}^*, t) - \frac{d}{dt} \left[ \frac{\partial g}{\partial \dot{x}}(x^*, \dot{x}^*, t) \right] = 0 \quad (4.2)$$

If  $x(t_1)$  and/or  $x(t_2)$  are unspecified, in addition to the necessary condition of Eq. (4.2), extra boundary conditions must also be satisfied for optimality

$$\frac{\partial g}{\partial \dot{x}}(x^*(t_1), \dot{x}^*(t_1), t_1) = 0 \quad (4.3)$$

and/or

$$\frac{\partial g}{\partial \dot{x}}(x^*(t_2), \dot{x}^*(t_2), t_2) = 0$$

For the general case,

$$J(x_1, \dots, x_n) = \int_{t_1}^{t_2} g(x_1, \dots, x_n, \dot{x}_1, \dots, \dot{x}_n, t) dt \quad (4.4)$$

the necessary condition for optimality becomes

$$\frac{\partial g}{\partial \mathbf{x}}(\mathbf{x}^*, \dot{\mathbf{x}}^*, t) - \frac{d}{dt} \left[ \frac{\partial g}{\partial \dot{\mathbf{x}}}(\mathbf{x}^*, \dot{\mathbf{x}}^*, t) \right] = 0 \quad (4.5)$$

where

$$\mathbf{x} = \left[ x_1, \dots, x_n \right] \quad (4.6)$$

If  $\mathbf{x}$  is specified at the initial and/or final times, the boundary condition for the problem is formulated as

$$\mathbf{x} = \mathbf{x}_0 @ t = t_1, \quad \mathbf{x}(i) = \mathbf{x}_f @ t = t_2 \quad (4.7)$$

and if the initial and/or final  $\mathbf{x}$  is unspecified, the boundary conditions are derived from

$$\begin{aligned} \frac{\partial g}{\partial \dot{\mathbf{x}}}(\mathbf{x}^*(t_1), \dot{\mathbf{x}}^*(t_1), t_1) &= 0 \\ \frac{\partial g}{\partial \dot{\mathbf{x}}}(\mathbf{x}^*(t_2), \dot{\mathbf{x}}^*(t_2), t_2) &= 0 \end{aligned} \quad (4.8)$$

Mixed boundary conditions are also possible, where some of the elements of  $\mathbf{x}$  are specified and others are not.

Using calculus of variations, necessary optimality conditions can be derived for the optimal control problem. The general optimal control problem is formulated as finding the  $m \times 1$  control vector,  $\mathbf{u}^*(t)$ , and the  $n \times 1$  state vector,  $\mathbf{x}^*(t)$ , that minimizes

$$J = h(\mathbf{x}(t_2), t_2) + \int_{t_1}^{t_2} g(\mathbf{x}(t), \mathbf{u}(t), t) dt \quad (4.9)$$

while being subjected to

$$\dot{x} = f(\mathbf{x}(t), \mathbf{u}(t), t) \quad (4.10)$$

The cases considered here assume specified initial and final times, and specified initial conditions (i.e.,  $\mathbf{x}(t_1) = \mathbf{x}_0$ ). The Hamiltonian, denoted by  $\mathcal{H}$ , is defined by

$$\mathcal{H} = g(\mathbf{x}(t), \mathbf{u}(t), t) + \mathbf{p}^T f(\mathbf{x}(t), \mathbf{u}(t), t) \quad (4.11)$$

where the vector  $\mathbf{p}$  is known as the costate. Necessary conditions for optimality are



expressed as [57]

$$\begin{aligned}
\dot{\mathbf{x}}^*(t) &= \frac{\partial \mathcal{H}}{\partial \mathbf{p}}(\mathbf{x}^*(t), \mathbf{u}^*(t), \mathbf{p}^*(t), t) \\
\dot{\mathbf{p}}^*(t) &= -\frac{\partial \mathcal{H}}{\partial \mathbf{x}}(\mathbf{x}^*(t), \mathbf{u}^*(t), \mathbf{p}^*(t), t) \\
0 &= \frac{\partial \mathcal{H}}{\partial \mathbf{u}}(\mathbf{x}^*(t), \mathbf{u}^*(t), \mathbf{p}^*(t), t)
\end{aligned} \tag{4.12}$$

For fixed final states, the boundary condition is

$$\mathbf{x}^*(t_2) = \mathbf{x}_f \tag{4.13}$$

and for free final states the boundary condition becomes

$$\frac{\partial h}{\partial \mathbf{x}}(\mathbf{x}^*(t_2), t_2) - \mathbf{p}^*(t_2) = \mathbf{0} \tag{4.14}$$

A combination of fixed and free final states is also possible.

### 4.3 External Force/Moment Trajectory Optimization

In this section, we aim to find the optimal external force/moment trajectory that, when applied to the system, maximizes energy regeneration in the semi-active joints. We assume that the system parameters are given and the robot asymptotically tracks desired reference trajectories,  $q^d$ . For the  $j$ -th semi-active joint, the problem is formulated as

$$\max_{\mathcal{T}_j} \Delta E_{sj} = \int_{t_1}^{t_2} \left( \tau_j^d \dot{q}_j^d - \frac{R_j \tau_j^{d2}}{a_j^2} \right) dt = \int_{t_1}^{t_2} F_j(\mathcal{T}_j, t) dt \tag{4.15}$$

where  $\tau_j^d$  is derived from

$$\tau_j^d = Y_j(q^d, \dot{q}^d, \ddot{q}^d)\Theta + m_j n_j^2 \dot{q}_j^d + (b_j n_j^2 + \frac{a_j^2}{R_j}) \dot{q}_j^d + \mathcal{T}_j \tag{4.16}$$

For maximizing energy regeneration in several semi-active joints, the problem reduces to the formulation presented in Eq. (4.15), hence the solution presented here is valid for both cases. Using Eq. (4.2), the necessary condition for optimality becomes

$$\frac{\partial F_j}{\partial \mathcal{T}_j} = 0 \quad (4.17)$$

Replacing for  $F_j$ , we have

$$\frac{\partial \tau_j^d}{\partial \mathcal{T}_j} \left( \dot{q}_j - 2 \frac{R_j}{a_j^2} \tau_j^d \right) = 0 \quad (4.18)$$

If  $\partial \tau_j^d / \partial \mathcal{T}_j = 0$ , the objective function is independent of  $\mathcal{T}_j$  and the problem is ill defined, hence

$$\tau_j^d = \frac{a_j^2}{2R_j} \dot{q}_j \quad (4.19)$$

and the optimum external force/moment trajectory,  $\mathcal{T}_j^*$ , is derived by replacing for  $\tau_j^d$  from Eq. (4.16):

$$\mathcal{T}_j^* = \frac{a_j^2}{2R_j} \dot{q}_j - Y_j(q^d, \dot{q}^d, \ddot{q}^d) \Theta - m_j n_j^2 \dot{q}_j^d - (b_j n_j^2 + \frac{a_j^2}{R_j}) \dot{q}_j^d \quad (4.20)$$

Substituting Eq. (4.19) into Eq. (4.15), the expression for the maximum attainable energy regeneration is derived as

$$\Delta E_{sj}^* = \int_{t_1}^{t_2} \frac{a_j^2}{4R_j} (\dot{q}_j^d)^2 dt \quad (4.21)$$

To show that this equation is indeed a maximum, we look at the second variation of the functional in Eq. (4.15).

$$\delta^2 \Delta E_{sj}(\mathcal{T}_j, t) = \int_{t_1}^{t_2} \frac{\partial^2 F_j}{\partial \mathcal{T}_j^2} \delta \mathcal{T}_j^2 dt = \int_{t_1}^{t_2} \frac{\partial^2 \tau_j^d}{\partial \mathcal{T}_j^2} \left( \dot{q}_j^d - \frac{a_j^2}{2R_j} \tau_j^d \right) - \frac{a_j^2}{2R_j} \left( \frac{\partial \tau_j^d}{\partial \mathcal{T}_j^d} \right)^2 dt \quad (4.22)$$

Replacing for  $\mathcal{T}_j$  from Eq. (4.20), the second variation reduces to

$$\delta^2 \Delta E_{sj}(\mathcal{T}_j^*, t) = -\frac{a_j^2}{2R_j}(t_2 - t_1) < 0 \quad (4.23)$$

which is always negative, and hence  $\mathcal{T}_j^*$  is a maximum. Furthermore, to demonstrate that this maximum is global, we initially assume that it is not, and there exists an alternative desired control for which the system regenerates more energy:

$$\tau_j^d = \frac{a_j^2}{2R_j} \dot{q}_j + v(t) \quad (4.24)$$

where  $v(t)$  can be any function. Replacing into Eq. (4.15) results in

$$\Delta E_{sj} = \int_{t_1}^{t_2} \frac{a_j^2}{4R_j} (\dot{q}_j^d)^2 dt - \int_{t_1}^{t_2} \frac{R_j}{a_j^2} v(t)^2 dt \leq \Delta E_{sj}^* \quad (4.25)$$

Therefore the initial premise is not valid, and  $\mathcal{T}_j^*$  is a global maximum. Moreover  $\mathcal{T}_j^*$  is the unique solution of Eq. (4.20), and hence it is a unique global maximum.

Equation (4.21) has some interesting features. It only depends on the reference trajectory followed by the joint ( $\dot{q}_j^d$ ), and the actuator parameters ( $n_j$ , and  $\gamma_j = \alpha_j^2/R_j$ ). It is an increasing function with respect to  $n_j$  and  $\gamma_j$ , and a larger value for these parameters will contribute to more energy regeneration. Moreover, Eq. (4.21) does not depend on the manipulator parameters ( $\theta$ ) and manipulator dynamics ( $Y_j$ ). This is due to the assumption that the joint will robustly follow the desired trajectory ( $q_j^d$ ). We can conclude that Eq. (4.21) expresses the maximum attainable energy regeneration in  $j$ -th semi-active joint with respect to  $\mathcal{T}_j^*$ , provided that the joint asymptotically tracks the desired trajectory.

To demonstrate the results of this section, we consider again the double pen-

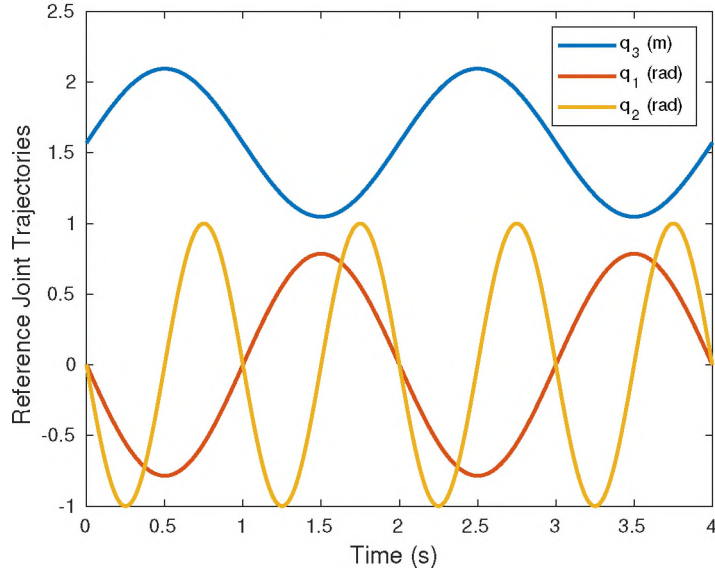


Figure 18: Reference trajectories for the cart double pendulum system.

dulum and cart system, where the manipulator parameter vector is given by

$$\theta = \begin{bmatrix} -0.72 & 0.24 & 0.512 & 0.192 & 0.128 & 0.01 & 0.01 & 0.01 & 2.2 \end{bmatrix} \quad (4.26)$$

and the semi-active actuators are identical except for the gear ratios, with  $R = 0.3 \Omega$ ,  $\alpha = 0.0302 \text{ Nm/A}$ ,  $m = 1 \times 10^{-5} \text{ kg.m}^2$ ,  $n_1 = 100$ ,  $n_2 = 30$ , and negligible joint friction.

Figure 18 shows the reference joint trajectories, where an inverse dynamics controller is used to guarantee trajectory tracking. Initially, no external forces or moments are exerted on the system, and Fig. 19 shows the simulation results for this case. Both semi-active joints are consuming energy, such that at the end of the simulation, Joint 1 and Joint 2 regenerate  $-87.1 \text{ J}$  and  $-63.56 \text{ J}$  respectively. Power flows show that most of the input energy to the semi-active joints is dissipated as Joule losses.

The optimal moment trajectory,  $\mathcal{T}_2^*$ , that maximizes energy regeneration for Joint 2 is computed using Eq. (4.20), and shown in Fig. 20. The simulation results

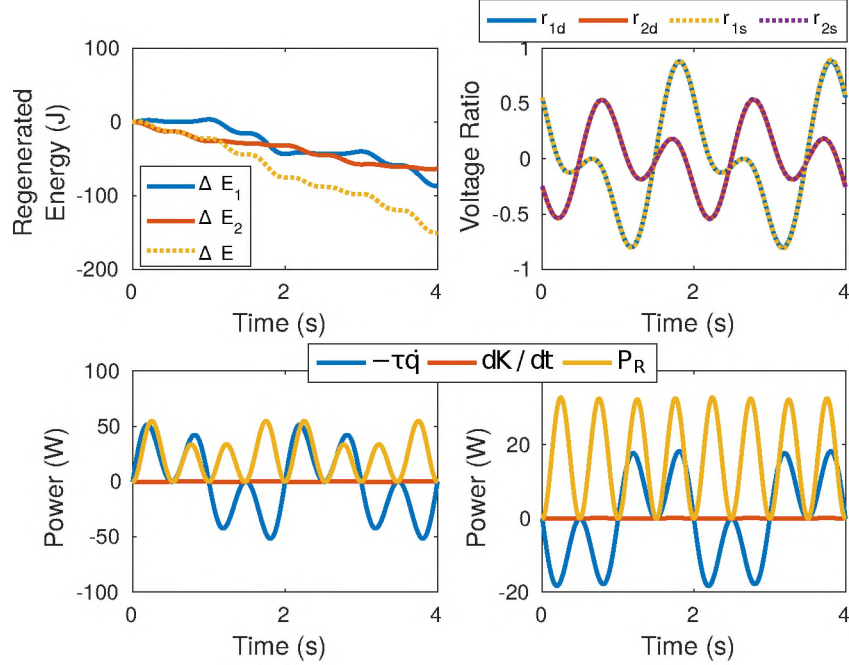


Figure 19: Simulation results for initial case with no external moments applied: top left) regenerated energy, top right) voltage ratio, lower left) power flows for Joint 1, lower right) power flows for Joint 2. Distributed configuration: solid lines, star configuration: dotted lines.

with  $\mathcal{T}_2^*$  applied to the system are shown in Fig. 21. Note that the inverse dynamics controller tracks the reference trajectories even with  $\mathcal{T}_2^*$  applied. We can see that Joint 2 is regenerating energy such that 8.32 J of energy is regenerated at the end of the simulation. This value agrees with that obtained from Eq. (4.21). A comparison of the power flows of Fig. 19 and Fig. 21 show that the Joule losses in Joint 2 have decreased while power flows and energy regeneration for Joint 1 remain the same. This is due to the fact that  $\mathcal{T}_2^*$  does not affect the dynamics of Joint 1. The Sankey diagram in Fig. 22 shows that the vast majority of input energy (91%) is being dissipated as resistive losses.

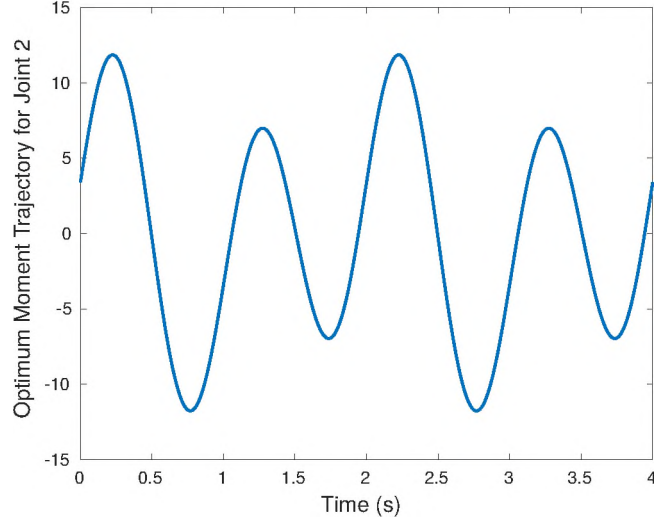


Figure 20: Optimum moment trajectory (N.m),  $\mathcal{T}_2^*$ , calculated from Eq. (4.20), that maximizes energy regeneration in Joint 2 of the cart double pendulum system.

#### 4.4 A More General Trajectory Optimization

We consider maximizing energy regeneration with respect to the variable  $x(t)$ , that satisfies the following conditions:

$$(i) \quad x \neq \dot{q}_j^d \quad (4.27)$$

$$(ii) \quad \frac{\partial \tau_j^d}{\partial x} \neq 0 \quad (4.28)$$

$$(iii) \quad \frac{\partial^h \tau_j^d}{\partial x^h} = 0 \quad \text{for } h > 1 \quad (4.29)$$

The variable  $x$  can be any motion, force, or moment trajectory that satisfies the above conditions. When maximizing energy regeneration in a single semi-active joint, and assuming all other system variables and parameters are fixed, the problem can be formulated as

$$\max_x \Delta E_{sj} = \int_{t_1}^{t_2} \left( \tau_j^d \dot{q}_j - \frac{R_j \tau_j^{d2}}{a_j^2} \right) dt = \int_{t_1}^{t_2} F_j(x, t) dt \quad (4.30)$$

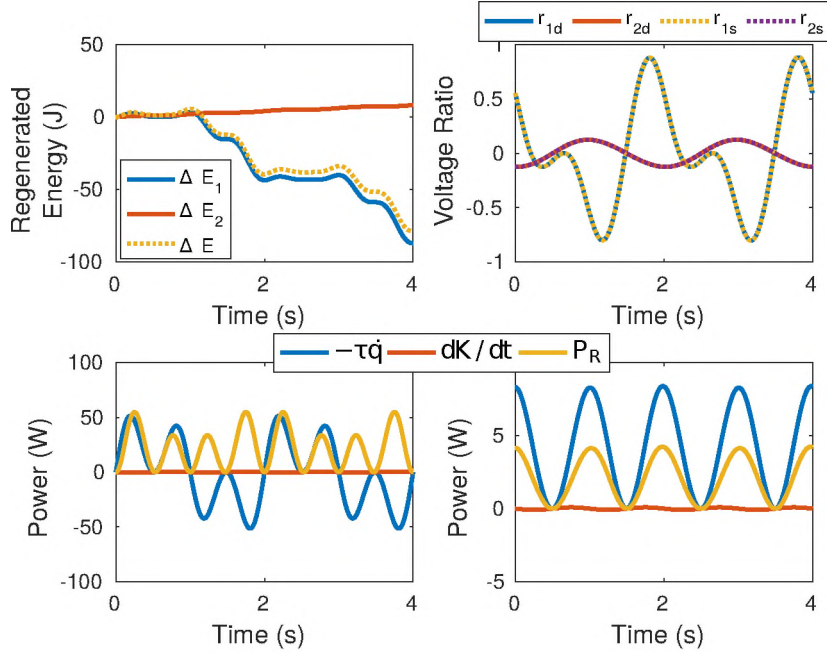


Figure 21: Simulation results with the optimal moment trajectory,  $\mathcal{T}_2^*$ , applied: top left) regenerated energy, top right) voltage ratio, lower left) power flows for Joint 1, lower right) power flows for Joint 2. Distributed configuration: solid lines, star configuration: dotted lines.

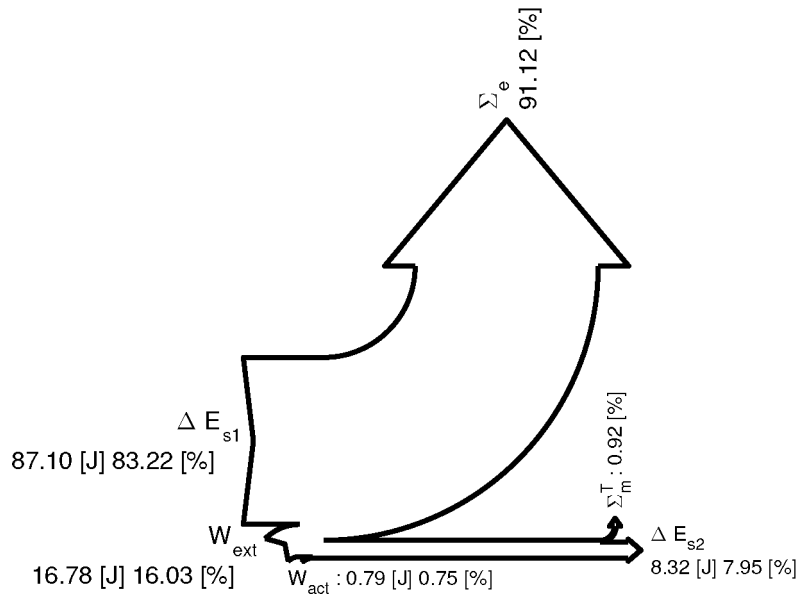


Figure 22: Sankey diagram for the external energy balance with the optimal moment trajectory,  $\mathcal{T}_2^*$ , applied. The overall mechanical energy is represented by  $\Delta E_m$ ,  $\Sigma_e$  and  $\Sigma_m$  are the electrical and mechanical losses respectively,  $W_{act}$  is the work done by the fully-active joints, and  $\Delta E_{sj}$  is the energy going to (i.e., regenerated) or coming from (i.e., consumed) the  $j$ -th semi-active actuator.

where  $\tau_j^d$  is obtained from Eq. (4.16). Using Eq. (4.2), the necessary condition for optimality is derived as

$$\frac{\partial F_j}{\partial x} = \frac{\partial \tau_j^d}{\partial x} \left( \dot{q}_j^d - \frac{2R_j}{a_j^2} \tau_j^d \right) = 0 \quad (4.31)$$

Since  $\partial \tau_j^d / \partial x \neq 0$  (Condition (ii), Eq. (4.28)), the necessary condition for optimality becomes

$$\tau_j^d = \frac{a_j^2}{2R_j} \dot{q}_j^d \quad (4.32)$$

which is the same as what was obtained for the force/moment trajectory optimization problem in the previous section. This is not surprising since  $\mathcal{T}_j$  satisfies all the conditions for  $x$  (Eq. (4.27) to Eq. (4.29)).

$\tau_j^d$  can be rearranged as (Condition (iii), Eq. (4.29))

$$\tau_j^d = A_j x + B_j \quad (4.33)$$

and the optimal value for  $x$  can be derived as

$$x^* = \frac{1}{A_j} \left( \frac{a_j^2}{2R_j} \dot{q}_j^d - B_j \right) \quad (4.34)$$

Similar to Section 4.3, we can show that  $x^*$  is a unique and global maximum. Replacing Eq. (4.32) in Eq. (4.30), the expression for the maximum attainable energy is derived and is equal to Eq. (4.21).

These results can be extended for the case of maximizing energy regeneration in several semi-active joints:

$$\max_x \Delta E_s = \int_{t_1}^{t_2} \sum_{j=1}^e \left( \tau_j^d \dot{q}_j - \frac{R_j \tau_j^d{}^2}{a_j^2} \right) dt = \int_{t_1}^{t_2} \sum_{j=1}^e F_j(x, t) dt \quad (4.35)$$



where the variable  $x$  satisfies

$$(i) \quad x \neq \dot{q}_j^d \quad j = 1, \dots, e \quad (4.36)$$

$$(ii) \quad \frac{\partial \tau_j^d}{\partial x} \neq 0 \quad j = 1, \dots, e \quad (4.37)$$

$$(iii) \quad \frac{\partial^h \tau_j^d}{\partial x^h} = 0 \quad h > 1 \text{ and } j = 1, \dots, e \quad (4.38)$$

The necessary condition for optimality is then derived from Eq. (4.5) as

$$\sum_{j=1}^e \frac{\partial F_j}{\partial x} = \sum_{j=1}^e \frac{\partial \tau_j^d}{\partial x} \left( \dot{q}_j^d - \frac{2R_j}{a_j^2} \tau_j^d \right) = 0 \quad (4.39)$$

Rewriting  $\tau_j^d$  as in Eq. (4.33) (Condition (iii), Eq. 4.38), the optimum  $x$  can be found as

$$x^* = \frac{\sum_{j=1}^e A_j \left( \dot{q}_j^d - \frac{2R_j}{a_j^2} B_j \right)}{\sum_{j=1}^e \frac{2R_j}{a_j^2} A_j^2} \quad (4.40)$$

A careful inspection of the above equation reveals a relation between the optimum  $x$  when optimizing for a single semi-active joint ( $x_j^*$  derived from Eq. (4.34)), and the optimum  $x$  when optimizing for all semi-active joints ( $x^*$  derived from Eq. (4.40)). This relation can be expressed as the weighted average of  $x_j^*$ :

$$x^* = \frac{\sum_{j=1}^e w_j x_j^*}{\sum_{j=1}^e w_j} \quad (4.41)$$

where  $w_j = \frac{2R_j}{a_j^2} A_j^2$ .

To demonstrate the results, we revisit the cart double inverted pendulum system, where the manipulator and actuator parameters are the same as the example in Section 4.3, an inverse dynamics controller is used to track reference trajectories for Joint 1 and Joint 2 shown in Fig. 18, and no external forces or moments are applied to the system. We aim to find the optimal reference trajectory for Joint 3 ( $q_3^d$ ) that maximizes energy energy regeneration in Joint 1 and Joint 2. Note that

Joint 3 is fully-active. We can verify that  $\ddot{q}_3^d$  satisfies all the conditions of Eq. (4.36) to Eq. (4.38).  $\tau_1^d$  and  $\tau_2^d$  can be rearranging according to Eq. (4.33), to find

$$\begin{aligned}
 A_1 &= \sin(q_1)\theta_1 - \sin(q_1 + q_2)\theta_2 & (4.42) \\
 B_1 &= -g \cos(q_1)\theta_1 + g \cos(q_1 + q_2)\theta_2 + Y(1, 3 : 9)\theta(3 : 9) + m_1 n_1^2 \ddot{q}_1 + \frac{a_1^2}{R_1} \dot{q}_1 \\
 A_2 &= -\sin(q_1 + q_2)\theta_2 \\
 B_2 &= g \cos(q_1 + q_2)\theta_2
 \end{aligned}$$

Using Eq. (4.40) the optimal  $\ddot{q}_3^d$  is derived, and integrating yields  $\dot{q}_3^d$  and  $q_3^d$ . The initial conditions for integration are chosen such that  $mean(q_3^d) = 0$  and  $mean(\dot{q}_3^d) = 0$ . These trajectories are shown in Fig. 23. Figure 24 and Fig. 25 show the simulation results. We can see that compared to the results of the non-optimized case in Fig. 19, energy regeneration has increased such that at the end of the simulation, Joint 1 and Joint 2 regenerate  $-45.21$  J and  $38.58$  J of energy respectively, which adds up to a total of  $-6.63$  J for both semi-active joints. The Sankey diagram in Fig. 25 shows that the optimized  $q_3$  injects energy into the system ( $W_{act}$ ) to maximize energy regeneration.

#### 4.5 Linear Optimal Control Problem

In this section, we present the closed-form solution to the optimal control problem for regenerative energy systems described by a linear system model. This solution can be applied to energy regenerative robotic systems that can be accurately modeled as a linear time invariant systems.

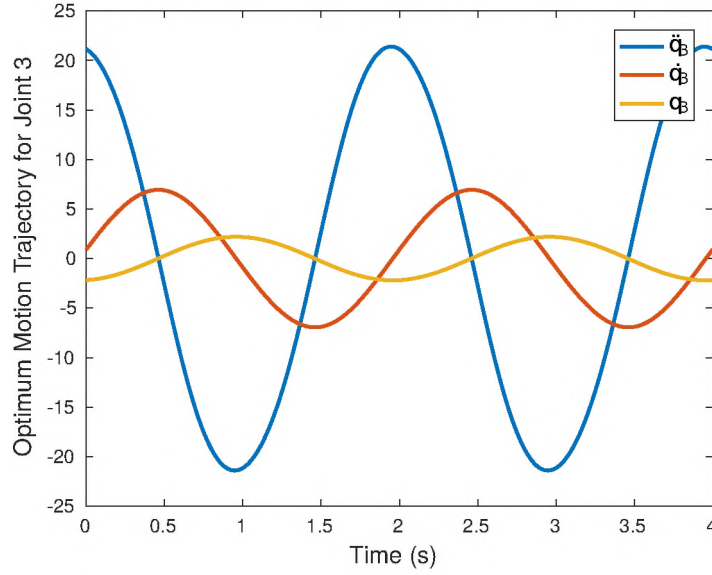


Figure 23: Optimum motion trajectory for Joint 3,  $q_3^d$  (m), that maximizes energy regeneration in Joint 1 and Joint 2.

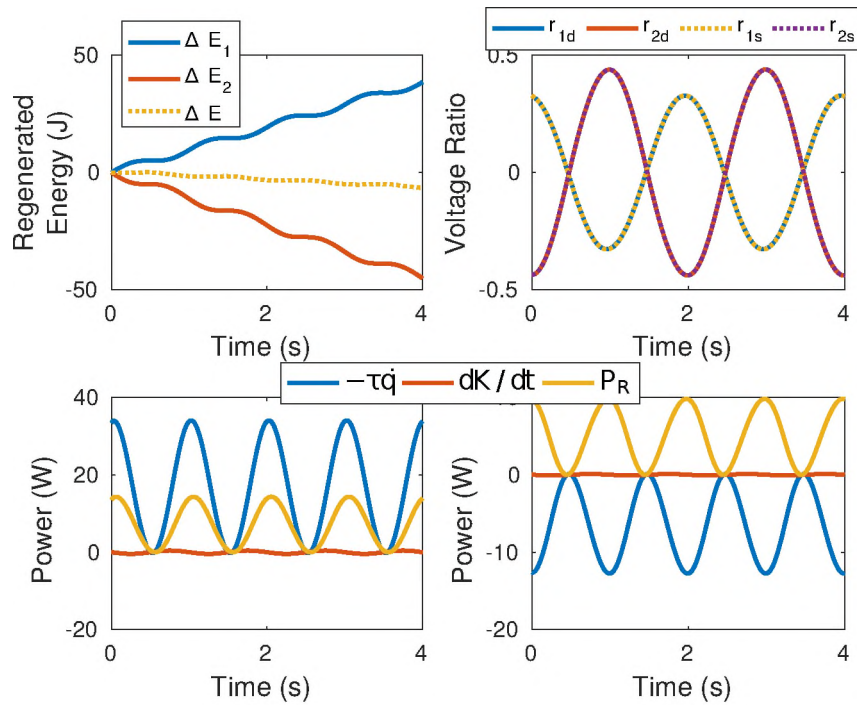


Figure 24: Simulation results with optimized trajectory for Joint 3: top left) regenerated energy, top right) voltage ratio, lower left) power flows for Joint 1, lower right) power flows for Joint 2. Distributed configuration: solid lines, star configuration: dotted lines.

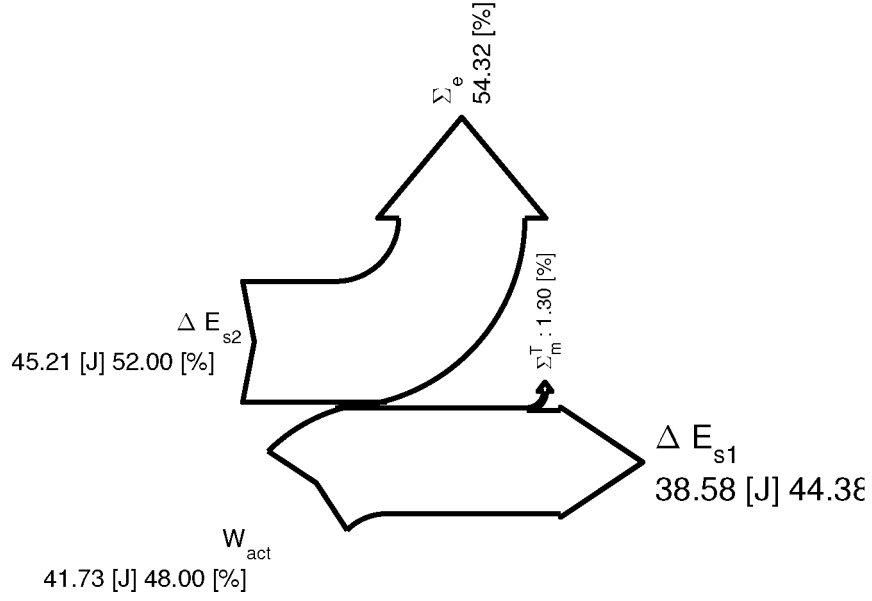


Figure 25: Sankey diagram when the trajectory of Joint 3 is optimized. The overall mechanical energy is represented by  $\Delta E_m$ ,  $\Sigma_e$  and  $\Sigma_m$  are the electrical and mechanical losses respectively,  $W_{act}$  is the work done by the fully-active joints, and  $\Delta E_{sj}$  is the energy going to (i.e., regenerated) or coming from (i.e., consumed) the  $j$ -th semi-active actuator.

Taking the state and control vectors to be

$$\boldsymbol{\tau}^d = \left[ \tau_1^d, \dots, \tau_e^d \right]^T \quad (4.43)$$

$$\boldsymbol{x} = \left[ q_1, \dots, q_e, \dot{q}_1, \dots, \dot{q}_e \right]^T \quad (4.44)$$

the objective is to find the optimal virtual control,  $\boldsymbol{\tau}^{d*}(t)$ , and state trajectory,  $\boldsymbol{x}^*(t)$ , that maximize energy regeneration in semi-active joints 1 to  $e$

$$\max_{\boldsymbol{\tau}^d, \boldsymbol{x}} J = -\frac{1}{2} [\boldsymbol{x}(t_f) - \boldsymbol{x}_f]^T H [\boldsymbol{x}(t_f) - \boldsymbol{x}_f] + \int_0^{t_f} \sum_{j=1}^e \tau_j^d \dot{q}_j - \frac{R_j}{a_j^2} (\tau_j^d)^2 dt \quad (4.45)$$

while being constrained to the dynamic equation of the system

$$\dot{\boldsymbol{x}} = A\boldsymbol{x} + B\boldsymbol{\tau}_j^d + B\boldsymbol{\tau}_{ext} \quad (4.46)$$

where  $\boldsymbol{\tau}_{ext}$  is the external force or moment applied to the joints. All the system parameters are assumed to be constant, and all other joints not considered in the optimization are assumed to follow reference trajectories,  $q^d$ . We take the initial states ( $\boldsymbol{x}(0)$ ) and the final time ( $t_f$ ) to be fixed, and take the final final states ( $\boldsymbol{x}(t_f)$ ) to be free. We also use the penalty function approach to drive the system to the final states ( $\boldsymbol{x}_f$ ), where  $H$  is a diagonal matrix with positive elements. This problem is equivalent to

$$\min_{\boldsymbol{\tau}^d, \boldsymbol{x}} J = \frac{1}{2}[\boldsymbol{x}(t_f) - \boldsymbol{x}_f]^T H[\boldsymbol{x}(t_f) - \boldsymbol{x}_f] + \frac{1}{2} \int_0^{t_f} \begin{bmatrix} \boldsymbol{x}^T & (\boldsymbol{\tau}^d)^T \end{bmatrix} \begin{bmatrix} Q & M \\ M^T & W \end{bmatrix} \begin{bmatrix} \boldsymbol{x} \\ \boldsymbol{\tau}^d \end{bmatrix} dt \quad (4.47)$$

where

$$Q = \mathbf{0}_{2e \times 2e} \quad M = \begin{bmatrix} \mathbf{0}_{e \times e} \\ -\mathbf{I}_{e \times e} \end{bmatrix} \quad W = \text{diag} \left[ \frac{2R_1}{a_1^2}, \dots, \frac{2R_e}{a_e^2} \right] \quad (4.48)$$

with  $\mathbf{0}$  being the zero matrix, and  $\mathbf{I}$  the identity matrix. The solution presented here closely follows the solution of the linear tracking optimal control problem, which can be found in [57]. The Hamiltonian can be derived from Eq. (4.11) as

$$\mathcal{H} = \frac{1}{2} \begin{bmatrix} \boldsymbol{x} & \boldsymbol{\tau}^d \end{bmatrix}^T \begin{bmatrix} Q & M \\ M^T & W \end{bmatrix} \begin{bmatrix} \boldsymbol{x} \\ \boldsymbol{\tau}^d \end{bmatrix} + \boldsymbol{p}^T (A\boldsymbol{x} + B\boldsymbol{\tau}^d + B\boldsymbol{\tau}_{ext}) \quad (4.49)$$

and the necessary conditions for optimality from Eq. (4.12) as

$$\dot{\boldsymbol{p}}^* = -\frac{\partial \mathcal{H}}{\partial \boldsymbol{x}} = -Q\boldsymbol{x}^* - M(\boldsymbol{\tau}^d)^* - A^T \boldsymbol{p}^* \quad (4.50)$$

$$0 = \frac{\partial \mathcal{H}}{\partial \boldsymbol{\tau}^d} = M^T \boldsymbol{x}^* + W(\boldsymbol{\tau}^d)^* + B^T \boldsymbol{p}^* \quad (4.51)$$

$$\dot{\boldsymbol{x}}^* = A\boldsymbol{x}^* + B(\boldsymbol{\tau}^d)^* + B\boldsymbol{\tau}_{ext} \quad (4.52)$$

Solving Eq. (4.51), the optimal virtual control can be found as

$$(\boldsymbol{\tau}^d)^* = -W^{-1} (M^T \mathbf{x}^* + B^T \mathbf{p}^*) \quad (4.53)$$

Replacing in Eq. (4.52) and Eq. (4.50) and simplifying results in

$$\dot{\mathbf{x}}^* = (A - BW^{-1}M^T) \mathbf{x}^* - BW^{-1}B^T \mathbf{p}^* + B\boldsymbol{\tau}_{ext} \quad (4.54)$$

$$\dot{\mathbf{p}}^* = (-Q + MW^{-1}M^T) \mathbf{x}^* + (MW^{-1}B^T - A^T) \mathbf{p}^* \quad (4.55)$$

which can also be represented in matrix form as

$$\begin{bmatrix} \dot{\mathbf{x}}^* \\ \dot{\mathbf{p}}^* \end{bmatrix} = \begin{bmatrix} A - BW^{-1}M^T & -BW^{-1}B^T \\ -Q + MW^{-1}M^T & MW^{-1}B^T - A^T \end{bmatrix} + \begin{bmatrix} B\boldsymbol{\tau}_{ext} \\ 0 \end{bmatrix} \quad (4.56)$$

The above system of differential equations are linear, time varying, and non-homogeneous.

The solution can be written as

$$\begin{bmatrix} \mathbf{x}^*(t_f) \\ \mathbf{p}^*(t_f) \end{bmatrix} = \phi(t_f, t) \begin{bmatrix} \mathbf{x}^*(t) \\ \mathbf{p}^*(t) \end{bmatrix} + \int_{t_1}^{t_2} \phi(t_f, \eta) \begin{bmatrix} B\boldsymbol{\tau}_{ext} \\ 0 \end{bmatrix} d\eta \quad (4.57)$$

where  $\phi$  is the transition matrix and can be partitioned as

$$\phi = \begin{bmatrix} \phi_{11} & \phi_{12} \\ \phi_{21} & \phi_{22} \end{bmatrix} \quad (4.58)$$

and the integral in Eq. (4.57) can be replaced by the  $2n \times 1$  vector  $[f_1^T, f_2^T]^T$ . Replacing in Eq. (4.57) we obtain

$$\mathbf{x}^*(t_f) = \phi_{11}(t_f, t) \mathbf{x}^*(t) + \phi_{12}(t_f, t) \mathbf{p}^*(t) + f_1(t) \quad (4.59)$$

$$\mathbf{p}^*(t_f) = \phi_{21}(t_f, t) \mathbf{x}^*(t) + \phi_{22}(t_f, t) \mathbf{p}^*(t) + f_2(t) \quad (4.60)$$

The boundary conditions can be derived from Eq. (4.14), and the final condition for the optimal costate is

$$\mathbf{p}^*(t_f) = H\mathbf{x}^*(t_f) - H\mathbf{x}_f \quad (4.61)$$

Replacing in Eq. (4.60), and substituting  $\mathbf{x}^*(t_f)$  from Eq. (4.59), we find  $p^*(t)$  as

$$\begin{aligned} \mathbf{p}^*(t) &= [H\phi_{12} - \phi_{22}]^{-1}[\phi_{21} - H\phi_{11}]\mathbf{x}^*(t) + [H\phi_{12} - \phi_{22}]^{-1}[f_2 - Hf_1 + H\mathbf{x}_f] \quad (4.62) \\ &= K(t)\mathbf{x}^*(t) + S(t) \end{aligned}$$

Replacing

$$\mathbf{p}^* = K\mathbf{x}^* + S \quad (4.63)$$

$$\dot{\mathbf{p}}^* = \dot{K}\mathbf{x}^* + K\dot{\mathbf{x}}^* + \dot{S}$$

into Eq. (4.54) and Eq. (4.55) and eliminating  $\dot{\mathbf{x}}^*$  we obtain

$$\begin{aligned} &\left[ \dot{K} + Q - MW^{-1}M^T - MW^{-1}B^TK + A^TK + KA - KBW^{-1}M^T \right. \\ &\left. - KBW^{-1}B^TK \right] \mathbf{x}^* + \left[ \dot{S} - KBW^{-1}B^TS - MW^{-1}B^TS + A^TS + KB\boldsymbol{\tau}_{ext} \right] = 0 \end{aligned} \quad (4.64)$$

Since this equation must be satisfied for all  $\mathbf{x}^*(t)$  and all  $\boldsymbol{\tau}_{ext}$ , we have

$$\begin{aligned} \dot{K} &= -Q + K(BW^{-1}M^T - A) + (MW^{-1}B - A^T)K + KBW^{-1}B^TK \\ &\quad + MW^{-1}M^T \end{aligned} \quad (4.65)$$

$$\dot{S} = (KBW^{-1}B^T + MW^{-1}B^T - A^T)S - KB\boldsymbol{\tau}_{ext} \quad (4.66)$$

From Eq. (4.61) and Eq. (4.63), the final conditions for  $K(t)$  and  $S(t)$  become

$$K(t_f) = H \quad (4.67)$$

$$S(t_f) = -H\mathbf{x}_f$$

Using the final conditions, Eq. (4.65) and Eq. (4.66) can be integrated backwards in time to derive  $K(t)$  and  $S(t)$ . Replacing  $K(t)$  and  $S(t)$  into Eq. (4.63), and then replacing the result into Eq. (4.53), we obtain the optimal virtual control

$$(\boldsymbol{\tau}^d)^* = -W^{-1} (M^T \mathbf{x}^* + B^T (K \mathbf{x}^* + S)) \quad (4.68)$$

The maximum attainable energy regeneration can then be derived as

$$\Delta E_s^* = \int_0^{t_f} \frac{1}{2} (\mathbf{x}^*)^T M W^{-1} M^T \mathbf{x}^* - \frac{1}{2} (K \mathbf{x}^* + S)^T B W^{-1} B^T (K \mathbf{x}^* + S) dt \quad (4.69)$$

To demonstrate the results, we consider an example of a vehicle seat suspension system, depicted in Fig. 26a. In this example the base of the seat is moving with the trajectory  $w$ , and is connected to the seat via a regenerative semi-active actuator, and a spring with stiffness  $K_s$ . We aim to find the optimal control,  $(\boldsymbol{\tau}^d)^*$ , and the resulting seat trajectory,  $x^*$ , maximizing energy storage.

The system parameters are

$$M_m = 100 \text{ kg} \quad b = 1e - 2 \text{ N.m.s} \quad (4.70)$$

$$m = 1 \times 10^{-5} \text{ kg.m}^2 \quad n = 100 \text{ rad/m}$$

$$R = 0.1 \ \Omega \quad K_s = 9810 \text{ N/m}$$

$$\alpha = 0.0502 \text{ Nm/A}$$



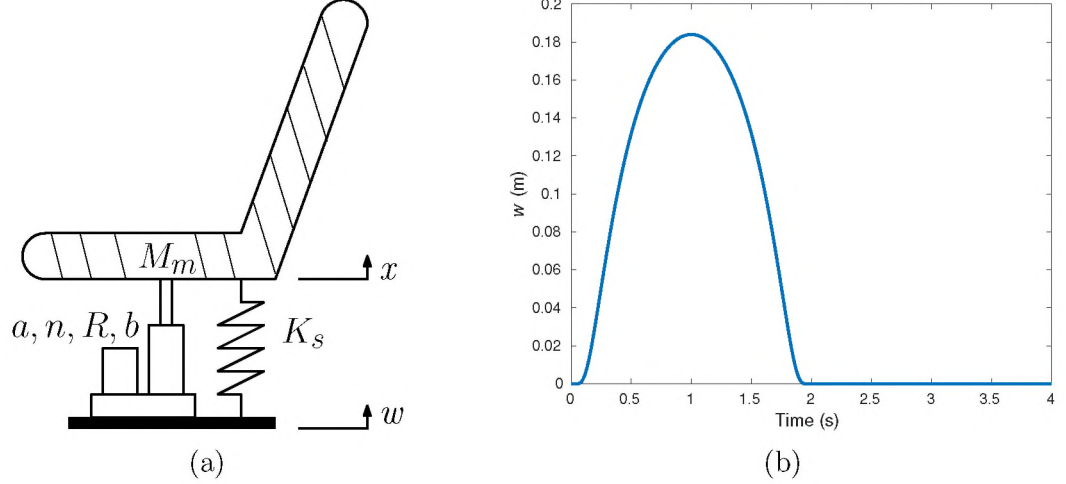


Figure 26: a) Example of a vehicle suspension system, used to demonstrate the linear optimal control problem for maximizing energy regeneration. b) The profile for  $w$  is selected to model a bump in the road.

and  $w$  follows the function

$$w(t) = \begin{cases} 0.5 \exp\left(-\frac{1}{1 - (t - 1)^2}\right) & 0 \leq t \leq 2 \\ 0 & \text{Otherwise} \end{cases} \quad (4.71)$$

which is used to simulate a bump in the road, and is shown in Fig. 26b. The linear state space model of the system can be derived as

$$A = \begin{bmatrix} 0 & 1 \\ -\frac{K_s}{M_m + mn^2} & -\frac{bn^2 + \frac{a^2}{R}}{M_m + mn^2} \end{bmatrix} \quad B = \begin{bmatrix} 0 \\ \frac{1}{M_m + mn^2} \end{bmatrix} \quad \tau_{ext} = -M_m \ddot{w} \quad (4.72)$$

We set the final desired state of the system to  $x_f = [0, 0]$ , and select

$$H = \begin{bmatrix} 10^6 & 0 \\ 0 & 10^5 \end{bmatrix} \quad (4.73)$$

To find the optimal solution, we integrate Eq. (4.65) and Eq. (4.66) backwards in time to obtain  $K(t)$  and  $S(t)$ , shown in Fig. 27a and Fig. 27b. The optimal control

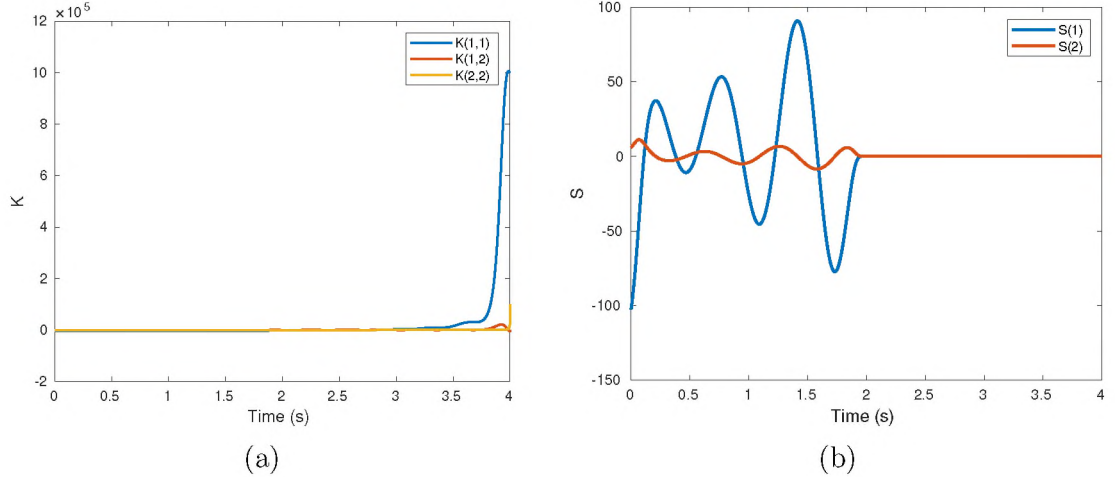


Figure 27: a)  $K(t)$  derived from integrating backwards Eq. (4.65), b)  $S(t)$  derived from integrating backwards Eq. (4.66).

is derived from Eq. (4.68), and Fig. 28 shows the system response when applying the optimal control. We can see that the movement of the base causes the seat to start vibrating. The semi-active joint initially takes advantage of this vibration and starts regenerating energy. However, close to the end of the simulation, the semi active joint consumes energy to bring the system states to zero and satisfy the final conditions. A total of 5.41 J energy is regenerated, which agrees with what was obtained from Eq. (4.69).

## 4.6 General Optimal Control Problem

The results of the previous section are limited to robotic systems that can be accurately modeled by linear equations; this, however, is not the case for most robotic systems. In this section, we investigate the general nonlinear optimal control problem, where we aim to find motion and control trajectories that maximize the amount of energy regenerated for a robotic system that is modeled by nonlinear equations.

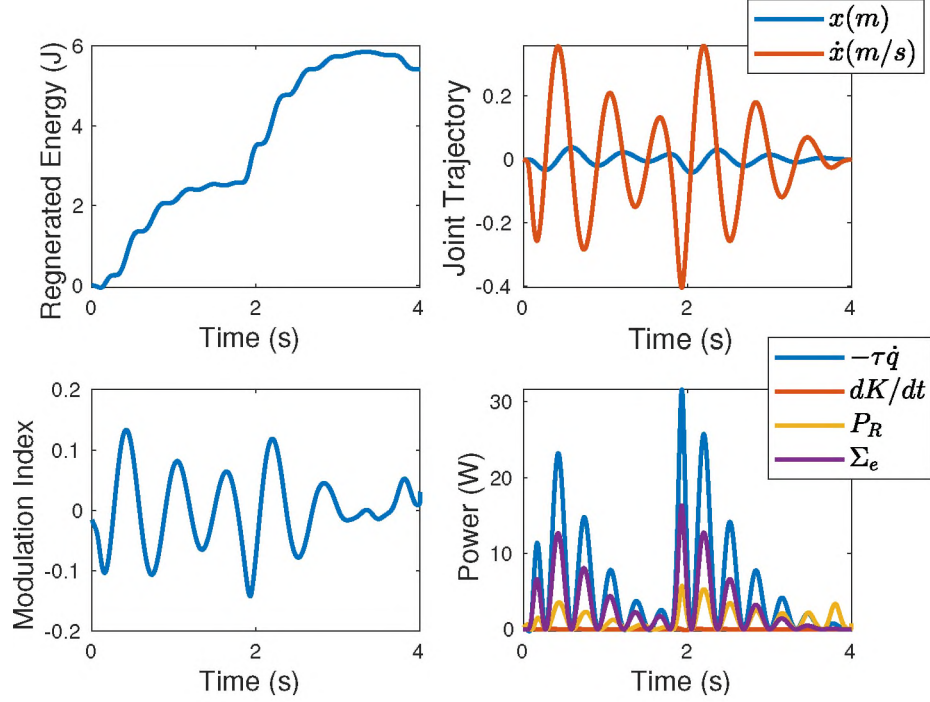


Figure 28: Simulation results for seat suspension system with optimal control : top left) regenerated energy, top right) system states, lower left) voltage ratio, lower right) semi-active joint power flows.

#### 4.6.1 Problem Formulation

The problem is formulated as an optimal control problem of finding the vector of optimal trajectories ( $\mathbf{q}(t)$ ) and the vector of optimal controls ( $\boldsymbol{\tau}^d$ ) that maximize energy regeneration in semi-active joints 1 to  $e$ :

$$\max_{\boldsymbol{\tau}^d, \mathbf{q}} J = \int_0^{t_f} \sum_{j=1}^e \left( \tau_j^d \dot{q}_j - \frac{R_j \tau_j^{d2}}{a_j^2} \right) dt \quad (4.74)$$

The robot starts from an initial configuration at time zero, and moves to a final configuration at some specified time, while being subjected to the dynamic equations of Eq. (2.3), bounds on the control, and constraints for the starting and ending points

of the trajectories.

$$D(q)\ddot{q} + C(q, \dot{q})\dot{q} + \mathcal{R}(q, \dot{q}) + g(q) + \mathcal{T} = \tau^d \quad (4.75a)$$

$$\frac{-a_j}{R_j}V_{cap} \leq \tau_j^d \leq \frac{a_j}{R_j}V_{cap} \quad (4.75b)$$

$$q_{t=0} = q_i \quad \dot{q}_{t=0} = \dot{q}_i \quad (4.75c)$$

$$q_{t=t_f} = q_f \quad \dot{q}_{t=t_f} = \dot{q}_f \quad (4.75d)$$

We assume that all motion and control trajectories of other joints not considered in the optimization are fixed. The bounds for the controls  $\tau^d$  are obtained from the requirement  $|r_j| \leq 1$  and Eq. (2.6), where the available capacitor voltage  $V_{cap}$  is assumed constant for the purposes of the optimization. Trajectories start from the initial position  $q_i$  and initial velocity  $\dot{q}_i$ , and reach the final position  $q_f$  with final velocity  $\dot{q}_f$  at time  $t_f$ .

As a case study, we consider finding optimal trajectories for a PUMA 500 robot. However, the methods used here are applicable to any robotic manipulator that can be modeled as in Eq. (2.3). The PUMA robot shown in Fig. 29a consists of three main joints and a spherical wrist, which together provide six degrees of freedom for the robot. Here, we only consider the dynamics of the three main joints of the robot which have the most potential for energy regeneration. The three main joints,  $q_1$ ,  $q_2$ , and  $q_3$ , are assumed to be semi-active and connected in the star configuration via a central ultracapacitor. The robot is constrained to start from the initial position  $q_i = [0, -\pi/2, 0]$  (in joint space) and initial velocity  $\dot{q}_i = [0, 0, 0]$  – referred to as Point A – and finish at  $q_f = [\pi/3, 0, \pi/4]$  with  $\dot{q}_f = [0, 0, 0]$  – referred to as Point B. These two points are shown in Fig. 29b.

Using the linear parameterization property for robotic manipulators [96] and assuming no external forces and moments are applied to the robot ( $\mathcal{T} = 0$ ), the

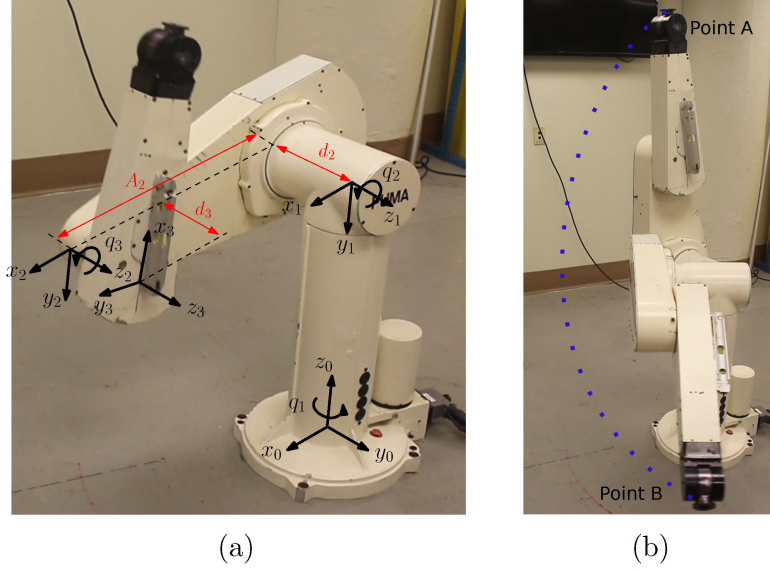


Figure 29: a) The PUMA 500 robot used as a case study for finding optimal trajectories that maximize energy regeneration. Coordinate frames for modeling the PUMA robot are assigned using the Denavit-Hartenberg convention. b) Starting position (Point A) and the final position (Point B) for the PUMA robot.

dynamic equations for the PUMA robot (Eq. (4.75a)) can be written as

$$Y(q, \dot{q}, \ddot{q})\theta + \mathcal{R}(q, \dot{q}) = \tau^d \quad (4.76)$$

where  $Y_{n \times p}$  is the regressor matrix,  $\theta_{p \times 1}$  is the parameter vector, and  $\mathcal{R}$  includes the linear/nonlinear damping and frictional effects for the robot joints and the drive mechanism. Here, joint friction is modeled as a linear damping term

$$\mathcal{R}_j = \frac{a_j^2}{R_j} \dot{q}_j + b_j \dot{q}_j \quad (4.77)$$

Using the Denavit-Hartenberg (DH) convention [96], dynamic equations for the PUMA robot and the semi-active drive mechanisms are derived. These equations are presented in regressor and parameter vector form in Appendix B. Figure 29a shows coordinate frames assigned for the PUMA robot using the DH convention.

The optimal control problem defined in Eq. (4.74) and Eq. (4.75) is in gen-

eral nonlinear and non-convex. It can have none, one, many, or an infinite number of solutions. When no immediate analytical solution exists, one normally resorts to numerical methods for solving the problem. The optimality conditions for this problem (Eq. (4.12)) generally lead to a set of differential equations with split boundary conditions. Methods such as steepest descent and variation of extremals are used for solving these types of two point boundary value problems [57]; we have taken an alternative approach to solve the problem numerically.

After deriving dynamic equations for the PUMA robot and the regenerative semi-active joints, we use the method of direct collocation [84, 105, 108] to transcribe the optimal control problem into a large-scale nonlinear program (NLP) problem. In this method, the states  $(q, \dot{q})$  and controls  $(\tau^d)$  are discretized into  $N$  temporal nodes. The cost function (Eq. (4.74)) and constraints (Eq. (4.75)) are discretized by using an appropriate finite difference approximation for the state derivatives; here, we use the backward Euler approximation. The cost function becomes a function of the states and controls at each grid point, and the dynamic constraints are converted into a set of algebraic constraints that are also a function of the discretized states and controls. The optimal control problem is converted to a constrained optimization problem of finding the states and controls at each grid point that minimize the discretized cost function and satisfy a set of algebraic constraints.

#### 4.6.2 Numerical Optimization Results

The code used to numerically solve the optimization problem considered here can be downloaded from [14]. The direct collocation problem is solved using the IPOPT (interior point optimizer) numerical solver [109]. The IPOPT solver generally finds local optima for nonlinear problems. Optimization is run several times starting from different random initial conditions to find the best possible solution. In addition, using successive mesh refinement, the value of  $N = 100$  was found for which the

Table IV: Nominal values for  $R$ ,  $a$  and  $b$  taken from [17].

	$R$ ( $\Omega$ )	$a$ (Nm/A)	$b$ (N.m.s)
Joint 1	2.1	13.64	8.26
Joint 2	2.1	23.54	8.53
Joint 3	2.1	12.96	3.02

results of the optimization showed little variation with respect to the value of  $N$ . Each optimization problem is solved in 400 – 900 iterations, depending on the case and the initial conditions, and takes approximately 25 – 55 seconds on a computer equipped with *Intel Core i7-5600U* CPU running *Matlab R2018a*.

The nominal parameter vector for the PUMA 500 robot is calculated by using robot parameters given in [17]

$$\theta = \begin{bmatrix} 1.6858 \text{ kgm}^2 & 2.0953 \text{ kgm}^2 & 0.1699 \text{ kgm}^2 & 0.4477 \text{ kgm}^2 & -0.1556 \text{ kgm}^2 \\ 2.5352 \text{ kgm}^2 & 0.3099 \text{ kgm}^2 & -1.2254 \text{ kgm}^2 & 10.1710 \text{ Nm} & 57.1684 \text{ Nm} \end{bmatrix} \quad (4.78)$$

The values for  $R$ ,  $a$ , and  $b$  are also taken from [17] and given in Tab. IV.

The optimization was run once from a starting point  $A$  to the final point  $B$ , and once from  $B$  back to  $A$ . The capacitor voltage during the optimization was assumed to be a constant 27 V for the purpose of the optimization. This limits the control torques to  $[-175, 175]$  Nm,  $[-303, 303]$  Nm and  $[-167, 167]$  Nm for Joints 1, 2, and 3 respectively.

Figure 30 shows the optimal trajectories and controls found, and Fig. 31 shows the power flows for each joint. Power is positive when it flows from the capacitor of the semi-active joint to the robot joint (power is consumed), and is negative when it flows back from the robot joint to the capacitor (power is regenerated).

Table V compares the energy consumption of each joint when going from  $A$  to  $B$  and vice versa. Positive energy indicates energy consumption, and negative energy

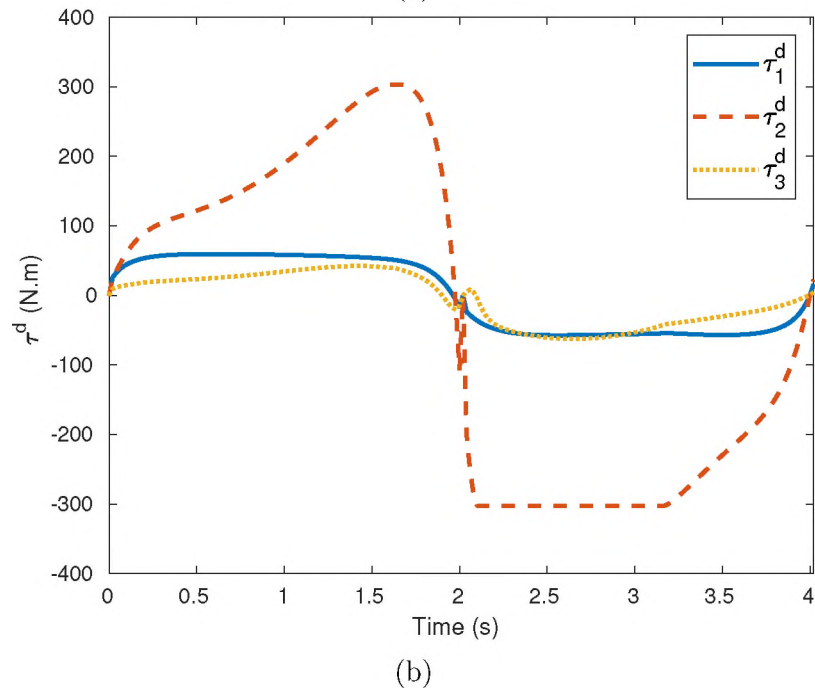
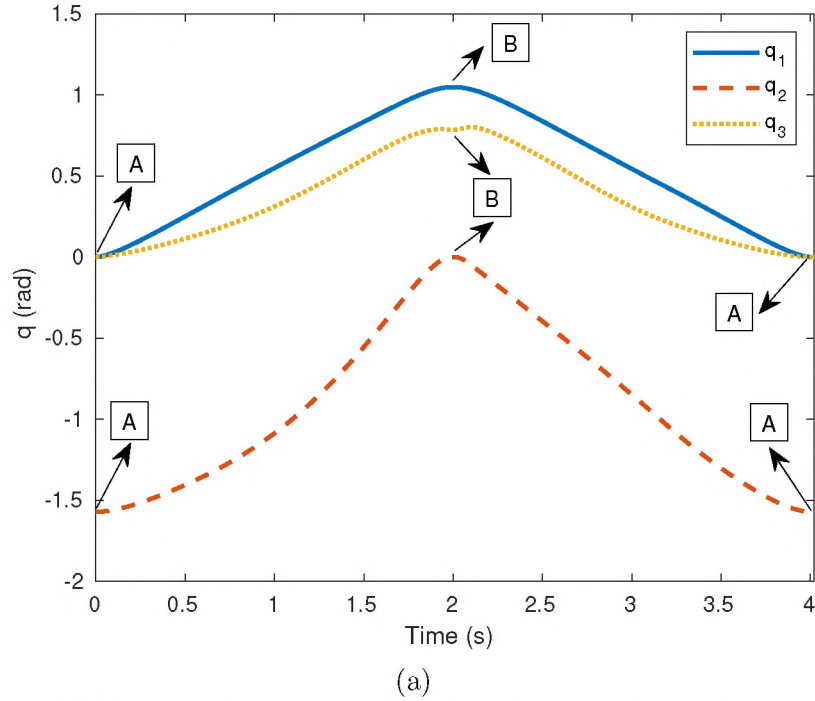


Figure 30: Optimal trajectories and controls found for the PUMA 560 robot, a) optimal trajectories from point  $A$  (starting point) to point  $B$  (final point), and from point  $B$  to point  $A$ , b) the optimal virtual controls ( $\tau^d$ ). Controls are bound between  $[-175, 175]$  Nm,  $[-303, 303]$  Nm and  $[-167, 167]$  Nm for Joints 1, 2, and 3 respectively.

indicates energy regeneration. From Tab. V and Fig. 31, we can see that from  $A$  to  $B$ , Joint 2 and Joint 3 are regenerating energy while Joint 1 is consuming energy;



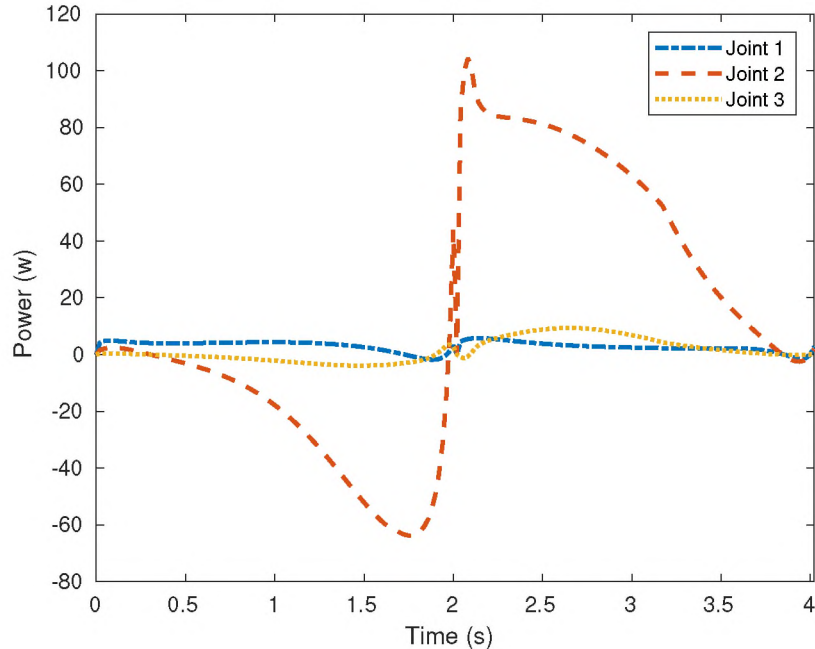


Figure 31: Power flows for the joints of the the PUMA 500 robot when following the optimal trajectories. Power is consumed when positive, and regenerated when negative.

from  $B$  to  $A$  however, all joints are consuming energy. These results are somewhat expected since at point  $B$ , Joint 2 and Joint 3 are at a lower potential energy level compared point  $A$ . Therefore, the potential energy difference between points  $A$  and  $B$  is being regenerated and partially stored in the common capacitor. We also observe that Joint 2 is the main contributor to energy regeneration when going from  $A$  to  $B$ . This is due to Joint 2 supporting the large weight of the second and third links of the robot and motion in a vertical plane. When going from  $B$  to  $A$ , the capacitor needs to provide the potential energy difference between the two points to move the robot back to point  $A$ .

#### 4.7 Remarks

In this chapter, we investigated several trajectory optimization problems pertaining to energy regenerative robots. Assuming given system parameters and using the framework in Chapter II, we considered problems where closed-form solutions were

Table V: Energy consumption for each joint of the PUMA 560 robot when the joints follow optimized trajectories. Positive energy indicates energy consumption, negative energy indicates energy regeneration.

	$E_{A \rightarrow B}(J)$	$E_{B \rightarrow A}(J)$
Joint 1	6.22	5.46
Joint 2	-46.72	101.81
Joint 3	-3.10	8.89

attainable. These problems included finding the optimal external force/moment trajectory that maximizes energy regeneration, where a closed-form solution was found that was shown to be global and unique. In addition, an explicit expression for the maximum energy regeneration was derived which depended on only the trajectory followed by the robot and the actuator parameters of the semi-active joints.

We also derived closed-form solutions for a more general trajectory optimization problem with respect to any variable satisfying a set of conditions (Eq. (4.36) to Eq. (4.38)). The problem was formulated to maximize energy regeneration in one or many semi-active joints. Closed form solutions were found that were shown to be global and unique. For each problem, simulation examples using the double pendulum cart system were provided to demonstrate the results.

Furthermore, we considered the linear optimal control problem, where we aimed to find optimal control and motion trajectories that maximize energy regeneration for linear time invariant systems. Closed form equations expressing the optimal solution and the maximum attainable energy regeneration were presented.

For cases where the robotic system cannot be model linearly, the general non-linear optimal control problem must be solved. However, for this problem, closed-form analytical solutions are not always possible; hence we resort to numerical methods for finding the optimal solution. The PUMA 500 robot is used as a case study, and the problem is formulated to find point-to-point trajectories maximizing energy regener-

ation. We use the method of direct collocation to transcribe the problem into a large scale nonlinear programming problem, and use the IPOPT numeric solver to find the solution. The results found that Joint 2 of the PUMA robot was the main contributor to energy regeneration, which can be due to the large weight of the second and third links of the robot and motion in the vertical plane. In addition, observing the overall energy balance equation (Eq. (2.14)) for this case study, we can see that all the robot joints are semi-active ( $W_{act} = 0$ ), there are no external forces or moments being applied to the system ( $W_{ext} = 0$ ), and the initial and final configurations of the robot are constrained ( $\Delta E_m^T$  is constant). Therefore, maximizing energy regeneration ( $\Delta E_s$ ) is equivalent to minimizing energy consumption ( $W_{ext} - \Delta E_s$ ), and equivalent to minimizing electrical and mechanical losses ( $\Sigma_m^T + \Sigma_e$ ).

**CHAPTER V**

**EXPERIMENTAL EVALUATION OF OPTIMAL TRAJECTORIES  
FOR THE PUMA 500 ROBOT**

**5.1 Introduction**

In this chapter, we present the experimental evaluation of point-to-point optimal trajectories for the PUMA 500 robot having custom regenerative drives. To do so, we initially identify the parameters of the robot model in Appendix B, and derive optimal trajectories for the robot using the methodology of Section 4.6 in Chapter IV. Tracking of optimal trajectories is enforced on the robot using a standard robust passivity based control approach. Power flows, stored regenerative energy, and efficiency are then evaluated to demonstrate the effectiveness of energy regeneration.

The problem is formulated as in Section 4.6, where we consider the first three joints of the PUMA 500 robot  $(q_1, q_2, q_3)$ , that are semi-active and connected to a central capacitor in the star configuration. The robot starts from the initial position  $q_i$  and zero initial velocity ( $\dot{q}_i = [0, 0, 0]$ ), and moves to  $q_f$  with zero terminal velocity ( $\dot{q}_f = [0, 0, 0]$ ). Three optimal trajectories with different starting and ending positions are considered. These points are given in Tab. VI and also shown in Fig. 32.

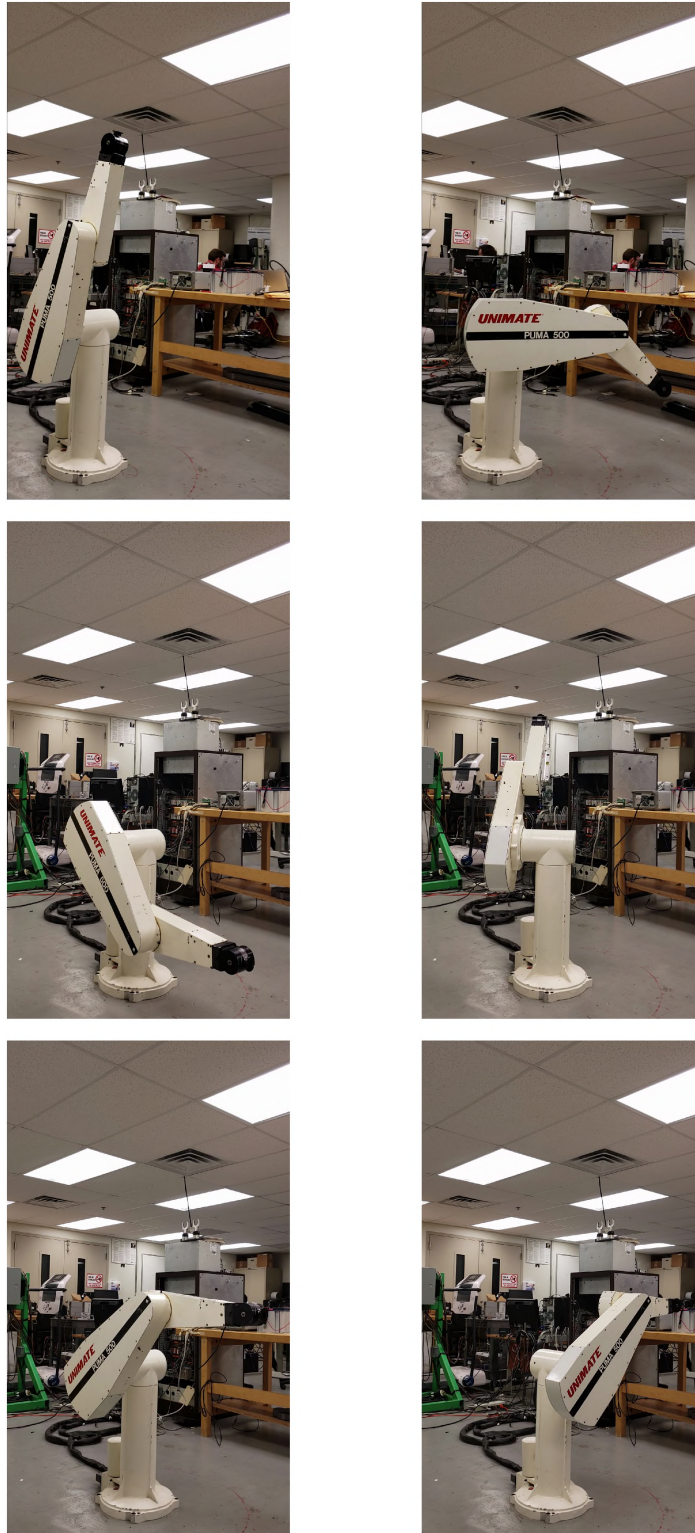


Figure 32: Initial (Point  $A$ ) and final (Point  $B$ ) configurations for the three studied cases. first row) Case 1, second row) Case 2, third row) Case 3, first column) initial configuration, second column) final configuration.

Table VI: Starting and ending constraints (in joint space) for the three optimal trajectories. Trajectories start at point A ( $q_i, \dot{q}_i$ ) and terminate at time  $t_f$  at point B ( $q_f, \dot{q}_f$ ). Initial and terminal joint velocities are zero for the three trajectories (i.e.,  $\dot{q}_i = [0, 0, 0]$  and  $\dot{q}_f = [0, 0, 0]$ ).

	$q_i$ (rad)	$q_f$ (rad)	$t_f$ (s)
Case 1	$[0, -2\pi/5, 0]$	$[\pi/3, 0, \pi/4]$	2
Case 2	$[0, \pi/4, -\pi/4]$	$[-\pi/4, -3\pi/4, 0]$	4
Case 3	$[0, -\pi/4, \pi/4]$	$[\pi/2, -\pi/4, \pi/4]$	8

## 5.2 Parameter Identification for the PUMA 500 Robot

In all the optimization problems considered, a sufficiently accurate model of the system is necessary for the results to have any practical value. In this section, we present methods that were used to identify the system parameters of the PUMA 500 robot.

The PUMA 500 model can be expressed as in Eq. (4.76), where the regressor and the parameter vector are given in Appendix B.  $\mathcal{R}$  consists of the back EMF damping term ( $a^2/R$ ) and the combined nonlinear friction and damping effects of the robot joints and drive mechanism. In place of the linear friction model used in Section 4.6, we use the nonlinear friction model taken from [67] that is simplified by neglecting the Stribeck effects according to [71]. For the  $j$ -th link

$$\mathcal{R}_j = \frac{a_j^2}{R_j} \dot{q}_j + \gamma_{j1} \tanh(\gamma_{j2} \dot{q}_j) + \gamma_{j3} \tanh(\gamma_{j4} \dot{q}_j) + \gamma_{j5} \dot{q}_j \quad (5.1)$$

where constants  $\gamma$  are parameters of the friction model.

Link length values  $A_2$ ,  $d_2$ , and  $d_3$  are taken from [17] and verified by measuring the robot. The motor resistances,  $R_j$  and the parameter  $a_j = \alpha_j n_j$  are derived from rearranging the electrical side equation for the regenerative drive (Eq. (2.8)),

$$a_j \dot{q}_j - R_j \frac{i_j}{r_j} = r_j V_{cap} \quad (5.2)$$

Table VII: Measured values for  $R$  and  $a$ .

	$R$ ( $\Omega$ )	$a$ (Nm/A)
Joint 1	2.52	13.96
Joint 2	2.71	22.57
Joint 3	2.19	12.36

and finding the least square solution by applying various trajectories for  $r_j$  and measuring the resulting  $\dot{q}_j$ ,  $i_j$ , and  $V_{cap}$ . Table VII lists these values.

All other system parameters (i.e., link masses, link inertias, friction constants, etc.) are found by solving a constrained optimization scheme based on Eq. (4.76), where the robot follows specially constructed trajectories ( $q^e$ ,  $\dot{q}^e$ ,  $\ddot{q}^e$ ). System parameters are found that minimize the root mean squared error (RSME) of the measured virtual control ( $\tau_{exp}^d$ ) and the virtual control derived from Eq. (4.76) ( $\tau_{model}^d$ ).

$$\min_{\text{System Parameters}} RSME(\tau_{exp}^d - \tau_{model}^d) \quad (5.3)$$

$$\text{Lower Bound} \leq \text{System Parameters} \leq \text{Upper Bound}$$

To facilitate the numerical optimization, excitation trajectories are found by solving a separate optimization problem similar to what was done in [71]. The trajectories of the  $j$ -th joint are represented as a finite Fourier series

$$\begin{aligned} q_j^e(t) &= \sum_{i=1}^N \frac{\mathcal{A}_i}{\omega_{fi}} \sin(\omega_{fi}t) - \frac{\mathcal{B}_i}{\omega_{fi}} \cos(\omega_{fi}t) \\ \dot{q}_j^e(t) &= \sum_{i=1}^N \mathcal{A}_i \cos(\omega_{fi}t) + \mathcal{B}_i \sin(\omega_{fi}t) \\ \ddot{q}_j^e(t) &= \sum_{i=1}^N -\mathcal{A}_i \omega_{fi} \sin(\omega_{fi}t) + \mathcal{B}_i \omega_{fi} \cos(\omega_{fi}t) \end{aligned} \quad (5.4)$$

where  $\omega_f$  is the fundamental frequency. The Fourier series coefficients  $\mathcal{A}_i$  and  $\mathcal{B}_i$  are found by minimizing the condition number ( $cond()$ ) and maximizing the minimum

singular value ( $\sigma_{max}()$ ) of the regressor matrix  $Y$ .

$$\min_{q^e, \dot{q}^e, \ddot{q}^e} J = \lambda_1 \text{cond}(Y) + \lambda_2 \frac{1}{\sigma_{max}(Y)} \quad (5.5)$$

Lower Bound  $\leq q^e, \dot{q}^e, \ddot{q}^e \leq$  Upper Bound

The maximum and minimum singular values of the matrix  $A$  are given by the identities

$$\begin{aligned} \sigma_{max}(A) &= \max_{\|x\|=1} \|Ax\|_2 \\ \sigma_{min}(A) &= \min_{\|x\|=1} \|Ax\|_2 \end{aligned} \quad (5.6)$$

where  $\|\cdot\|_2$  is the 2-norm, and the condition number is defined as [94]

$$\text{cond}() = \frac{\sigma_{max}()}{\sigma_{min}()} \quad (5.7)$$

Excitation trajectories obtained in this manner will ensure minimum sensitivity to measurement noise and model uncertainty when obtaining system parameters [71]. For identifying the parameters of the PUMA robot, we select  $N = 4$  and  $\omega_f = 2\pi/10$ . Figure 33 shows the resulting excitation trajectories. After finding suitable excitation trajectories, the robot is made to follow these trajectories by using the robust passivity based control method (explained in Section 5.4). The optimization problem defined in Eq. (5.3) is then solved to identify system parameters. The resulting parameter vector is

$$\theta = \begin{bmatrix} 3.4677 \text{ kgm}^2 & 0.9129 \text{ kgm}^2 & 0.2377 \text{ kgm}^2 & 0.4387 \text{ kgm}^2 & -0.1525 \text{ kgm}^2 \\ 4.2051 \text{ kgm}^2 & 0.9622 \text{ kgm}^2 & -0.8711 \text{ kgm}^2 & 9.9665 \text{ Nm} & 42.1485 \text{ Nm} \end{bmatrix} \quad (5.8)$$

and the identified  $\gamma$  values for the friction model are given in Tab. VIII. Figure 34 compares the virtual control resulting from the optimized model ( $\tau_{model}^d$ ) and the virtual control measured from the PUMA robot ( $\tau_{exp}^d$ ).



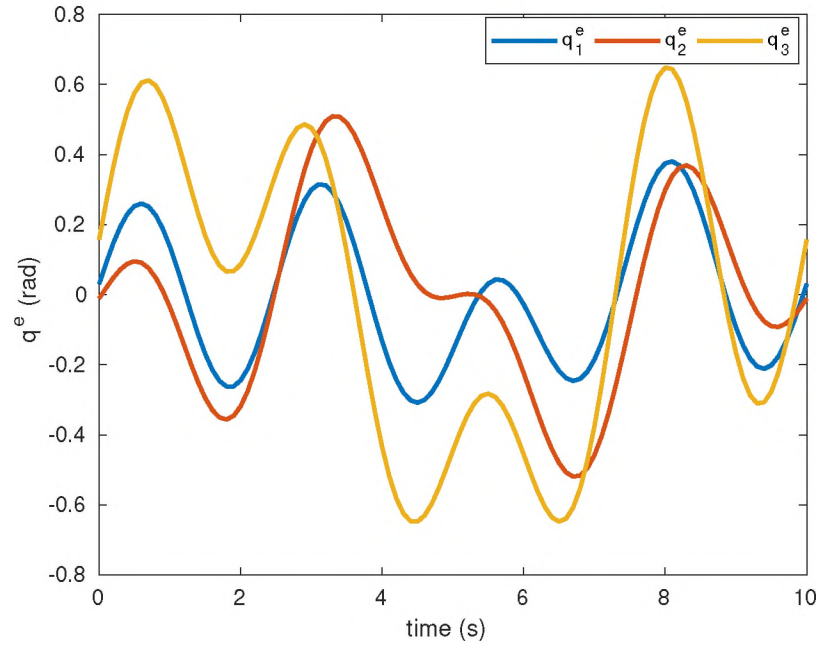


Figure 33: Excitation trajectories found for the purpose of parameter identification.

Table VIII:  $\gamma$  values identified for the friction model.

	$\gamma_1$	$\gamma_2$	$\gamma_3$	$\gamma_4$	$\gamma_5$
Joint 1	3.25	32.64	4.06	734.85	2.13
Joint 2	5.92	92.32	0	267.14	13.26
Joint 3	1.46	189.26	2.80	11.94	0.86

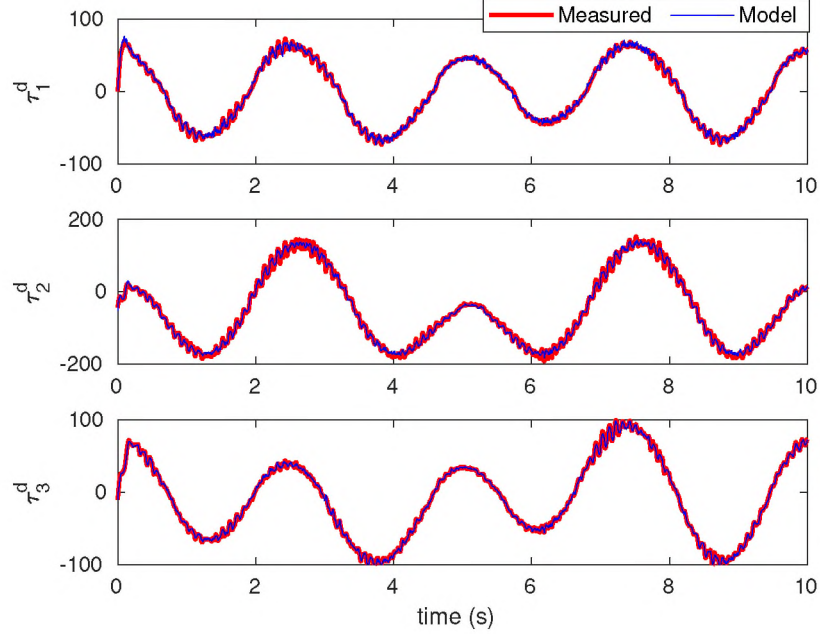


Figure 34: Comparison of the measured ( $\tau_{exp}^d$ ) and modeled ( $\tau_{model}^d$ ) virtual control post optimization.

### 5.3 Experimental Setup

Figure 35 shows the schematic of the experimental setup. The PUMA 500 robot has three main joints and three joints at the wrist. Here we are only concerned with the operation of the main three joints, which have the most potential for energy regeneration. Each joint is actuated by a DC motor that is driven by the four quadrant 25 amp SyRen motor driver (Dimension Engineering, Hudson, Ohio). The dSPACE 1103 controller board (dSPACE GmbH, Paderborn, Germany) is used for controlling the robot and for data acquisition. The input and output voltages and currents for each motor driver are needed to calculate the instantaneous power. The currents are measured via the ACS723 current sensors (Allegro Microsystems, Worcester, Massachusetts). The capacitor voltage is directly measured by using a voltage divider and the dSPACE system. The voltage on the motor side is not directly measured; however, it is verified separately that this voltage accurately follows the voltage requested by the command signal ( $V_{Command}$ ). The input of all three motor

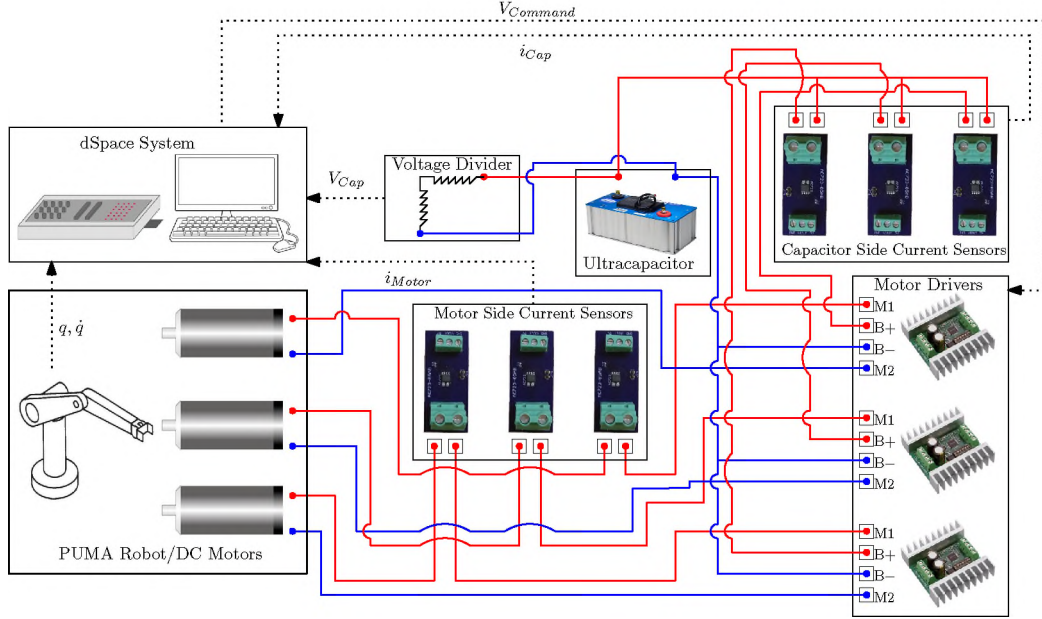


Figure 35: Schematic of the experimental setup. Current sensors are used to measure currents on both sides of each motor driver. Voltage on the capacitor side is measured directly via the dSPACE system. The dSPACE system is also used for controlling the robot. The motor drivers are all connected to a common ultracapacitor (star configuration). Dotted lines indicate signals, solid lines indicate wiring.

drivers are connected to a common 48 V ultracapacitor bank (Maxwell Technologies, San Diego, California) with a capacitance of 165 F. The capacitor is initially charged to 27 V to avoid reaching the 30 V absolute maximum input voltage for the motor drivers. A robust passivity-based control method is used to track the optimal trajectories. The controller is implemented in real time with the dSPACE system and uses angular position and velocity feedback provided by encoders on the robot joints, in addition to capacitor voltage feedback.

#### 5.4 Overview of robust passivity-based control

The optimization problem yields an open-loop control solution which is not implementable in the real robot. The robust passivity-based control [96] was selected to ensure the robot tracks the desired optimal trajectories with guaranteed stability despite parametric uncertainties in the robot model. Based on the dynamic equa-

tion for the augmented model (Eq. (2.3)) and assuming no known external forces or moments are exerted on the robot ( $\mathcal{T} = 0$ ), the control input is chosen as

$$\tau^d = \hat{D}a + \hat{C}\nu + \hat{\mathcal{R}} + \hat{g} - Kr = Y_a(q, \dot{q}, a, \nu)\hat{\theta} - Kr \quad (5.9)$$

where  $Y_a$  is the control regressor and  $\hat{\theta}$  is the parameter estimate adjusted by the control law. Variables  $a$ ,  $\nu$ , and  $r$  are defined as

$$\nu = \dot{q}^d - \Lambda\tilde{q} \quad (5.10a)$$

$$a = \dot{\nu} \quad (5.10b)$$

$$r = \dot{q}^d - \nu \quad (5.10c)$$

where  $q^d$  and  $\dot{q}^d$  denote the desired joint trajectories and  $\tilde{q} = q - q^d$  denotes the tracking error. Also,  $K$  and  $\Lambda$  are diagonal matrices with positive nonzero entries. The parameter estimate  $\hat{\theta}$  is adjusted according to

$$\hat{\theta} = \theta_0 + \delta\theta \quad (5.11)$$

where  $\theta_0$  is a set of constant nominal parameters. If the parametric uncertainty of the system is bounded,  $\|\theta - \hat{\theta}\| \leq \rho$ , then by choosing  $\delta\theta$  as

$$\delta\theta = \begin{cases} -\rho \frac{Y_a^T r}{\|Y_a^T r\|} & \text{if } \|Y_a^T r\| > \epsilon \\ -\frac{\rho}{\epsilon} Y_a^T r & \text{if } \|Y_a^T r\| \leq \epsilon \end{cases} \quad (5.12)$$

where  $\epsilon$  is a small positive parameter, one can show ultimate boundedness of the tracking error.

## 5.5 Experimental Results

We solve the optimization problem formulated in Section 4.6 using the model obtained in Section 5.2, and the direct collocation method, to find the optimal trajectory for each case in Tab. VI. Similar to before, the optimization is run once from point  $A$  to point  $B$ , and once from  $B$  back to  $A$ . The central capacitor is charged to 27 V. For simplicity the capacitor voltage is assumed constant in the optimization. This limits  $\tau_1^d$  to  $[-175, 175]$  Nm,  $\tau_2^d$  to  $[-303, 303]$  Nm, and  $\tau_3^d$  to  $[-167, 167]$  Nm. The optimal trajectories are implemented on the PUMA 500 robot using the robust passivity based control method to ensure trajectory tracking.

Figure 36 shows the optimal trajectories and the actual trajectories followed by the robot joints for each studied case. The videos of the motion trajectories can be found in [15]. We see that the robust passivity based controller provides good tracking of the optimal reference trajectories; however, the controller does lose tracking to a small degree (maximum error of 0.046 radians). This happens due to several reasons. Observing the control input  $\tau^d$  in Fig. 36, we can see that for the second joint in cases 1 and 2, the control torque saturates around  $-222$  N.m. This value is higher compared to the limit set on the control torque for the optimization ( $-224$  N.m), which was set assuming a constant capacitor voltage of 27 V. However, the capacitor voltage does not stay constant during the movement of the robot, as seen in Fig. 37. For example, in Case 1, the capacitor voltage is about 26.84 V at the beginning of the movement and varies between 26.91 and 26.45 V. Since the capacitor voltage is less than the 27 V assumed for the optimization, we can conclude that capacitor voltage is lower than what is needed to follow the optimum trajectory for Joint 2. One could achieve more accurate results by including the ultracapacitor model in the optimization; however, doing so would significantly increase the complexity of the problem. Ultracapacitors exhibit nonlinear and complex behavior and their models do not represent all the aspects of the ultracapacitor's performance [6, 7, 13, 28].

By feeding back the capacitor voltage, SVC allows the control of the robot without being concerned with the nonlinear behavior of the ultracapacitor. In addition, for the robot joints that do not reach the torque saturation limit, better tracking performance could have been achieved by increasing the gains of the robust controller; however, as explained later, higher gains lead to control signal chattering, which in turn results in significant reduction of motor driver efficiency to regenerate energy.

Figure 38 to Fig. 40 show power flows for the motor side and capacitor side of the motor drivers for each case. Power is positive when it flows from the ultracapacitor to the motor driver and from the motor driver to the robot joints. Table IX summarizes the energy consumed by the robot while following the optimal trajectories, where negative consumption indicates energy regeneration. Figure 38 to Fig. 40 also compare the measured power with the power predicted by the robot model when following optimal trajectories. In general, the predicted power agrees quite well with the power on the motor side, indicating that a very good model was identified for the system. Some of the relatively small disagreement can be related to the robot losing track of the optimal trajectories. Results also show that the power on the capacitor side is higher than the power on the motor side. This reflects the inefficiency of the motor driver (some power is dissipated in the motor driver) and also the power required to operate the motor driver. These inefficiencies are not taken into account by the optimization (we have considered an ideal motor driver in the model).

Observing the external energy equation (Eq. (2.14)) for our case study, we note that all joints are semi-active ( $W_{act} = 0$ ) and no external forces or moments are present ( $W_{ext} = 0$ ); therefore, energy stored in the ultracapacitor can only be a result of a change in the mechanical energy of the system. In Case 1, the robot trajectory starts from a higher potential energy level compared to the ending configuration when going from  $A$  to  $B$ . As a result, a portion of this difference in potential energy is regenerated and stored in the ultracapacitor by Joint 2 and 3, and the rest is lost as

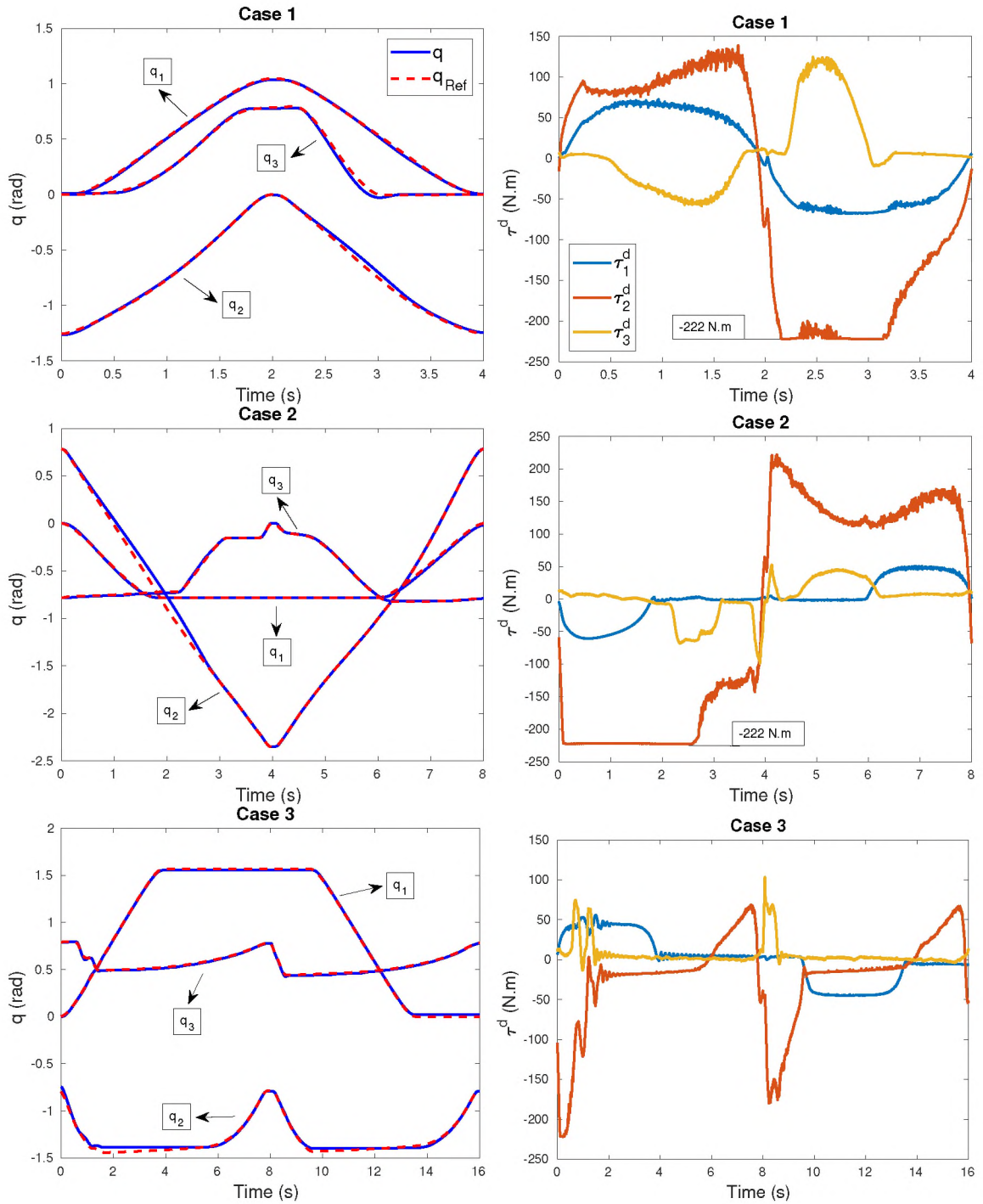


Figure 36: first column) Optimal reference trajectories (dotted lines) and actual trajectories (solid lines) followed by the PUMA 500 robot. Trajectories go from point  $A$  to point  $B$ , and vice versa. second column) Control torque commands ( $\tau^d$ ) applied to the robot joints.



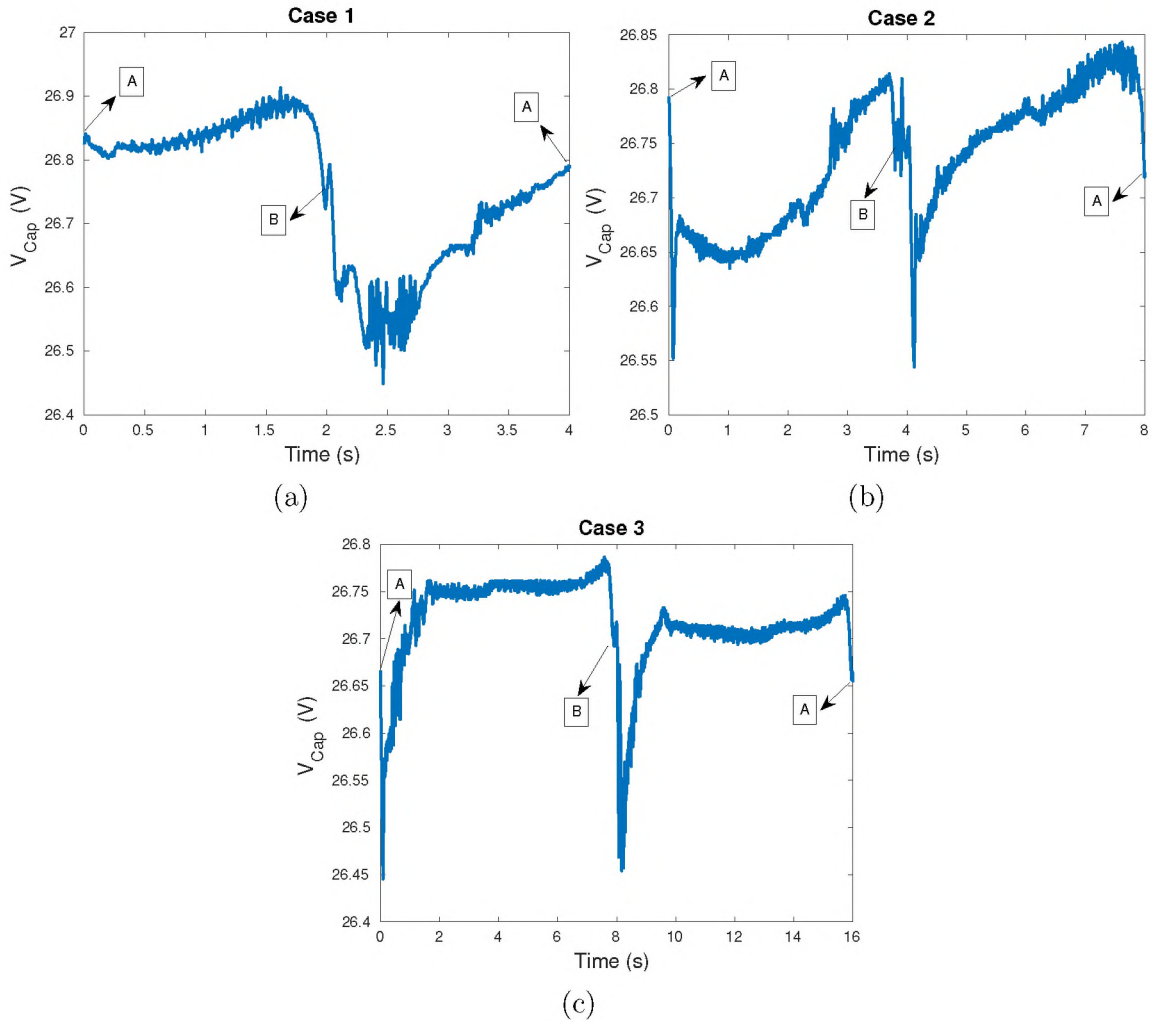


Figure 37: Capacitor voltage for the three studied cases during the movement of the robot.

electrical and mechanical losses. Joint 2 is the main contributor to energy regeneration ( $-24.14$  J from  $A$  to  $B$  with peak negative power of  $-35$  W) due to motion in the vertical plane and a large weight, while joint 1 mostly consumes energy ( $12.10$  J) and only regenerates at the end of the  $A$  to  $B$  portion when the joint is braking and reversing direction. Joint 3 shows portions of negative power on the motor side ( $-1.5$  J energy is regenerated from  $A$  to  $B$  on the motor side) but power on the capacitor side is only positive ( $7.5$  J is consumed on the capacitor side), indicating that the regenerated energy is all dissipated in the motor driver and does not reach the capacitor. In the  $B$  to  $A$  portion, power is positive and energy flows from the



capacitor to the robot (12.34, 99.42, and 14.55 J for joints 1, 2, and 3 respectively). Part of this power is stored as potential energy to move the robot back to point *A* and the rest is lost due to mechanical and electrical losses.

In the *A* to *B* portion of Case 2, the robot starts at a low elevation, goes through an almost vertical position ( $q_2 \approx -\pi/2$  and  $q_3 \approx 0$ ), and comes down to its final configuration. For Joint 2, this results in energy being consumed and converted to potential energy when the robot is moving to a higher potential energy level (from  $q_2 = \pi/4$  to  $q_2 \approx -\pi/2$ ), and regenerated when the robot is moving to a lower potential energy level (from  $q_2 \approx -\pi/2$  to  $q_2 = -3\pi/4$ ). Similarly in the *B* to *A* portion, power is positive when moving to a higher potential energy level ( $q_2 = -\pi/4$  to  $q_2 \approx -\pi/2$ ), and regenerated when going to lower potential energy levels ( $q_2 \approx -\pi/2$  to  $q_2 = \pi/4$ ). Joint 2 is the main contributor to energy regeneration (negative power peak  $-41$  watts). From *A* to *B* Joint 2 consumes a net energy of 160.37 J, and from *B* to *A* it regenerates a net of  $-8.62$  J. Joint 3 is mostly consuming energy and only regenerates when the joint is braking and reversing at the end of the *A* to *B* portion, and Joint 1 is consuming energy throughout the movement of the robot.

The initial and final configurations in Case 3 are chosen such that the robot can reach the final configuration by only moving Joint 1. However, maintaining Joint 2 and Joint 3 at their initial configuration is highly energy consuming. The optimal trajectory moves the robot to a low energy consuming configuration where the power flow for joints 2 and 3 are close to zero. The robot only moves out of the low energy configuration at the end of the trajectory to reach the final configuration. Similar to cases 1 and 2, Joint 2 regenerates energy when moving to a lower potential energy level.

Note that in portions of the robot's movement, when Joint 2 is regenerating energy and Joint 1 and Joint 2 are consuming energy, energy is being channeled from Joint 2 to the other robot joints through the capacitor.

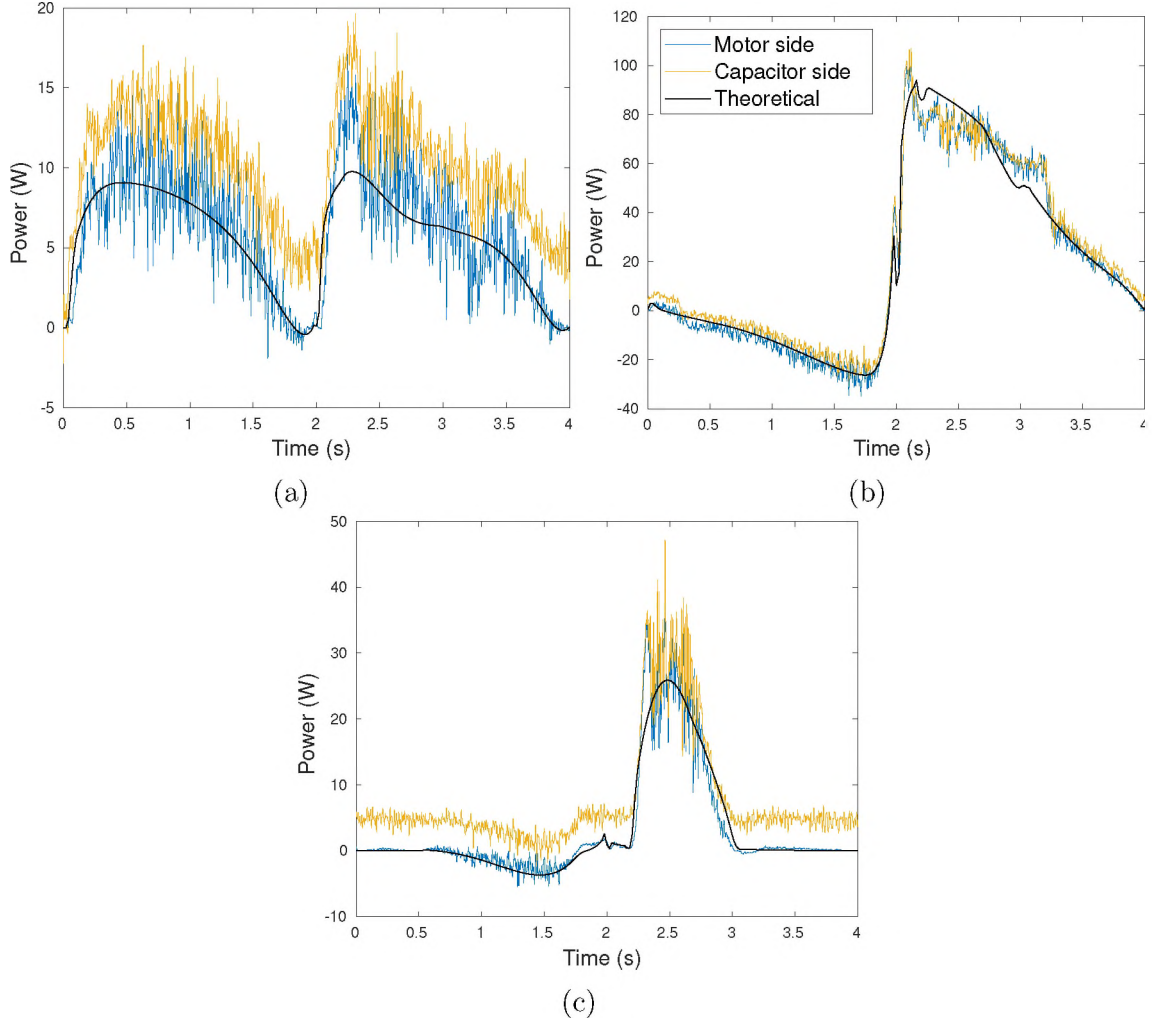


Figure 38: Power flows for the motor side and capacitor side of the motor driver in Case 1 for a) Joint 1, b) Joint 2 and c) Joint 3. Positive power indicates energy consumption and negative power indicates energy regeneration. The theoretical power flow is also shown for comparison.

In addition, note that ultracapacitors exhibit complex and nonlinear dynamic behavior due to the capacitance and ESR (equivalent series resistor) being a function of voltage and frequency [28, 74]. SVC allows us to control the robot without being concerned with the nonlinearities and complexities of ultracapacitor behavior and their effect on the overall performance of the robot.

Figure 41 shows Sankey diagrams for the overall energy balance for Case 1 based on Eq. (2.14) and using model parameters identified for the robot (Section 5.2). Since there is no energy entering the system from an external source (i.e.,  $W_{ext} =$

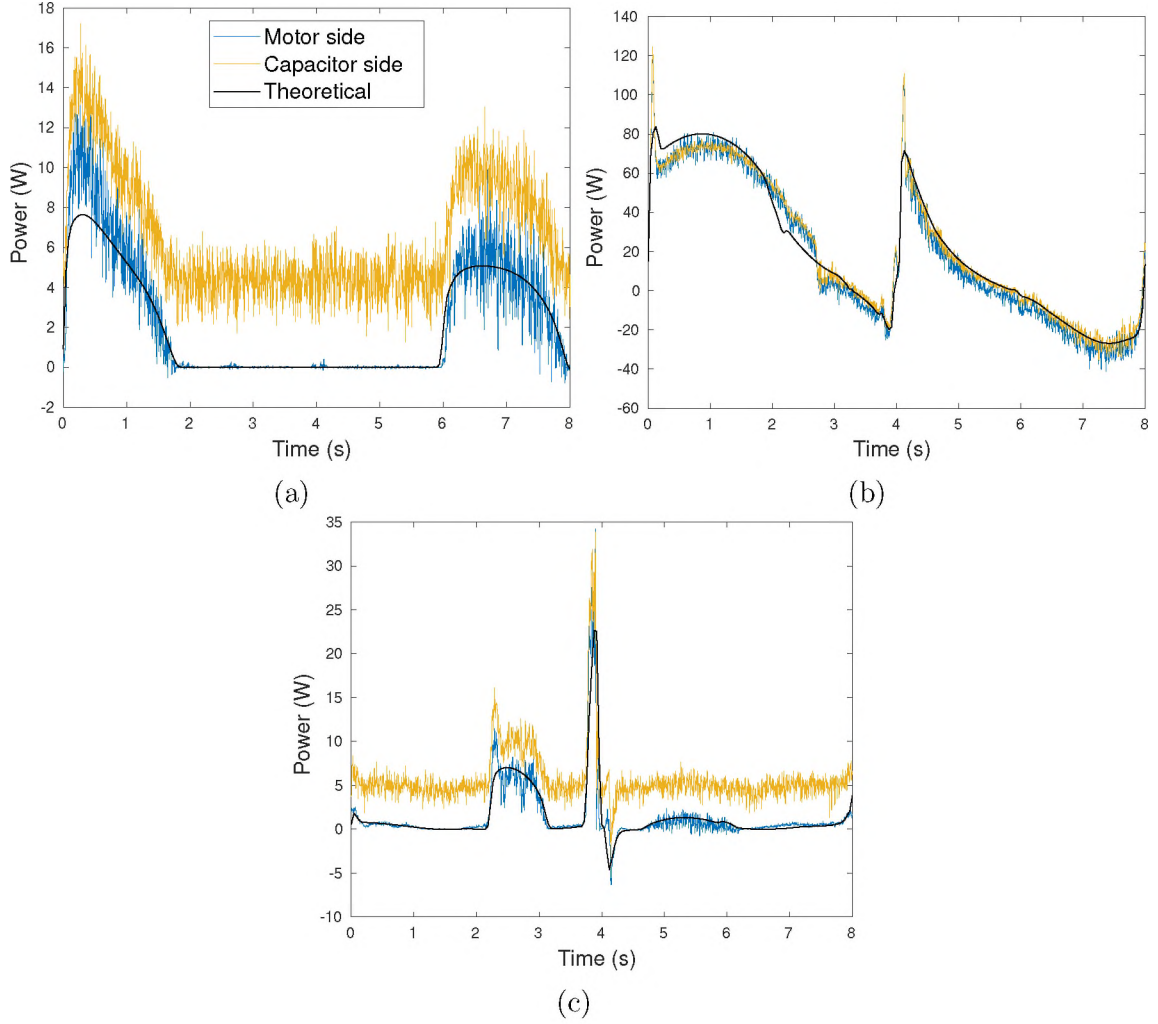


Figure 39: Power flows for the motor side and capacitor side of the motor driver in Case 2 for a) Joint 1, b) Joint 2 and c) Joint 3. Positive power indicates energy consumption and negative power indicates energy regeneration. The theoretical power flow is also shown for comparison.

0 and  $W_{act} = 0$ ), energy can be stored in the capacitor only due to changes in mechanical energy ( $\Delta E_m^T$ ). Also, since the robot trajectories start and end at a stationary configuration (i.e.,  $\dot{q}_s = \dot{q}_f = [0, 0, 0]$ ), the mechanical energy difference between points  $A$  to  $B$  is equal to the potential energy difference. This potential energy difference is 56.40 J for Case 1. In the first portion of the movement, about 49% of the mechanical energy is dissipated as mechanical losses, another 27% is dissipated as electrical losses, and only about 24% reaches the motor drive. Due to inefficiencies in the motor drive only part of that energy is actually stored in the

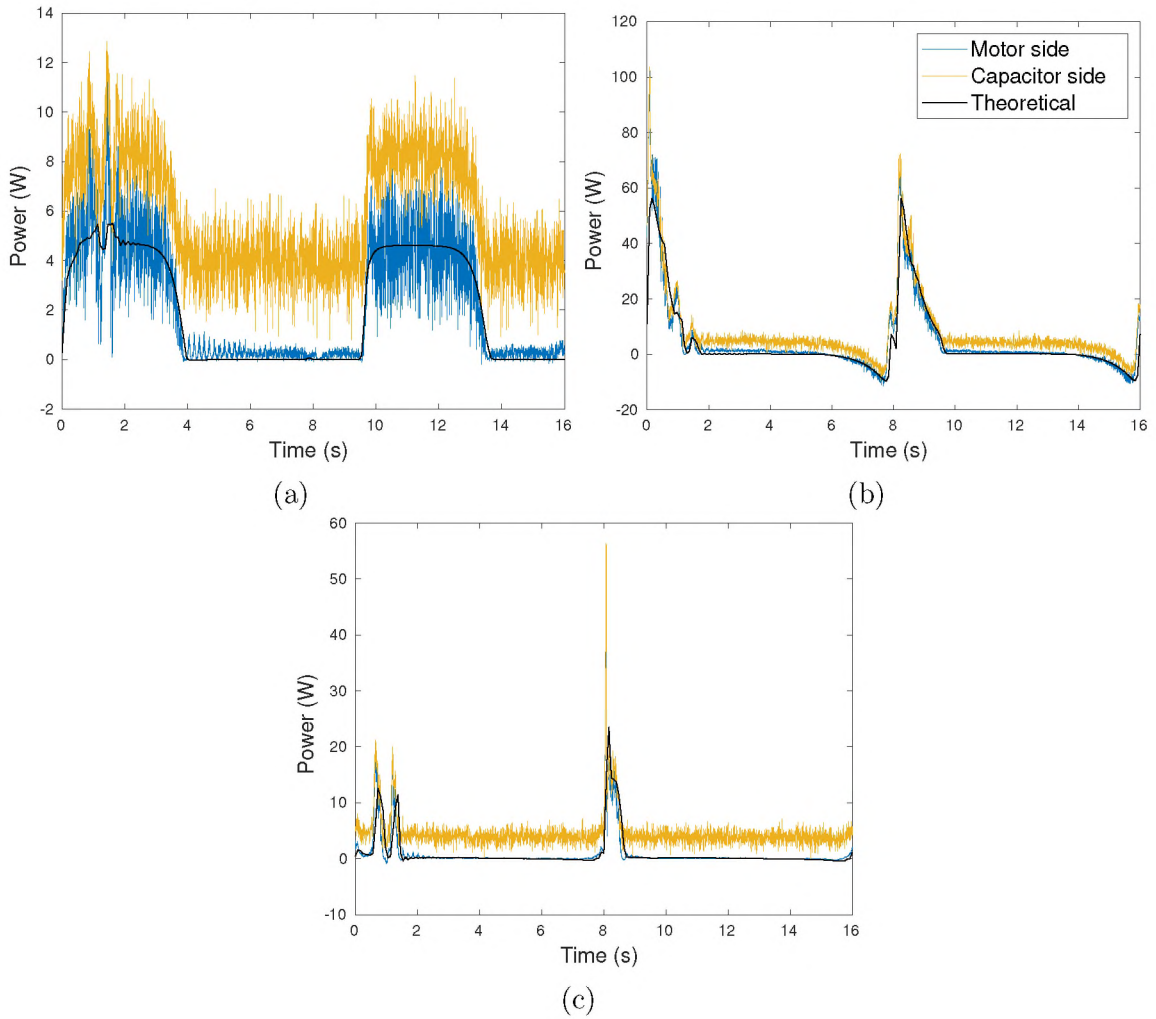


Figure 40: Power flows for the motor side and capacitor side of the motor driver in Case 3 for a) Joint 1, b) Joint 2 and c) Joint 3. Positive power indicates energy consumption and negative power indicates energy regeneration. The theoretical power flow is also shown for comparison.

capacitor; however, by utilizing a high efficiency drive these additional losses can be minimized. In the second portion of the movement, 126.31 J of energy is provided by the driver to move the robot from point *B* to point *A*. Mechanical losses account for about 27% of the provided energy, electrical losses account for about 28% of the provided energy, and only 45% is stored as mechanical energy. These figures indicate that the mechanical losses, which are due to the design of the robot, are a large portion of the total losses and a better robot design can lead to more energy regeneration.

Table IX: Energy consumption for the PUMA 500 robot when following optimal trajectories. Energy consumption is reported for the motor side and capacitor side of the motor driver when going from point  $A$  to point  $B$  and vice versa. Negative energy indicates energy regeneration.

Case 1				
	$E_{A \rightarrow B}(J)$		$E_{B \rightarrow A}(J)$	
	Motor	Capacitor	Motor	Capacitor
Joint 1	12.10	20.16	12.34	20.07
Joint 2	-24.14	-16.21	99.42	103.76
Joint 3	-1.50	7.53	14.55	22.80
Total	-13.54	11.48	126.31	146.63
Case 2				
	$E_{A \rightarrow B}(J)$		$E_{B \rightarrow A}(J)$	
	Motor	Capacitor	Motor	Capacitor
Joint 1	10.34	27.11	7.92	25.72
Joint 2	160.37	168.84	-8.62	7.07
Joint 3	9.51	27.33	1.66	19.73
Total	180.22	223.28	0.96	52.52
Case 3				
	$E_{A \rightarrow B}(J)$		$E_{B \rightarrow A}(J)$	
	Motor	Capacitor	Motor	Capacitor
Joint 1	18.68	46.88	17.20	46.67
Joint 2	42.62	70.10	35.64	63.77
Joint 3	7.05	37.08	7.84	37.47
Total	68.35	154.06	60.68	147.91

We define the effectiveness of energy regeneration as

$$\epsilon = 1 - \frac{\Delta E_R}{\Delta E_{NR}} \quad (5.13)$$

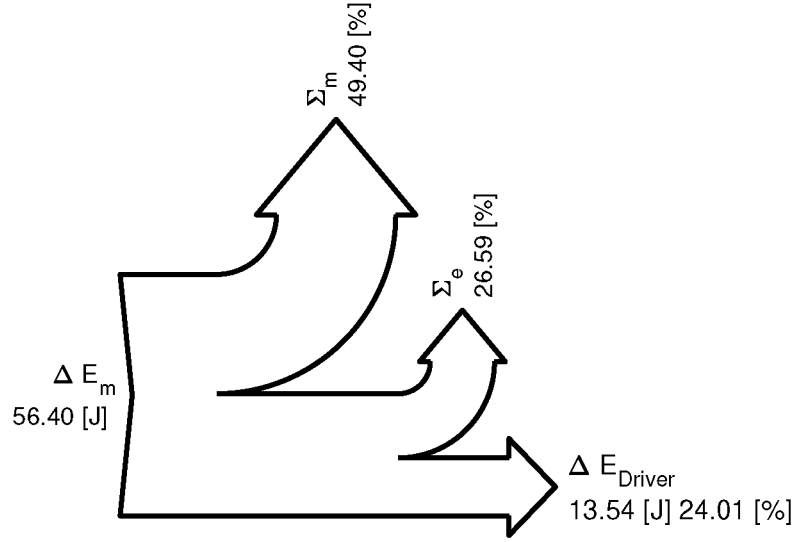
where  $\Delta E_R$  is the energy consumed by the robot in one complete cycle when energy regeneration is enabled, and  $\Delta E_{NR}$  is the energy consumed by the robot in one complete cycle when no energy regeneration capability exists.  $\Delta E_{NR}$  is computed by integrating the power flows for each joint assuming all negative power is dissipated (i.e.,  $P(P < 0) = 0$ ). The effectiveness is a number between 0 and 1, where  $\epsilon = 0$  indicates that energy regeneration has no effect in reducing the energy consumption of the robot, and  $\epsilon = 1$  indicates that energy regeneration reduces energy consumption by 100%. For Case 1,  $\Delta E_R = 113$  J and  $\Delta E_{NR} = 141$  J which results in  $\epsilon = 0.2$ , or in other words a 20% reduction in energy consumption. We use the motor side energy to compute  $\epsilon$  to exclude the deficiencies of the motor driver. For Case 2, a 22% reduction in energy consumption was observed ( $\epsilon = 0.22$ ), and for Case 3, 10% ( $\epsilon = 0.10$ ).

To verify that the optimum trajectories are in fact maxima, two neighboring trajectories are generated and evaluated. In the interest of conciseness, we only consider the *A* to *B* portion of Case 1. Neighboring trajectories are generated by adding a Gaussian function term to the optimum trajectory

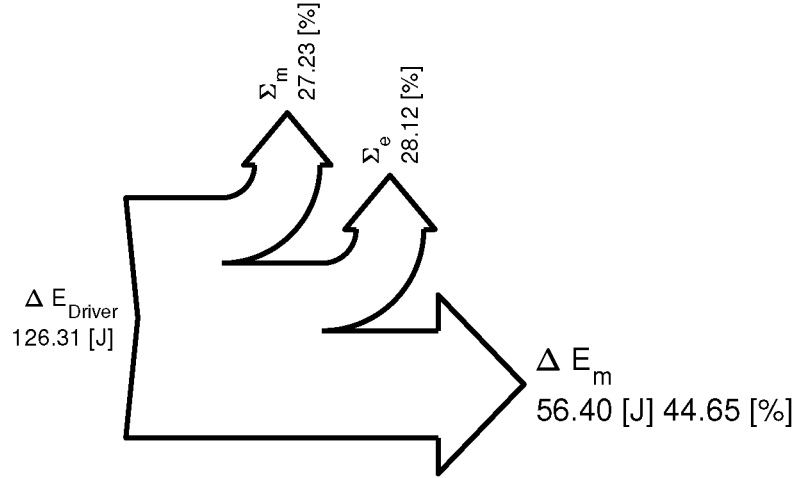
$$q_{neighboring} = q_{optimum} \pm \epsilon e^{-\frac{1}{2}\left(\frac{(t-\mu)^2}{\sigma^2}\right)} \quad (5.14)$$

With  $\mu = 1$ ,  $\sigma = \mu/3$ , and  $\epsilon = 0.2 \max(|q|)$ . Parameters for the Gaussian function are chosen so that the neighboring trajectories satisfy the boundary conditions for the optimal trajectory with negligible error. Figure 42 shows the neighboring trajectories followed by the robot and Table X compares energy consumptions for the optimum and neighboring trajectories. We see that compared to the neighboring trajectories, the optimum trajectory results in the maximum total energy regeneration, even though Joint 3 consumes slightly more energy.

While conducting experiments, we observed that controller chattering had a



(a)



(b)

Figure 41: Sankey diagram showing the overall energy balance for the PUMA 500 robot when following optimal trajectories in Case 1 from a)  $A$  to  $B$  and b)  $B$  to  $A$ . The overall mechanical energy of the robot is represented by  $\Delta E_m$ ,  $\Sigma_e$  and  $\Sigma_m$  are the electrical and mechanical losses respectively,  $\Delta E_{Driver}$  is the energy going to (i.e., regenerated) or coming from (i.e., consumed) the motor driver.

negative effect on regeneration efficiency. Increasing the gains of the robust passivity based controller leads to lower tracking error of the optimum trajectories, but at a cost of increasing control signal chattering, which in turn reduces regeneration efficiency. This is demonstrated in Fig. 43 where we have increased the gains of the robust controller while following the  $A$  to  $B$  portion of the optimum trajectory in Case 1.

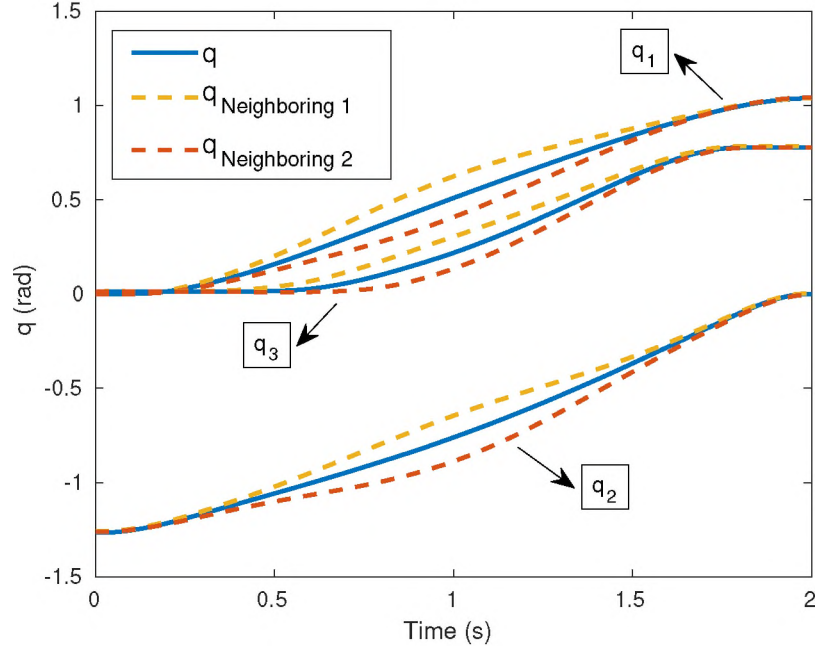


Figure 42: Optimum and neighboring trajectories followed by the robot when going from point  $A$  to point  $B$  in Case 1. Neighboring trajectories are tested to show the effectiveness of the optimization.

Table X: Comparison of energy consumption for the PUMA 500 robot when following optimal and neighboring trajectories. Energy consumption is reported for the motor side of the motor driver when going from point  $A$  to point  $B$  in Case 1. Negative energy indicates energy being regenerated. The neighboring trajectories show a lower amount of total energy regeneration when compared to the optimal trajectory.

	$E_{A \rightarrow B}(J)$		
	Neighboring 1	Neighboring 2	Optimal
Joint 1	12.96	12.95	<u>12.10</u>
Joint 2	-21.25	-22.05	<u>-24.14</u>
Joint 3	<u>-1.91</u>	-1.10	-1.50
Total	-10.20	-10.20	<u>-13.54</u>

Chattering is quantified empirically by summing the magnitude of the fast Fourier transform (FFT) of the control signal between 10 Hz and the Nyquist frequency (500 Hz, one-half of the sampling rate) [82]. Figure 43 shows that as the root mean squared (RMS) tracking error decreases, controller chattering increases. This initially results in a slight increase in energy regeneration (decrease in energy consumption)



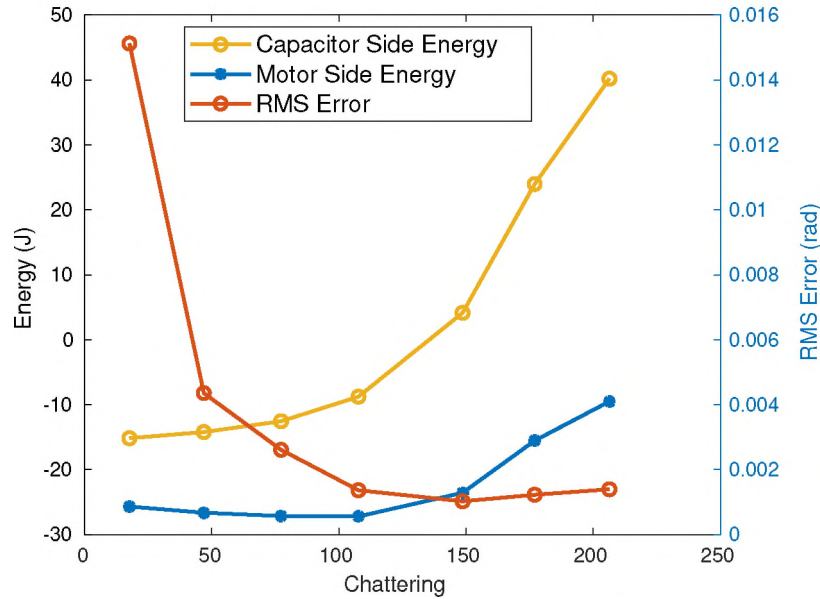


Figure 43: Effect of chattering on energy regeneration.

on the motor side, which can be related to more accurately tracking the optimal trajectory, but significantly decreases energy regeneration on the capacitor side as a result of decrease in motor driver efficiency. After a certain point, further increases in chattering significantly decrease energy regeneration on both motor and capacitor sides of the motor driver. Therefore, there is a compromise between how well the optimal trajectories are followed, and control signal chattering, and in certain cases it is necessary to give up trajectory tracking for more energy regeneration.

## 5.6 Remarks

In this chapter, we experimentally evaluated optimal point-to-point trajectories for the PUMA 500 robot. Based on the nonlinear optimal control problem formulated in Section 4.6 of Chapter IV, we find optimal trajectories maximizing energy regeneration using an experimentally identified model for the PUMA 500 robot. The problem is solved numerically and the optimal trajectories are implemented on the PUMA 500 using a robust passivity based controller. Power flows are reported for the motor side and capacitor side of the motor driver. Experimental results show

a good agreement with the theoretical results for the motor side of the motor driver and less agreement with the capacitor side. This is due to the efficiency of the motor driver and the power required to operate it. In addition, due to the fact that there was no energy entering the system from an external source (i.e.,  $W_{ext} = 0$  and  $W_{act} = 0$  in Eq. (2.14)), energy is stored in the capacitor due to only changes in mechanical energy, potential energy being the main contributor. For this reason, we only considered the first three joints of the PUMA 500 robot for optimization, which have potential for energy regeneration – compared to the three main joints, the robot wrist is light weight, has a lot of friction, and moves slowly.

Also, while conducting the experiments, it was observed that controller chattering has a negative effect on energy regeneration. In certain cases it might be necessary to compromise trajectory tracking for more energy regeneration. Using a higher quality motor driver can also mitigate the problems associated with motor driver. On the other hand, including the inefficiencies of the motor driver in the model could provide more energy regeneration by prompting the optimization to look for different trajectories that operate in the efficient range for the motor drivers. Moreover, experimental results for the neighboring trajectories showed the strong dependency of energy regeneration on trajectories followed by the robot joints; thus the need for trajectory optimization. Results also showed that a great portion of the energy is dissipated as mechanical losses due to the robot design. Even with these losses, energy regeneration resulted in about 10 – 22% reduction in the overall energy consumption. In a factory assembly line with many robots, energy regeneration can lead to significant reduction in operating cost.

As part of future research paths, an alternative approach to the one taken here could be to use model predictive control methods to provide optimal feedback directly, as opposed to solving for the optimal trajectory separately and enforcing it via a robust control method. Such an approach provides online calculations of

new optimal trajectories with changes in initial or final positions. Model predictive control involves a moving-horizon implementation of essentially the same optimal control solutions presented in this chapter. The energy-based cost function, however, is not positive-definite relative to any particular equilibrium point, and the required feasibility, stability, and performance analyses fall into the category of *economic model predictive control* [73]. This requires a separate approach, and is a current area under study.

## CHAPTER VI

# DEVELOPMENT AND EXPERIMENTAL EVALUATION OF A POWERED PROSTHETIC KNEE

### 6.1 Introduction

In Chapter I we discussed how energy regeneration can reduce the overall energy consumption of lower limb prostheses, making them more practical for daily use. In this chapter, we present an overview of the design, control, and experimental evaluation of an ultracapacitor based regenerative powered prosthetic knee. The framework presented in Chapter II is used to design and model the powered prosthesis. Our prosthesis prototype is comprised of a passive ankle joint, and a powered knee joint that is actuated by an semi-active ultracapacitor based drive system. We also present a novel varying impedance control approach that drives the prosthesis in both stance and swing phase, while explicitly dealing with energy regeneration. This approach provides a natural variation in the impedance of the knee and leads to far fewer tuning parameters compared to some other approaches [97–100]. In addition, the controller allows walking at different speeds without the need for retuning, and with a simple adjustment, the same tuning can be used for different subjects. The prosthesis is evaluated experimentally by having an amputee test subject walk with the device on a treadmill. This is the first known human trial testing of an electro-mechanical energy-regenerative prosthesis.

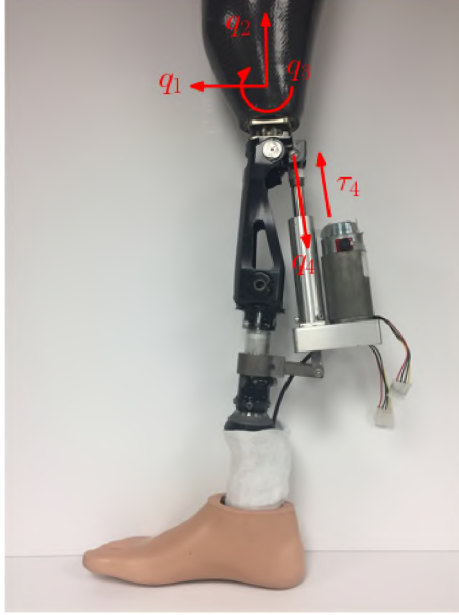


Figure 44: Prosthetic knee prototype with ottobock triton vertical shock foot.

## 6.2 The Regenerative Prosthesis Model

Our prosthetic leg prototype, depicted in Fig. 44, is comprised of a powered regenerative knee joint and a passive ankle joint. To model the system, the prosthesis, excluding the regenerative drive mechanism, can be thought of as a four degree of freedom standard open-chain robotic system. The first three degrees of freedom are the horizontal motion, vertical motion, and rotation of the prosthesis socket in the sagittal plane; the fourth degree of freedom corresponds to flexion/extension of the knee joint. The equation of motion for this system can be expressed using Eq. (2.1).

The motion of the prosthesis socket ( $q_1$ ,  $q_2$ , and  $q_3$ ) is controlled by the human subject and can be thought of as fully-active, injecting energy into the system. The prosthetic knee is connected to a semi-active drive mechanism, where the schematic and bond graph model are depicted in Fig 45. The inertial and frictional effects of the motor are assumed to have been reflected to the transmission and are thereby included in  $m$  and  $b$ . In the most general case, the transmission ratio can be a function of the knee joint angle.

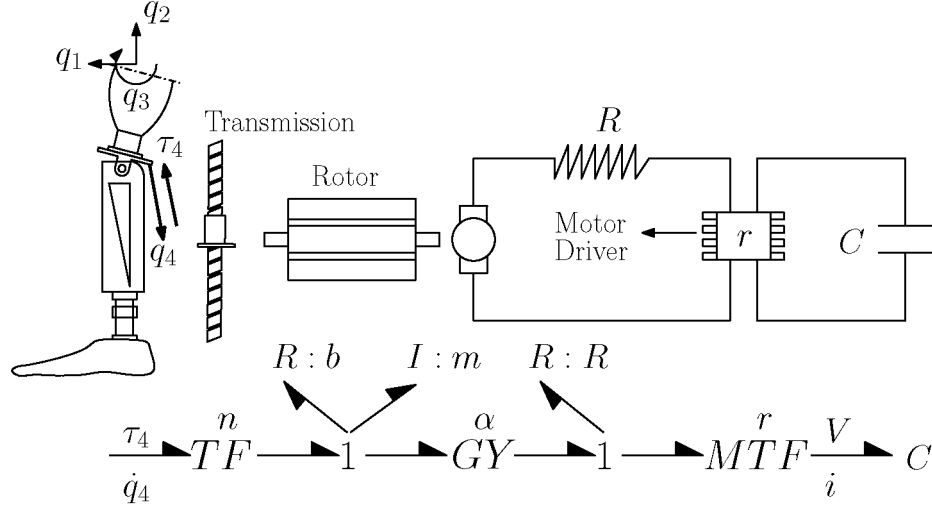


Figure 45: The prosthetic leg with the regenerative drive mechanism and its bond graph representation. The first three joints of the prosthesis are actuated by the human subject and are considered fully-active. The knee joint is regenerative and considered semi-active.

From the bond graph model in Fig. 45, the interfacing force  $\tau_4$  for the knee joint is found as

Substituting  $\tau_4$  from Eq. (6.1) into the dynamic equations for the prosthesis (Eq. (2.1)) and absorbing the terms containing  $\dot{q}$  and  $\ddot{q}$  into the left-hand side, the complete model of the prosthesis with the regenerative drive mechanism is obtained.

$$D(q)\ddot{q} + C(q, \dot{q})\dot{q} + \mathcal{R}(q, \dot{q}) + g + \mathcal{T} = u \quad (6.2)$$

where  $D$  and  $\mathcal{R}$  result from augmenting  $D^\circ$  and  $\mathcal{R}^\circ$  in Eq. (2.1),

$$\begin{aligned} D_{44} &= D_{44}^\circ + mn^2\ddot{q}_4 \\ \mathcal{R}_4 &= \mathcal{R}_4^\circ + (bn^2 + \frac{a^2}{R})\dot{q}_4 \end{aligned} \quad (6.3)$$

The first three joints are actively controlled by the human subject ( $u_{1-3}$ ), and the knee joint is controlled via the semi-active virtual control method.

### 6.3 Variable Impedance Control Method

Many powered lower limb prostheses use impedance control [4, 38, 44, 61, 97]. Impedance control emulates the behavior of physical springs and dampers; any active, variable, and nonlinear behavior can be achieved. For prostheses, power is produced by varying the joint impedance during different gait phases. However, the advantages of impedance control over mechanical springs and dampers, as with any powered control method, come at the price of energy consumption.

The general approach for controlling powered lower limb prostheses is to use a finite state impedance controller which divides the gait into discrete states [3, 4, 44, 61, 63, 68, 97–100, 110]. Each state has its separate controller and transitions between states are triggered by sensors placed on the prostheses. The control parameters for each state are tuned to individual subjects and different walking speeds. A five state controller with three gains per state across three walking speeds can lead to as many as  $5 \times 3 \times 3 = 45$  tuning parameters in addition to gait-phase switching rules [100]. More elaborate methods add variation of the impedance parameters based on joint angles or measured forces during the finite states to reduce the number of tunable parameters [23, 93]. We refer readers to a comprehensive survey [104] of control strategies used for powered lower extremity prostheses.

We use a novel varying impedance control method to control the prosthetic knee. Our approach changes the impedance of the knee joint based on the amount of force applied to the prosthesis' shank. This provides a continuous variation of the knee impedance during the gait cycle and enables a soft transition between the stance and swing phases of gait. Moreover, our approach leads to far fewer tuning parameters when compared to finite state impedance control. Five parameters that are independent of walking speed are identified. Furthermore, once the controller is tuned, the same tuning can be used for different subjects with just a simple adjustment.

The equation describing the control structure is

$$\tau^d = -(B_h + B)\dot{q}_4 - \frac{F}{F_s}Kq_4 - K_s(q_4 - q_4^\circ) \quad (6.4)$$

where  $B$  and  $B_h$  are virtual damping coefficients,  $F$  is the shank force,  $F_s$  is a normalization factor,  $K$  and  $K_s$  are virtual spring stiffnesses, and  $q_4^\circ$  is the equilibrium point of the virtual spring. We explain the controller's functionality in the stance and swing phases separately.

### 6.3.1 Swing Phase

In the swing phase the shank force  $F$  is zero and Eqn. (6.4) reduces to

$$\tau^d = -(B_h + B)\dot{q}_4 - K_s(q_4 - q_4^\circ) \quad (6.5)$$

We mainly rely on the kinetic energy of the prosthesis at the beginning of the swing phase to extend the knee. The virtual stiffness  $K_s$  can be used to further propel the leg if the knee joint does not fully extend before heel strike. During tests with the prototype, we observed that this was not the case and set  $K_s$  to zero.

Virtual damping constant  $B_h$  prevents the mechanical hard stop from making contact at the end of the swing phase and only becomes active when the knee angle approaches full extension, meaning that the screw displacement becomes less than a certain threshold.

$$B_h = \begin{cases} b_h & q_4 < q_{threshold} \\ 0 & q_4 > q_{threshold} \end{cases} \quad (6.6)$$

This could, however, be achieved mechanically by installing a soft stop insert, avoiding the need to expend extra electrical energy.

The purpose of the virtual damping constant  $B$  is to regenerate energy in the swing phase. The damping constant is set by considering the regenerated energy



Eq. (2.10) under the case where  $\tau^d = -B\dot{q}_4$ .

$$\Delta E_s = \int_{t_1}^{t_2} - \left( B + \frac{R}{a^2} B^2 \right) \dot{q}_4^2 dt \quad (6.7)$$

From Eq. (6.7) it can be seen that energy is regenerated ( $\Delta E_s > 0$ ) only if

$$-\frac{a^2}{R} < B < 0 \quad (6.8)$$

Equation (6.8) suggests that power can only be regenerated with a virtual damper if negative damping constants are used. Negative damping constants in the range of Eq. (6.8) reduce the damping of the overall system but not to the extent of causing instability. Assuming that  $\dot{q}_4$  is mostly governed by the system dynamics and varying  $B$  in the range of Eq. (6.8) has negligible effect on  $\dot{q}_4$ , we can differentiate Eq. (6.7) with respect to  $B$  and set it to zero to find the optimum damping constant for regeneration.

$$B^* = -\frac{a^2}{2R} \quad (6.9)$$

and the optimum energy regenerated is

$$\Delta E_s^* = \int_{t_1}^{t_2} \frac{a^2}{4R} \dot{q}_4^2 dt \quad (6.10)$$

Note that this expression is identical to Eq. (4.21). This is to be expected since, assuming  $\dot{q}_4$  is constant with respect to changes in the damping constant,  $B$  satisfies all the conditions for  $x$  in Section. 4.4.

### 6.3.2 Stance Phase

Once the foot makes contact with the ground, the shank force  $F$  is non-zero, reinstating the full control law Eq. (6.4). The virtual spring  $K$  dominates the control in stance phase due to the smaller knee velocities. Also, the virtual spring constant

$K$  is typically set to much larger values compared to  $K_s$ . The stance phase control reduces to

$$\tau^d \approx -\frac{F}{F_s} K q_4 \quad (6.11)$$

The normalization factor  $F_s$  is the measured shank force  $F$  when the amputee is fully supported by the prosthetic leg.

During stance phase the behavior of the control law dictates that as the user shifts his or her weight to the prosthetic leg, the knee will stiffen, providing the amputee with the necessary support even when the knee remains slightly flexed. This is in contrast to the slow collapse of, for example, a hydraulic knee joint under matching conditions. During late stance when the amputee prepares for swing phase and begins to transfer his or her weight to the opposing leg, the proposed control law causes the prosthesis to soften, initializing the knee flexion required to enter swing phase. Each of these transitions are accomplished without switching between multiple sets of control gains.

### 6.3.3 Controller Tuning Procedure

Tuning the control law requires the selection of five values. These are  $b_h$ ,  $q_{threshold}$ ,  $K$ ,  $K_s$ , and  $q_4^\circ$ . Notably,  $B$  is automatically determined by three system parameters; see Eq. (6.9). The parameter  $b_h$  is set to be a little larger than the magnitude of  $B$  so that it cancels the negative damping. The smallest sufficient value of  $q_{threshold}$  to prevent the hard stop is chosen, typically a couple of millimeters.  $K$  is determined by trial and error such that the amputee feels well supported.  $K_s$  and  $q_4^\circ$  are nonzero only when needed and are increased until the knee fully extends under the user's volition. Once this initial tuning is completed, it is expected that other amputees could reuse the same tuning parameters. The value for  $F_s$ , which is specific to the user's weight, would only need to be updated. None of the tuning parameters are dependent on the user's selected speed either. These features of the

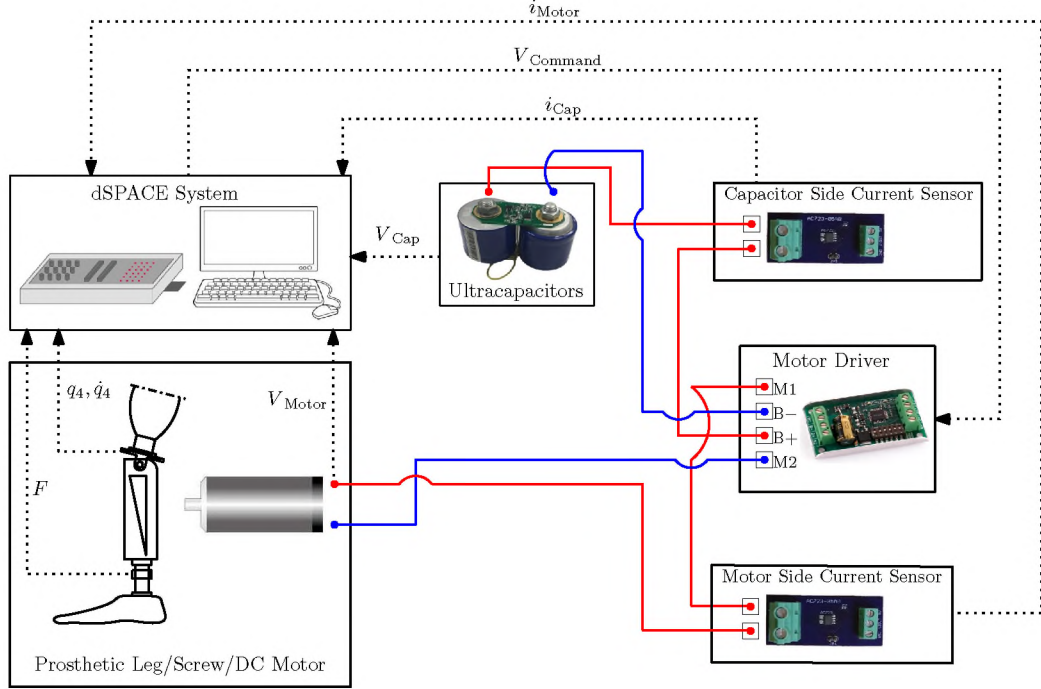


Figure 46: Prosthetic leg system overview indicating power and information paths.

controller make tuning efforts minimal and very straightforward compared to finite state impedance controllers.

## 6.4 The Prosthesis Prototype and Experimental Setup

The prototype used for this work was constructed from off-the-shelf components with an emphasis on creating a low-cost, proof-of-concept system. The overall system can be divided into the following categories: actuation, power storage, control, and sensing. A schematic of the system is given in Fig. 46.

The knee structure was built such that standard pyramid adapters are available at both the thigh and ankle interfaces. Also, it should be noted in relation to stance phase that when the knee is completely straight it can enter a mechanically self-locking region, depending on the location of the user's center of mass. Under this condition  $q_4 = \dot{q}_4 = 0$ , eliminating active power usage and saving energy. The knee attached to a socket and an Ottobock Triton Vertical Shock foot is shown in Fig. 44.

A 12 V DC motor-driven lead screw (ULTRAMOTION) actuates the knee joint by use of the crank-slider architecture. The measured resistance and torque constant for this motor are  $0.27 \Omega$  and  $0.31 \text{ Nm/A}$ . The screw has a transmission ratio of  $n = 989.5 \text{ rad/m}$ . Power is supplied to the motor from four ultracapacitors linked in series by balancing circuitry (Maxwell Technologies, BKIT-MCINT). These capacitors are rated for up to 2.7 V and at 650 F each (Maxwell Technologies, BCAP0650 P270 K04), determining a maximum operating voltage of 10.8 V. Regulating the power flow to and from the motor, a 10 A SyRen motor driver was selected. This device is capable of four-quadrant operation. The analog control signal sent to the motor driver is generated by the dSPACE system, specifically the DS1104. The control software run by this system was developed in Simulink with the more complex computations written directly in MATLAB code.

A variety of sensors were installed for both control feedback and performance evaluation. For feedback, motor position, which is kinematically related to knee angle, was measured by an encoder, from which velocity could be computed. Additionally, two strain gages were adhered to the foot and then calibrated to produce shank force. The capacitor voltage was measured for use in the semiactive virtual control method. To be able to evaluate the energy regeneration capacity of the prosthesis, current sensors were installed at both the input and output to the motor driver; see Fig. 46 for the wiring schematic. The voltage applied to the motor as well as the voltage across the capacitors, as previously mentioned, were recorded. Combining these two pairs of measurements provides information regarding the power usage and the efficiency of the motor driver. All data with the exception of the knee position were passed through a digital filter with a cutoff frequency of 24 Hz.

Human trials with an amputee subject were completed at the Louis Stokes Cleveland VA Medical Center as approved by its internal institutional review board. A 35-year-old male (81.7 kg, 175.3 cm) with a right transfemoral amputation volunteered

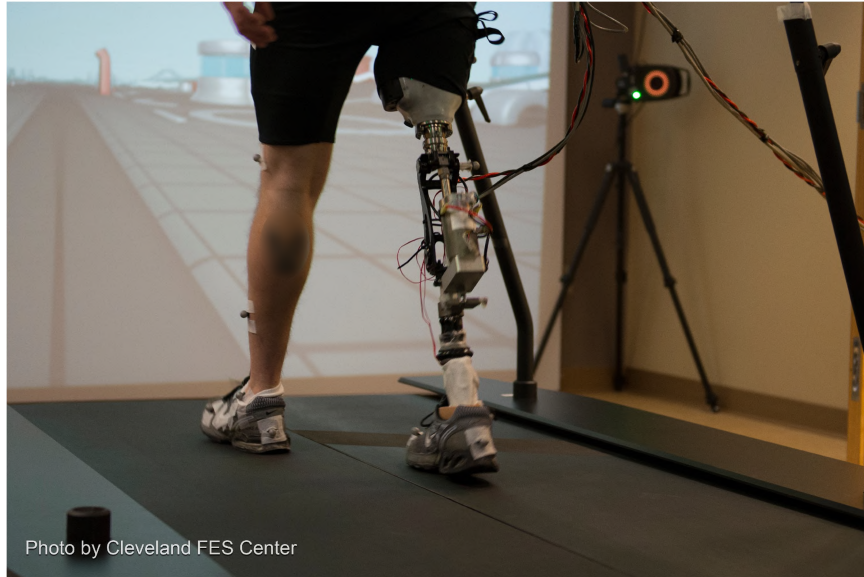


Figure 47: Test subject walking with the prosthesis prototype (Copyright Cleveland FES Center, Cleveland, USA).

to trial the leg; see Fig. 47. The test subject walks with a Freedom Innovations Plie microprocessor-controlled passive knee in combination with an Ottobock Triton Vertical Shock foot on a daily basis. The subject used his personal socket and daily foot for all of the trials. All components were fit by a certified prosthetist.

Three speeds were selected for the trial protocol, which was executed on a treadmill. These were the amputee's preferred speed while using his everyday leg and plus and minus 0.15 m/s, giving 0.6 m/s, 0.75 m/s, and 0.9 m/s. All test data were taken on the same day. The amputee was provided two periods of at least 15 minutes on previous, non-consecutive days to familiarize himself with the experimental prosthesis.

## 6.5 Test Results

The video taken from the test is available and can be found via the link provided in [14]. The controller was tuned by trial and error based on the amputee's feedback and the guidelines previously described. The final parameters are provided

Table XI: Controller tuning parameters.

$K$ (N/mm)	$K_s$ (N/mm)	$B$ (Ns/mm)
200	0	-1.743
$b_h$ (Ns/mm)	$q_4^\circ$ (mm)	$q_{threshold}$ (mm)
2.5	0	2

in Tab. XI.  $K$ , the spring constant dominating the stance phase, was tuned before the trial so that the leg could hold the weight of one of the students in our lab. This gain was then fine-tuned with the test subject while he walked on a treadmill. The swing phase spring constant  $K_s$  and accordingly  $q_4^\circ$  were zero because the test subject's gait pattern caused the prosthesis to fully extend without aid.  $B$  was computed based on the constants  $a$  and  $R$  that were identified for the actuator.  $B_h$  overrides the negative damping during late swing phase, which is defined as  $q_{threshold} = 2$  mm of screw travel before full extension. Note that the same tuning was used for all tests and walking speeds.

Figure 48 shows the prosthetic knee angle as derived from the motor position for three walking speeds: slow (0.6 m/s), preferred (0.75 m/s), and fast (0.9 m/s). It can be seen that as walking speed increases the maximum angle of the knee in the swing phase also increases slightly, which is consistent with able-bodied gait [58]. However, the increase in maximum angle is less pronounced when comparing the preferred and fast speeds as opposed to the slow and preferred speeds, especially when considering the larger standard deviation band of the fast speed. This could be due to a singularity in the slider-crank mechanism of the knee actuator. The knee shows almost none of the flexion in the stance phase that is usually seen in able-bodied walking [117, 118]. This behavior, having little to no flexion in the stance phase, is typical, however, for most powered and passive prostheses [47, 62, 68, 88, 92, 97, 99]. While our controller had the ability to recover knee flexion in the stance phase, it

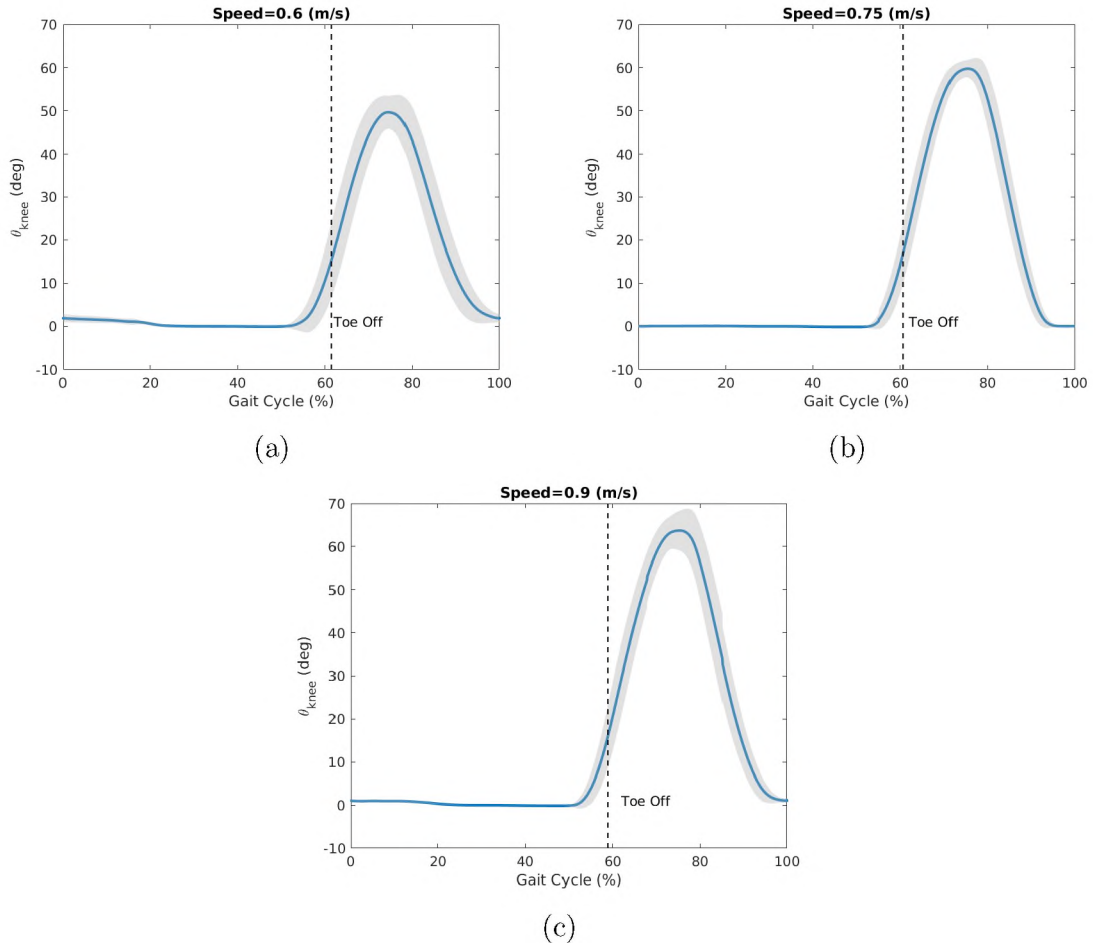


Figure 48: Average knee angle for three walking speeds. The slow, preferred, and fast walking speeds are 0.6, 0.75, and 0.9 meters per second, respectively. The gray bands show one standard deviation from the average trajectories.

was observed that the test subject would fully extend the knee joint before foot strike instead of using this feature, potentially due to previous walking habits and/or a lack of confidence in the prosthesis' ability to support the amputee's weight while flexed. The weight of the device might have also aided this outcome. A similar lack of stance flexion has been seen in below knee amputee gait data [86], suggesting the possibility that this phenomenon is due to the prosthetic ankle.

Figure 49 shows the electrical power flows for the three tested walking speeds. Power flows are given for the capacitor and motor side of the motor driver. Positive power indicates power consumption while negative power indicates power regenera-

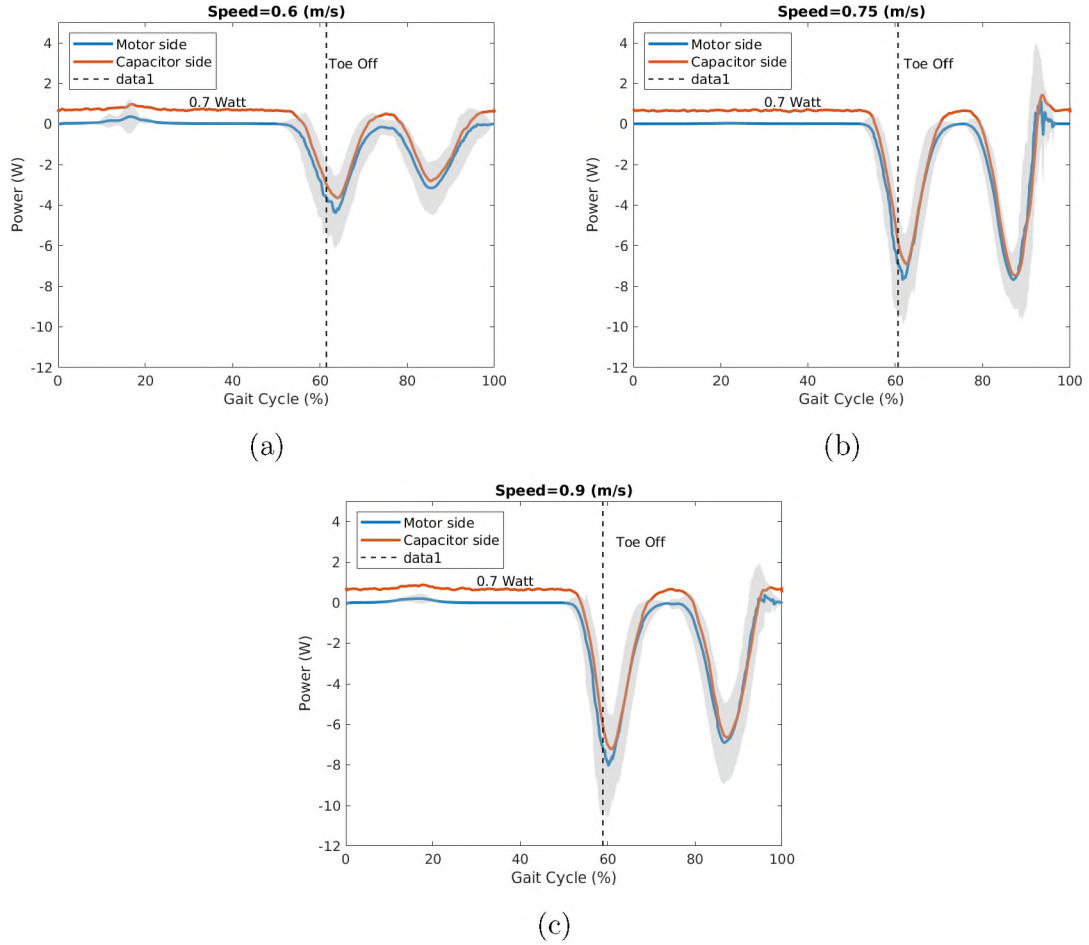


Figure 49: Power flows for the slow ( $0.6\text{ m/s}$ ), preferred ( $0.75\text{ m/s}$ ), and fast ( $0.9\text{ m/s}$ ) walking speeds. The gray bands show one standard deviation from the average trajectories. Positive power indicates power consumption. Negative power indicates power regeneration.

tion. In the stance phase, very little power is consumed. In able-bodied gait, the knee joint uses positive power while it is being extended during mid-stance [117]. As previously explained, for our tests the knee was fully extended during stance and supported the weight of the amputee without the need for energy expenditure. Hence the controller only needs to provide sufficient power to stabilize the knee. In the swing phase the negative damping term of Eq. (6.4) becomes dominant, and power is regenerated and stored in the ultracapacitor. With increased walking speed the peak value of the regenerated power increases. In addition, not all of the regenerated power is stored in the capacitor, and a portion of it (0.7 Watts) is consumed by the



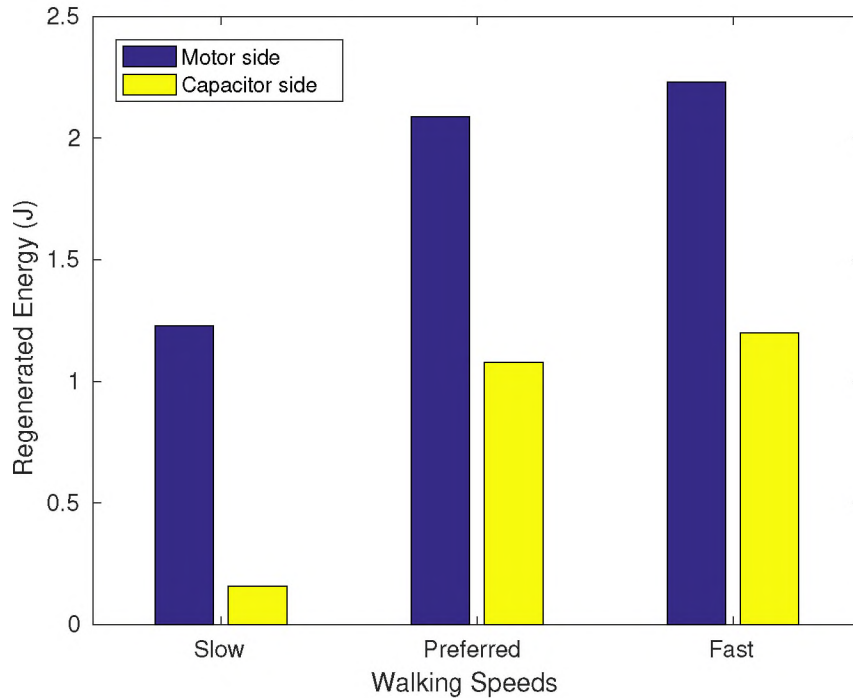


Figure 50: Average energy regenerated in each gait cycle for three walking speeds. Regenerated energies are reported for the capacitor side and the motor side of the motor driver.

motor driver.

As was observed from the power plots, energy regeneration was possible under the test conditions. Integrating the power measurements yields total energy regenerated. This is shown for both the motor and capacitor sides of the motor driver and across all speeds in Fig. 50. As speed increases, it is clear from the motor side values that energy regenerated increases. However, approximately one half or more of the regenerated energy does not reach the capacitor bank to be stored. Efficiency does increase significantly between the slow speed and both higher rates, suggesting that the efficiency of the motor driver is affected by the return voltage and/or current applied. There is a less significant increase between the preferred and fast walking speeds. This is likely partially due to the previously mentioned singularity in the crank-slider. It is also true that the hard stop prevention damping will use more energy at higher swing speeds, causing less energy to be available for storage. Comparing these results with

able-bodied data, in [117] the range of available energy is about 15-30 J for slow to fast paced walking, respectively. It therefore seems likely that there is still significant energy to be captured beyond what we have accomplished. Indeed, a regeneration potential is known to exist during the stance phase of able-bodied gait [117]. Our current results do not include energy recovery from this region.

## 6.6 Remarks

Within this work we have developed a powered knee prosthesis and controller, emphasizing control simplicity and energy regeneration. An experimental trial conducted with an amputee test subject validated the control method and achieved energy regeneration. Furthermore, basic features of able-bodied gait were replicated in testing, including swing phase knee flexion and transitions between gait phases.

Three traits of the proposed control law differentiate it from alternative methods. First, it has only five parameters, and they are intuitive for the individual adjusting the gains. This makes the tuning process relatively easy; tuning was able to be completed in a matter of minutes while conducting the test. Second, guidelines for tuning for energy regeneration can be developed analytically. Lastly, our approach only provides power to the knee joint when needed, yielding further energy savings.

The stability of the controller has not been evaluated analytically. This topic has been reserved for future work.

Considering longer periods of operation in the future, several items must be addressed. As with any system with finite on-board power storage, operation must be stopped once charge (indicated by  $V_{cap}$ ) drops below an acceptable threshold. At this point the system must be recharged. It is important to note that two alternative conditions, self-sustained operation or even charge buildup, can also occur in a system with energy regeneration. Achieving either of these conditions is dependent on system parameters and trajectories. If charging occurs during operation, the regenerated

power from the knee can be used for operating a powered ankle, which is a primary long-term goal of this work.

As suggested by the results, the prototype suffers from several sources of energy loss. Additionally, there are some losses that are not even reflected in the measurements taken. In the next hardware iteration, an improved actuator, including the motor, motor driver, and screw, will aid in eliminating these losses. Because the energy regenerated is directly dependent on the motor parameters, a more optimal motor can be selected with this in mind. A different four-quadrant motor driver should be identified to better transfer the power available for regeneration at low walking speeds. The current screw is a lead screw with a rated efficiency of about 60%. Replacing it with a ballscrew can easily raise this value above 90%. In addition, the energy regenerated by the negative damping is inversely proportional to electrical resistance ( $R$ ), Eq. (6.10). By embedding the electronics and eliminating the lengthy tether used in the test, further improvements in energy regeneration are possible.

## CHAPTER VII

### CONCLUSION

#### 7.1 Statement of Contributions

In this dissertation, we set out to investigate the possibilities and limitations of robots having energy regenerative drive systems. We aimed to explore the factors affecting energy regeneration, and to find bounds on the maximum energy regeneration attainable. To achieve this goal, five objectives were set at the beginning of this dissertation.

##### **Objective 1: Extend the baseline framework developed by Richter.**

In Chapter II, we expanded the framework in [81] to include the star configuration for the semi-active joints. In the star configuration, all the semi-active joints are connected to a common central capacitor, therefore allowing direct energy transfer from a joint with excess energy to a joint that requires energy. We showed that in terms of the total energy regenerated, the star and distributed configurations are equivalent; this was dictated by the SVC control strategy. However, the main advantage of the star configuration, over the distributed configuration is that it prevents the complete discharge, or overcharge of the capacitors, by channeling energy between semi-active robot joints. The star and distributed configurations are the two more relevant topologies investigated; other possible configurations for the semi-active joints

can be seen as the combination of the two. We also showed that by feeding back the capacitor voltage, SVC eliminates the need to model the ultracapacitor(s) for controlling the robot and formulating optimization problems. This is an important feature since ultracapacitors behave in a complex and nonlinear manner. In addition, we derive expressions for the amount of energy regenerated and the overall energy balance, which become the basis of all the optimization problems formulated in subsequent chapters. Moreover, the extended framework enables the generalization of all the results developed in this dissertation to any robotic system that can be captured using this framework.

**Objective 2: Investigate parameter optimization problems for energy regenerative robots.**

In Chapter III, we formulated and solved parameter optimization problems pertaining to robots with energy regeneration. Assuming the robot follows predefined motion trajectories, we found closed-form solutions for the optimal manipulator parameter vector that maximize energy regeneration in one or more semi-active joints. The optimal parameter vector can be used as a guideline when designing robotic systems that are capable of energy recovery. In addition, we show that the optimal solution is global and unique, and derive closed-form expressions for the maximum attainable energy regeneration. Moreover, we provide closed-form expressions for the optimal gear ratio and show that energy regeneration increases with the increase of the motor torque constant, and the decrease of motor winding resistance. The closed-form expressions we derive in this chapter provide insight into the capabilities and limitations of energy regeneration and become very valuable, considering that they are applicable to any energy regenerative robotic system that can be modeled using the framework of Chapter II.

### **Publications:**

- Khalaf, P., & Richter, H. (2018). On global, closed-form solutions to parametric optimization problems for robots with energy regeneration. *Journal of Dynamic Systems, Measurement, and Control*, 140(3), 031003.
- Khalaf, P., & Richter, H. (2016, July). Parametric optimization of stored energy in robots with regenerative drive systems. In *2016 IEEE International Conference on Advanced Intelligent Mechatronics (AIM)*, (pp. 1424-1429).

### **Objective 3: Investigate trajectory optimization problems for energy regenerative robots.**

In Chapter IV, assuming fixed system parameters, we solved several trajectory optimization problems, where closed-form solutions were possible. These problems included maximizing energy regeneration with respect to the external force/moment trajectory, and maximizing energy regeneration with respect to an arbitrary variable satisfying a set of conditions. All other system trajectories were assumed predefined and fixed. For each case, we give expressions for the maximum energy regeneration that are global and unique. These solutions provide understanding of the limits and bounds on energy regeneration, and can help in making various design decisions, such as choosing an appropriate capacitor size, or comparing the cost vs. benefits of incorporating energy regeneration in a given system. Moreover, we present the analytical solution to the linear optimal control problem, where assuming fixed system parameters, we find optimal control and motion trajectories that maximize energy regeneration for a linear time invariant system. Cartesian robots fall under this category and are utilized extensively in industrial production lines for high speed pick and place operations. The optimal linear control solution can easily be applied to any energy regenerative Cartesian robot that can be modeled using the aforementioned

framework. Most robotic systems, however, can not be accurately modeled using linear equations. Therefore, we formulate the nonlinear optimal control problem in this chapter. In the general case, analytical solutions for this problem cannot be found; hence, we provide the numerical formulation based on the direct collocation method and demonstrate the results using a PUMA 500 robot model.

**Publication:**

- Khalaf, P., & Richter, H. (2019). Trajectory Optimization of Robots with Regenerative Drive Systems: Numerical and Experimental Results. *IEEE Transactions on Robotics*. (under review)

**Objective 4: Experimentally evaluate energy regeneration in an industrial robotic manipulator.**

One of the goals we set out to achieve at the beginning was to provide experimental results that demonstrate the effectiveness of energy regeneration in robotic systems, which is lacking in the literature. Therefore, in Chapter V, we experimentally evaluated optimal point-to-point trajectories, maximizing energy regeneration for the PUMA 500 robot. To do so, we used an experimentally identified model to numerically solve the nonlinear optimal control problem via the direct collocation method. The optimal trajectories are enforced on the robot using robust passivity based control, and an experimental setup is devised to measure power flows at key locations. Three trajectories with different starting and ending points and movement durations were considered. The experimental power flows showed a good agreement with numerical results. In addition, motor driver inefficiency and friction were identified as the major sources of energy loss. We develop a new definition for the effectiveness of energy regeneration. The experimental results showed that energy regeneration was

effective in reducing the overall energy consumption by 10 – 22%. A more efficient robot design (lower friction, higher quality parts, etc.) can lead to further reductions energy consumption. Moreover, we investigated neighboring optimal trajectories and showed the strong dependency of energy regeneration on trajectories followed by the robot. In addition, we performed experiments to show the negative effect of controller chattering on motor driver regeneration efficiency.

**Publication:**

- Khalaf, P., & Richter, H. (2019). Trajectory Optimization of Robots with Regenerative Drive Systems: Numerical and Experimental Results. *IEEE Transactions on Robotics*. (under review)

**Objective 5: Design, control, and experimentally evaluate an energy regenerative powered transfemoral prosthesis.**

One of the main focuses of this dissertation was the applications of energy regenerations in lower limb powered prostheses. In Chapter VI, we presented the design and control of an energy regenerative powered transfemoral prosthesis. Our prototype included a regenerative knee joint and a passive ankle joint. We developed a novel varying impedance control method control method that emphasizes simplicity while explicitly dealing with energy regeneration. The controller has only five tuning parameters that are easily adjusted in a matter of minutes. The controller allows walking at different speeds with the prosthesis while regenerating energy to reduce energy consumption. The prosthesis prototype is evaluated with an amputee test subject walking on a treadmill. To our best knowledge, this is the first human trial testing of an electro-mechanical energy-regenerative prosthesis. The prototype did, however, suffer from several sources of inefficiency, which can be eliminated by design



revisions and using higher quality parts in future iterations. Therefore, in terms of energy regeneration, there is a lot of potential to be gained.

**Publication:**

- Khalaf, P., Warner, H., Hardin, E., Richter, H., & Simon, D. (2018, September). Development and Experimental Validation of an Energy Regenerative Prosthetic Knee Controller and Prototype. In ASME 2018 Dynamic Systems and Control Conference (pp. V001T07A008-V001T07A008). American Society of Mechanical Engineers.

## 7.2 Future Perspectives

Research in the area of energy regenerative robotics is relatively new and ongoing. With advances in energy storage technology and electric drive systems in the coming future, energy regeneration will find its way into more applications related to robotic systems. Here, we briefly mention some of the possible directions for future research.

In most of this dissertation, we have been concerned with motion tracking control methods, and only in Chapter VI we look into a specific case of impedance control for the powered prosthesis application. By controlling the dynamic interaction of the robot with its environment, impedance control can be used to emulate compliant behavior, which, as pointed out in Chapter VI, makes it the ideal control method for powered prostheses, exoskeletons, and in general, for controlling human robot interactions. Therefore, investigating impedance control methods applied to regenerative robotic systems for the purpose of finding the range of impedance parameters that result in energy regeneration, or possibly finding closed-form solutions for the optimal impedance parameters maximizing energy regeneration, is of particular value.

In this dissertation, we took a model based approach for formulating and solv-

ing optimizing problems pertaining to energy regenerative robots. In this approach, the optimization results depend heavily on the accuracy of the system model, requiring a lot of time and effort to be spent on model development. An alternative approach would be to use model-free online optimization methods, such as extremum seeking [1, 59]. For the powered prosthesis application coupled with impedance control, extremum seeking can be used to find the optimal impedance parameters that would result in maximum energy regeneration without the need to model the prosthesis or predict the behavior of the human subject.

We evaluated energy regeneration experimentally for two applications: the PUMA 500 industrial robotic manipulator, and the lower limb powered prosthesis prototype. In both cases, we used custom regenerative drives (four quadrant motor driver powered by an ultracapacitor) with existing hardware for evaluating the effectiveness of energy regeneration. On the other hand, in Chapter III, we showed that system parameters (gear ratios, link masses, etc.) have a great effect on energy regeneration, and how unsuitable parameter values, can lead to little or no regeneration. In order to truly evaluate the potential of energy regeneration in robotic systems, one needs to design the robot from the beginning with energy regeneration in mind. Therefore, every aspect of the robot, from selected gear ratios and electric motors, to the design of the control system and motion trajectories, are aimed towards maximizing energy regeneration.

An energy regenerative robot configured in the star configuration allows energy to flow directly between robot joints through the central capacitor. This concept could also be extended to multi-robot and collaborative robot systems, where energy can flow from a joint of one robot with an excess of energy to a joint of another robot requiring energy. These robots can be performing independent tasks or working together to achieve a common goal. Interesting optimization problems could be defined to find the trajectories for the robots that will result in maximum energy regeneration

while also completing the assigned task. Some of this research is currently underway at Cleveland State University.

## BIBLIOGRAPHY

- [1] K. B. Ariyur and M. Krstic. *Real-time optimization by extremum-seeking control*. John Wiley & Sons, 2003.
- [2] T. Asai and J. Scruggs. Nonlinear stochastic control of self-powered variable-damping vibration control systems. In *2016 American Control Conference (ACC)*, pages 442–448. IEEE, 2016.
- [3] S. K. Au and H. M. Herr. Powered ankle-foot prosthesis. *IEEE Robotics & Automation Magazine*, 15(3):52–59, 2008.
- [4] S. K. Au, J. Weber, and H. Herr. Powered ankle-foot prosthesis improves walking metabolic economy. *IEEE Transactions on Robotics*, 25(1):51–66, 2009.
- [5] R. D. Bellman, M. A. Holgate, and T. G. Sugar. SPARKy 3: Design of an active robotic ankle prosthesis with two actuated degrees of freedom using regenerative kinetics. In *2008 2nd IEEE RAS & EMBS International Conference on Biomedical Robotics and Biomechatronics*, pages 511–516. IEEE, 2008.
- [6] N. Bertrand, J. Sabatier, O. Briat, and J.-M. Vinassa. Fractional non-linear modelling of ultracapacitors. *Communications in Nonlinear Science and Numerical Simulation*, 15(5):1327–1337, 2010.
- [7] S. Buller, E. Karden, D. Kok, and R. De Doncker. Modeling the dynamic behavior of supercapacitors using impedance spectroscopy. In *Conference Record*

- of the 2001 IEEE Industry Applications Conference. 36th IAS Annual Meeting, volume 4, pages 2500–2504. IEEE, 2001.
- [8] G. Buondonno, J. Carpentier, G. Saurel, N. Mansard, A. De Luca, and J.-P. Laumond. Actuator design of compliant walkers via optimal control. In *IEEE/RSJ International Conference on Intelligent Robots and Systems (IROS 2017)*, page 7p, 2017.
- [9] A. Burke. Ultracapacitors: why, how, and where is the technology. *Journal of Power Sources*, 91(1):37–50, 2000.
- [10] G. Carabin, E. Wehrle, and R. Vidoni. A review on energy-saving optimization methods for robotic and automatic systems. *Robotics*, 6(39), 2017.
- [11] P. Cherelle, V. Grosu, A. Matthys, B. Vanderborght, and D. Lefeber. Design and validation of the ankle mimicking prosthetic (amp-) foot 2.0. *IEEE Transactions on Neural Systems and Rehabilitation Engineering*, 22(1):138–148, 2014.
- [12] P. Cherelle, A. Matthys, V. Grosu, B. Vanderborght, and D. Lefeber. The amp-foot 2.0: Mimicking intact ankle behavior with a powered transtibial prosthesis. In *2012 4th IEEE RAS & EMBS International Conference on Biomedical Robotics and Biomechatronics (BioRob)*, pages 544–549. IEEE, 2012.
- [13] C. J. Chiang, J. L. Yang, and W. C. Cheng. Dynamic modeling of the electrical and thermal behavior of ultracapacitors. In *10th IEEE International Conference on Control and Automation (ICCA)*, pages 1839–1844. IEEE, 2013.
- [14] Control, Robotics and Mechatronics lab. Code for energy regeneration optimization. <https://github.com/csurowing/regenrobotics/blob/master/DCoptPuma>, 2018. accessed 11-December-2018.

- [15] Control, Robotics and Mechatronics lab. Video of puma robot following optimized trajectories for each studied case. <https://www.youtube.com/channel/UCE0uudaRqwM3KQjxIa1QFvQ>, 2018. accessed 11-December-2018.
- [16] B. E. Conway. *Electrochemical supercapacitors: scientific fundamentals and technological applications*. Springer Science & Business Media, 2013.
- [17] P. I. Corke and B. Armstrong-Helouvry. A search for consensus among model parameters reported for the PUMA 560 robot. In *IEEE International Conference on Robotics and Automation*, pages 1608–1613. IEEE, 1994.
- [18] H. De Las Casas, H. Richter, and A. J. van den Bogert. Design and hybrid impedance control of a powered rowing machine. In *ASME 2017 Dynamic Systems and Control Conference*, pages V001T38A002–V001T38A002. American Society of Mechanical Engineers, 2017.
- [19] R. Dedić and H. Dindo. Smartleg: An intelligent active robotic prosthesis for lower-limb amputees. In *Information, Communication and Automation Technologies (ICAT), 2011 XXIII International Symposium on*, pages 1–7. IEEE, 2011.
- [20] E. G. dos Santos and H. Richter. Modeling and control of a novel variable-stiffness regenerative actuator. In *ASME 2018 Dynamic Systems and Control Conference*, pages V002T24A003–V002T24A003. American Society of Mechanical Engineers, 2018.
- [21] M. F. Eilenberg, H. Geyer, and H. Herr. Control of a powered ankle-foot prosthesis based on a neuromuscular model. *IEEE Transactions on Neural Systems and Rehabilitation Engineering*, 18(2):164–173, 2010.
- [22] C. Everarts, B. Dehez, and R. Ronsse. Variable stiffness actuator applied to an active ankle prosthesis: Principle, energy-efficiency, and control. In *2012*

- IEEE/RSJ International Conference on Intelligent Robots and Systems*, pages 323–328. IEEE, 2012.
- [23] N. P. Fey, A. M. Simon, A. J. Young, and L. J. Hargrove. Knee swing-initiation and ankle plantar flexion control using an active prosthesis across walking speeds and users. In *Annual meeting of the American Society of Biomechanics. Omaha, NE*, 2013.
- [24] Y. Fujimoto. Minimum energy biped running gait and development of energy regeneration leg. In *Advanced Motion Control, 2004. AMC'04. The 8th IEEE International Workshop on*, pages 415–420. IEEE, 2004.
- [25] S. Gale, A. A. Eijsen, and J. T. Gravdahl. Modelling and simulation of a flywheel based energy storage system for an industrial manipulator. In *2015 IEEE International Conference on Industrial Technology (ICIT)*, pages 332–337. IEEE, 2015.
- [26] Y. Gao, L. Chen, and M. Ehsani. Investigation of the effectiveness of regenerative braking for ev and hev. *SAE transactions*, pages 3184–3190, 1999.
- [27] A. Ghorbanpour and H. Richter. Control with optimal energy regeneration in robot manipulators driven by brushless dc motors. In *ASME 2018 Dynamic Systems and Control Conference*, pages V001T04A003–V001T04A003. American Society of Mechanical Engineers, 2018.
- [28] P. J. Grbovic. *Ultra-capacitors in power conversion systems: analysis, modeling and design in theory and practice*. John Wiley & Sons, 2013.
- [29] P. J. Grbovic, P. Delarue, P. Le Moigne, and P. Bartholomeus. Modeling and control of the ultracapacitor-based regenerative controlled electric drives. *IEEE Transactions on Industrial Electronics*, 58(8):3471–3484, 2011.

- [30] P. J. Grbovic, P. Delarue, P. Le Moigne, and P. Bartholomeus. The ultracapacitor-based controlled electric drives with braking and ride-through capability: Overview and analysis. *IEEE Transactions on Industrial Electronics*, 58(3):925–936, 2011.
- [31] S. Ha, S. Coros, A. Alspach, J. Kim, and K. Yamane. Joint optimization of robot design and motion parameters using the implicit function theorem. In *Robotics: Science and Systems*, 2017.
- [32] M. S. Halper and J. C. Ellenbogen. Supercapacitors: A brief overview. *The MITRE Corporation, McLean, Virginia, USA*, pages 1–34, 2006.
- [33] C. Hansen, J. Öltjen, D. Meike, and T. Ortmaier. Enhanced approach for energy-efficient trajectory generation of industrial robots. In *Automation Science and Engineering (CASE), 2012 IEEE International Conference on*, pages 1–7. IEEE, 2012.
- [34] M. Hazewinkel. *Encyclopaedia of Mathematics: Fibonacci Method H*. Springer Science & Business Media, 2013.
- [35] H. M. Herr and A. M. Grabowski. Bionic ankle-foot prosthesis normalizes walking gait for persons with leg amputation. *Proceedings of the Royal Society B: Biological Sciences*, 279(1728):457–464, 2011.
- [36] M. J. Highsmith, J. T. Kahle, S. L. Carey, D. J. Lura, R. V. Dubey, K. R. Csavina, and W. S. Quillen. Kinetic asymmetry in transfemoral amputees while performing sit to stand and stand to sit movements. *Gait & posture*, 34(1):86–91, 2011.
- [37] M. J. Highsmith, J. T. Kahle, S. L. Carey, D. J. Lura, R. V. Dubey, and W. S. Quillen. Kinetic differences using a power knee and c-leg while sitting down



- and standing up: a case report. *JPO: Journal of Prosthetics and Orthotics*, 22(4):237–243, 2010.
- [38] J. Hitt, T. Sugar, M. Holgate, R. Bellman, and K. Hollander. Robotic transtibial prosthesis with biomechanical energy regeneration. *Industrial Robot: An International Journal*, 36(5):441–447, 2009.
- [39] J. K. Hitt, R. Bellman, M. Holgate, T. G. Sugar, and K. W. Hollander. The SPARKy (spring ankle with regenerative kinetics) project: Design and analysis of a robotic transtibial prosthesis with regenerative kinetics. In *ASME 2007 International Design Engineering Technical Conferences and Computers and Information in Engineering Conference*, pages 1587–1596. American Society of Mechanical Engineers, 2007.
- [40] J. K. Hitt, T. G. Sugar, M. Holgate, and R. Bellman. An active foot-ankle prosthesis with biomechanical energy regeneration. *Journal of medical devices*, 4(1):011003, 2010.
- [41] M. A. Holgate, A. W. Bohler, and T. G. Suga. Control algorithms for ankle robots: A reflection on the state-of-the-art and presentation of two novel algorithms. In *2008 2nd IEEE RAS & EMBS International Conference on Biomedical Robotics and Biomechatronics*, pages 97–102. IEEE, 2008.
- [42] M. A. Holgate, J. K. Hitt, R. D. Bellman, T. G. Sugar, and K. W. Hollander. The SPARKy (spring ankle with regenerative kinetics) project: Choosing a dc motor based actuation method. In *2008 2nd IEEE RAS & EMBS International Conference on Biomedical Robotics and Biomechatronics*, pages 163–168. IEEE, 2008.
- [43] B. L. Hunter. *Design of a self-contained, active, regenerative computer con-*

- trolled above-knee prosthesis*. PhD thesis, Massachusetts Institute of Technology, 1981.
- [44] K. A. Ingraham, N. P. Fey, A. M. Simon, and L. J. Hargrove. Assessing the relative contributions of active ankle and knee assistance to the walking mechanics of transfemoral amputees using a powered prosthesis. *PLOS ONE*, 11(1):e0147661, 2016.
- [45] T. Izumi. Energy saving manipulator by regenerating conservative energy. In *6th International Workshop on Advanced Motion Control*, pages 630–635. IEEE, 2000.
- [46] T. Izumi, P. Boyagoda, M. Nakaoka, and E. Hiraki. Optimal control of a servo system regenerating conservative energy to a condenser. In *Industrial Automation and Control: Emerging Technologies, 1995., International IEEE/IAS Conference on*, pages 651–656. IEEE, 1995.
- [47] J. L. Johansson, D. M. Sherrill, P. O. Riley, P. Bonato, and H. Herr. A clinical comparison of variable-damping and mechanically passive prosthetic knee devices. *American Journal of Physical Medicine & Rehabilitation*, 84(8):563–575, 2005.
- [48] A. S. Kammer and N. Olgac. Enhancing energy harvesting capacity using delayed feedback control. In *2016 American Control Conference (ACC)*, pages 1863–1868. IEEE, 2016.
- [49] S. Kannappan, K. Kaliyappan, R. K. Manian, A. S. Pandian, H. Yang, Y. S. Lee, J.-H. Jang, and W. Lu. Graphene based supercapacitors with improved specific capacitance and fast charging time at high current density. *arXiv preprint arXiv:1311.1548*, 2013.

- [50] D. C. Karnopp, D. L. Margolis, and R. C. Rosenberg. *System Dynamics: Modeling, Simulation, and Control of Mechatronic Systems*. John Wiley & Sons, 2012.
- [51] H. Kawasaki, T. Shimizu, and K. Kanzaki. Symbolic analysis of the base parameters for closed-chain robots based on the completion procedure. In *1996 IEEE International Conference on Robotics and Automation*, volume 2, pages 1781–1786. IEEE, 1996.
- [52] P. Khalaf and H. Richter. Parametric optimization of stored energy in robots with regenerative drive systems. In *2016 IEEE International Conference on Advanced Intelligent Mechatronics (AIM)*, pages 1424–1429. IEEE, 2016.
- [53] P. Khalaf and H. Richter. On global, closed-form solutions to parametric optimization problems for robots with energy regeneration. *Journal of Dynamic Systems, Measurement, and Control*, 140(3):031003, 2018.
- [54] P. Khalaf, H. Warner, E. Hardin, H. Richter, and D. Simon. Development and experimental validation of an energy regenerative prosthetic knee controller and prototype. In *ASME 2018 Dynamic Systems and Control Conference*, pages V001T07A008–V001T07A008. American Society of Mechanical Engineers, 2018.
- [55] A. Khaligh and Z. Li. Battery, ultracapacitor, fuel cell, and hybrid energy storage systems for electric, hybrid electric, fuel cell, and plug-in hybrid electric vehicles: State of the art. *IEEE Transactions on Vehicular Technology*, 59(6):2806–2814, 2010.
- [56] F. Khoshnoud, Y. Zhang, R. Shimura, A. Shahba, G. Jin, G. Pissanidis, Y. K. Chen, and C. W. De Silva. Energy regeneration from suspension dynamic

- modes and self-powered actuation. *IEEE/ASME Transactions on Mechatronics*, 20(5):2513–2524, 2015.
- [57] D. E. Kirk. *Optimal control theory: an introduction*. Courier Corporation, 2012.
- [58] C. Kirtley, M. W. Whittle, and R. Jefferson. Influence of walking speed on gait parameters. *Journal of Biomedical Engineering*, 7(4):282–288, 1985.
- [59] S. Kumar, A. Mohammadi, N. Gans, and R. D. Gregg. Automatic tuning of virtual constraint-based control algorithms for powered knee-ankle prostheses. In *2017 IEEE Conference on Control Technology and Applications (CCTA)*, pages 812–818. IEEE, 2017.
- [60] T.-S. Kwon, S.-W. Lee, S.-K. Sul, C.-G. Park, N.-I. Kim, B.-i. Kang, and M.-s. Hong. Power control algorithm for hybrid excavator with supercapacitor. *IEEE Transactions on Industry Applications*, 46(4):1447–1455, 2010.
- [61] B. E. Lawson, J. Mitchell, D. Truex, A. Shultz, E. Ledoux, and M. Goldfarb. A robotic leg prosthesis: Design, control, and implementation. *IEEE Robotics & Automation Magazine*, 21(4):70–81, 2014.
- [62] B. E. Lawson, B. Ruhe, A. Shultz, and M. Goldfarb. A powered prosthetic intervention for bilateral transfemoral amputees. *IEEE Transactions on Biomedical Engineering*, 62(4):1042–1050, 2015.
- [63] B. E. Lawson, H. A. Varol, A. Huff, E. Erdemir, and M. Goldfarb. Control of stair ascent and descent with a powered transfemoral prosthesis. *IEEE Transactions on Neural Systems and Rehabilitation Engineering*, 21(3):466–473, 2013.
- [64] E. D. Ledoux, B. E. Lawson, A. H. Shultz, H. L. Bartlett, and M. Goldfarb. Metabolics of stair ascent with a powered transfemoral prosthesis. In *2015*

*37th Annual International Conference of the IEEE Engineering in Medicine and Biology Society (EMBC)*, pages 5307–5310. IEEE, 2015.

- [65] F. Lewis, D. Dawson, and C. Abdallah. *Robot Manipulator Control: Theory and Practice*. Automation and Control Engineering. Taylor & Francis, 2003.
- [66] S. M. Lukic, S. G. Wirasingha, F. Rodriguez, J. Cao, and A. Emadi. Power management of an ultracapacitor/battery hybrid energy storage system in an hev. In *2006 IEEE Vehicle Power and Propulsion Conference*, pages 1–6. IEEE, 2006.
- [67] C. Makkar, W. Dixon, W. Sawyer, and G. Hu. A new continuously differentiable friction model for control systems design. In *Proceedings of the 2005 IEEE/ASME International Conference on Advanced Intelligent Mechatronics.*, pages 600–605. IEEE, 2005.
- [68] E. C. Martinez-Villalpando and H. Herr. Agonist-antagonist active knee prosthesis: A preliminary study in level-ground walking. *Journal of Rehabilitation Research and Development*, 46(3):361, 2009.
- [69] E. C. Martinez-Villalpando, J. Weber, G. Elliott, and H. Herr. Design of an agonist-antagonist active knee prosthesis. In *2008 2nd IEEE RAS & EMBS International Conference on Biomedical Robotics and Biomechatronics*, pages 529–534. IEEE, 2008.
- [70] Maxwell Technologies. *Maxwell Ultracapacitors*. Maxwell Technologies, San Diego, CA, 2016. See also URL [maxwell.com](http://maxwell.com).
- [71] A. H. Memar and E. T. Esfahani. Modeling and dynamic parameter identification of the schunk powerball robotic arm. In *ASME 2015 International Design Engineering Technical Conferences and Computers and Information in Engi-*

- neering Conference*, volume 5C: 39th Mechanisms and Robotics Conference, page V05CT08A024. American Society of Mechanical Engineers, 2015.
- [72] N. Molen. Energy/speed relation of below-knee amputees walking on a motor-driven treadmill. *Internationale Zeitschrift für angewandte Physiologie einschließlich Arbeitsphysiologie*, 31(3):173–185, 1973.
- [73] M. A. Müller and F. Allgöwer. Economic and distributed model predictive control: Recent developments in optimization-based control. *SICE Journal of Control, Measurement, and System Integration*, 10(2):39–52, 2017.
- [74] V. Musolino, L. Piegari, and E. Tironi. New full-frequency-range supercapacitor model with easy identification procedure. *IEEE Transactions on Industrial Electronics*, 60(1):112–120, 2013.
- [75] Y. Nakamura and S. Ito. Lowering energy consumption of space robot systems through kinetic energy conservation. In *Robotics and Automation, 1993. Proceedings., 1993 IEEE International Conference on*, pages 1019–1026. IEEE, 1993.
- [76] N. Nakazawa, Y. Kono, E. Takao, and N. Takeda. Development of a braking energy regeneration system for city buses. Technical report, SAE Technical Paper, 1987.
- [77] M. Ogasa. Energy saving and environmental measures in railway technologies: Example with hybrid electric railway vehicles. *IEEE Transactions on Electrical and Electronic Engineering*, 3(1):15–20, 2008.
- [78] Ossur. *Power Knee instructions for use*. Ossur, Reykjavik, Iceland, latest edition, 2019. See also URL <https://assets.ossur.com/library/22244/POWER>.

- [79] Ottobock. *Empower Specification Sheet*. Ottobock, Duderstadt, Germany, latest edition, 2017. See also URL <https://professionals.ottobockus.com/media/pdf/14589-Empower-Spec-Sheet.pdf>.
- [80] R. Rarick, H. Richter, A. van den Bogert, D. Simon, H. Warner, and T. Barto. Optimal design of a transfemoral prosthesis with energy storage and regeneration. In *2014 American Control Conference*, pages 4108–4113. IEEE, 2014.
- [81] H. Richter. A framework for control of robots with energy regeneration. *Journal of Dynamic Systems, Measurement, and Control*, 137(9):091004, 2015.
- [82] H. Richter, X. Hui, A. J. van den Bogert, and D. Simon. Semiactive virtual control of a hydraulic prosthetic knee. In *2016 IEEE Conference on Control Applications (CCA)*, pages 422–429. IEEE, 2016.
- [83] H. Richter, D. Simon, and A. van den Bogert. Semiactive virtual control method for robots with regenerative energy-storing joints. In *Proc. 19th IFAC World Congress, Cape Town, South Africa, 2014*.
- [84] F. Rohani, H. Richter, and A. J. van den Bogert. Optimal design and control of an electromechanical transfemoral prosthesis with energy regeneration. *PloS one*, 12(11):e0188266, 2017.
- [85] A. Rufer and P. Barrade. A supercapacitor-based energy-storage system for elevators with soft commutated interface. *IEEE Transactions on industry applications*, 38(5):1151–1159, 2002.
- [86] D. J. Sanderson and P. E. Martin. Lower extremity kinematic and kinetic adaptations in unilateral below-knee amputees during walking. *Gait & Posture*, 6(2):126–136, 1997.

- [87] A. Schneuwly and R. Gally. Properties and applications of supercapacitors: From the state-of-the-art to future trends. *Rossens, Switzerland*, 2000.
- [88] A. D. Segal, M. S. Orendurff, G. K. Klute, M. L. McDowell, et al. Kinematic and kinetic comparisons of transfemoral amputee gait using C-Leg® and Mauch SNS® prosthetic knees. *Journal of Rehabilitation Research and Development*, 43(7):857, 2006.
- [89] S. Seok, A. Wang, M. Y. M. Chuah, D. J. Hyun, J. Lee, D. M. Otten, J. H. Lang, and S. Kim. Design principles for energy-efficient legged locomotion and implementation on the MIT Cheetah Robot. *IEEE/ASME Transactions on Mechatronics*, 20(3):1117–1129, 2015.
- [90] B. Seth. *Energy regeneration and its application to active above-knee prostheses*. PhD thesis, Massachusetts Institute of Technology, 1987.
- [91] T. Shimizu and C. Underwood. Super-capacitor energy storage for micro-satellites: Feasibility and potential mission applications. *Acta Astronautica*, 85:138–154, 2013.
- [92] A. H. Shultz, B. E. Lawson, and M. Goldfarb. Running with a powered knee and ankle prosthesis. *IEEE Transactions on Neural Systems and Rehabilitation Engineering*, 23(3):403–412, 2015.
- [93] A. M. Simon, K. A. Ingraham, N. P. Fey, S. B. Finucane, R. D. Lipschutz, A. J. Young, and L. J. Hargrove. Configuring a powered knee and ankle prosthesis for transfemoral amputees within five specific ambulation modes. *PLOS ONE*, 9(6):e99387, 2014.
- [94] S. Skogestad and I. Postlethwaite. *Multivariable feedback control: analysis and design*, volume 2. Wiley New York, 2007.



- [95] Z. Song, H. Hofmann, J. Li, J. Hou, X. Han, and M. Ouyang. Energy management strategies comparison for electric vehicles with hybrid energy storage system. *Applied Energy*, 134:321–331, 2014.
- [96] M. Spong, S. Hutchinson, and M. Vidyasagar. *Robot Modeling and Control*. Wiley, 2006.
- [97] F. Sup, A. Bohara, and M. Goldfarb. Design and control of a powered transfemoral prosthesis. *International Journal of Robotics Research*, 27(2):263–273, 2008.
- [98] F. Sup, H. A. Varol, and M. Goldfarb. Upslope walking with a powered knee and ankle prosthesis: initial results with an amputee subject. *IEEE Transactions on Neural Systems and Rehabilitation Engineering*, 19(1):71–78, 2011.
- [99] F. Sup, H. A. Varol, J. Mitchell, T. Withrow, and M. Goldfarb. Design and control of an active electrical knee and ankle prosthesis. In *2008 2nd IEEE RAS & EMBS International Conference on Biomedical Robotics and Biomechanics*, pages 523–528. IEEE, 2008.
- [100] F. Sup, H. A. Varol, J. Mitchell, T. J. Withrow, and M. Goldfarb. Preliminary evaluations of a self-contained anthropomorphic transfemoral prosthesis. *IEEE/ASME Transactions on Mechatronics*, 14(6):667–676, 2009.
- [101] K. A. Tabor. *The real-time digital control of a regenerative above-knee prosthesis*. PhD thesis, Massachusetts Institute of Technology, 1988.
- [102] S. Thiede. *Energy efficiency in manufacturing systems*. Springer Science & Business Media, 2012.
- [103] M. R. Tucker and K. B. Fite. Mechanical damping with electrical regenera-

- tion for a powered transfemoral prosthesis. In *2010 IEEE/ASME International Conference on Advanced Intelligent Mechatronics*, pages 13–18. IEEE, 2010.
- [104] M. R. Tucker, J. Olivier, A. Pagel, H. Bleuler, M. Bouri, O. Lambercy, J. del R Millán, R. Riener, H. Vallery, and R. Gassert. Control strategies for active lower extremity prosthetics and orthotics: a review. *Journal of NeuroEngineering and Rehabilitation*, 12(1):1, 2015.
- [105] A. J. van den Bogert, D. Blana, and D. Heinrich. Implicit methods for efficient musculoskeletal simulation and optimal control. *Procedia IUTAM*, 2:297–316, 2011.
- [106] R. Versluys, A. Desomer, G. Lenaerts, O. Pareit, B. Vanderborght, G. Perre, L. Peeraer, and D. Lefeber. A biomechatronical transtibial prosthesis powered by pleated pneumatic artificial muscles. *International Journal of Modelling, Identification and Control*, 4(4):394–405, 2008.
- [107] E. Vinot and R. Trigui. Optimal energy management of hevs with hybrid storage system. *Energy Conversion and Management*, 76:437–452, 2013.
- [108] O. von Stryk. Numerical solution of optimal control problems by direct collocation. *Optimal Control: Calculus of Variations, Optimal Control Theory and Numerical Methods*, 111:129, 2013.
- [109] A. Wächter and L. T. Biegler. On the implementation of an interior-point filter line-search algorithm for large-scale nonlinear programming. *Mathematical programming*, 106(1):25–57, 2006.
- [110] H. Warner, D. Simon, H. Mohammadi, and H. Richter. Switched robust tracking/impedance control for an active transfemoral prosthesis. In *2016 American Control Conference (ACC)*, pages 2187–2192. IEEE, 2016.

- [111] H. Warner, D. Simon, and H. Richter. Design optimization and control of a crank-slider actuator for a lower-limb prosthesis with energy regeneration. In *IEEE International Conference on Advanced Intelligent Mechatronics, Banff, Canada*, 2016.
- [112] H. E. Warner. Optimal design and control of a lower-limb prosthesis with energy regeneration. Master’s thesis, Cleveland State University, 2015.
- [113] R. Waters, J. Perry, D. Antonelli, and H. Hislop. Energy cost of walking of amputees: the influence of level of amputation. *J Bone Joint Surg Am*, 58(1):42–46, 1976.
- [114] G. Waycaster, S.-K. Wu, and X. Shen. A pneumatic artificial muscle actuated above-knee prosthesis. In *ASME 2010 Dynamic Systems and Control Conference*, pages 793–800. American Society of Mechanical Engineers, 2010.
- [115] T. Wilmot, G. Thomas, B. Montavon, R. Rarick, A. J. van den Bogert, S. Szatmary, D. J. Simon, W. Smith, and S. Samorezov. Biogeography-based optimization for hydraulic prosthetic knee control. 2013.
- [116] M. Windrich, M. Grimmer, O. Christ, S. Rinderknecht, and P. Beckerle. Active lower limb prosthetics: a systematic review of design issues and solutions. *Biomedical Engineering Online*, 15(3):140, 2016.
- [117] D. A. Winter. Energy generation and absorption at the ankle and knee during fast, natural, and slow cadences. *Clinical Orthopaedics and Related Research*, 175:147–154, 1983.
- [118] D. A. Winter. *Biomechanics and motor control of human movement*. John Wiley & Sons, 2009.

- [119] E. J. Wolf, V. Q. Everding, A. A. Linberg, J. M. Czerniecki, and C. J. M. Gabel. Comparison of the Power Knee and C-Leg during step-up and sit-to-stand tasks. *Gait & Posture*, 38(3):397–402, 2013.
- [120] W. Xi, Y. Yesilevskiy, and C. D. Remy. Selecting gaits for economical locomotion of legged robots. *International Journal of Robotics Research*, 35(9):1140–1154, 2016.
- [121] J. Xu, J. Yang, and J. Gao. An integrated kinetic energy recovery system for peak power transfer in 3-dof mobile crane robot. In *2011 IEEE/SICE International Symposium on System Integration (SII)*, pages 330–335. IEEE, 2011.
- [122] H. Yang, W. Sun, and B. Xu. New investigation in energy regeneration of hydraulic elevators. *IEEE/ASME Transactions on Mechatronics*, 12(5):519–526, 2007.
- [123] M. J. Yang, H. L. Jhou, B. Y. Ma, and K. K. Shyu. A cost-effective method of electric brake with energy regeneration for electric vehicles. *IEEE Transactions on Industrial Electronics*, 56(6):2203–2212, 2009.
- [124] Y. Zhang, K. Huang, F. Yu, Y. Gu, and D. Li. Experimental verification of energy-regenerative feasibility for an automotive electrical suspension system. In *2007 IEEE International Conference on Vehicular Electronics and Safety*, pages 1–5. IEEE, 2007.
- [125] Z. Zhang, X. Zhang, W. Chen, Y. Rasim, W. Salman, H. Pan, Y. Yuan, and C. Wang. A high-efficiency energy regenerative shock absorber using supercapacitors for renewable energy applications in range extended electric vehicle. *Applied Energy*, 178:177–188, 2016.

# APPENDICES

## APPENDIX A

### EQUATION DERIVATION

#### Interfacing Torque/Force for Semi-Active Joints

Bond graphs are used to model semi-active joints in the star and distributed configurations (Fig. 51). In this section, we present the detailed derivation of Eq. (2.2). The effort and flow variables for each bond are denoted by  $e_i$  and  $f_i$  respectively. The interfacing torque for the  $j$ -th semi-active joints can be written as

$$-\tau_j = n_j e_1 = n_j(e_2 + e_3 + e_4) \tag{A.1}$$

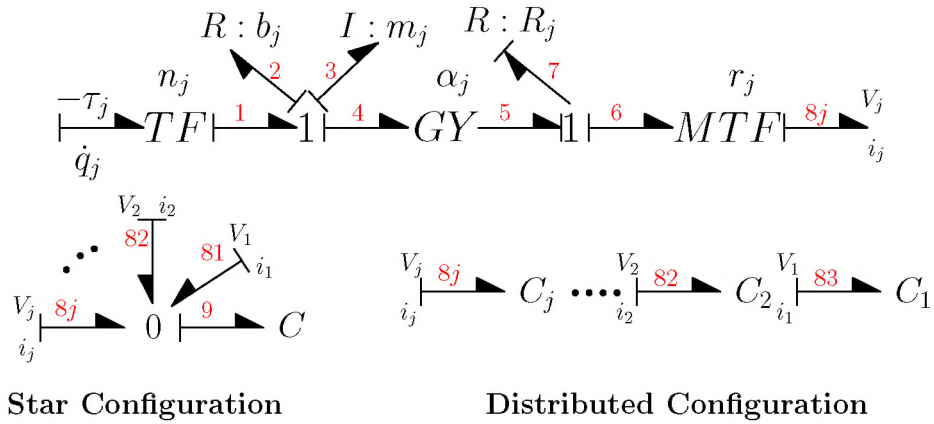


Figure 51: Bond graph of electro-mechanical semi-active joint in the distributed and star configurations.

where  $e_2 = b_j f_2$ ,  $e_3 = n_j m_j d(\dot{q}_j)/dt$ , and  $e_4 = \alpha_j f_5$ . Substituting gives

$$-\tau_j = n_j(b_j f_2 + n_j m_j \frac{d(\dot{q}_j)}{dt} + \alpha_j f_5) \quad (\text{A.2})$$

$f_2 = n_j \dot{q}_j$  and

$$f_5 = f_7 = \frac{e_7}{R_j} = \frac{1}{R_j}(e_5 - e_6) \quad (\text{A.3})$$

where

$$e_5 = \alpha_j f_4 = \alpha_j f_1 = \alpha_j n_j \dot{q}_j \quad (\text{A.4})$$

and

$$e_6 = r_j e_8 = r_j V_{cap} \quad (\text{A.5})$$

Replacing  $e_5$  and  $e_6$  in Eq. (A.3), we have

$$f_5 = \frac{1}{R_j}(\alpha_j n_j \dot{q}_j - r_j V_{cap}) \quad (\text{A.6})$$

and replacing for  $f_5$  in Eq. (A.2), we have

$$\tau_j = -m_j n_j^2 \ddot{q}_j - (bn^2 + \frac{a_j^2}{R})\dot{q}_j + \frac{a_j r_j}{R} V_{cap} \quad (\text{A.7})$$

where  $a = \alpha n$ .

## Energy Balance Equations

This section provides detailed derivations of Eq. (2.12), Eq. (2.13), and Eq. (2.14).

We start by deriving the expression of the Joule losses in terms of the desired control ( $\tau_j^d$ ). From the bond graph of Fig. 51 we have

$$P_{R_j} = R_j f_7^2 = R_j f_5^2 \quad (\text{A.8})$$

Replacing for  $f_5$  from Eq. (A.6) gives

$$P_{Rj} = \frac{(a_j \dot{q}_j - r_j V_{cap})^2}{R_j} \quad (\text{A.9})$$

By expanding this equation and using Eq. (2.6) we get

$$P_{Rj} = \frac{a_j^2 \dot{q}_j^2}{R_j} - 2\tau_j^d \dot{q}_j + \frac{R_j (\tau_j^d)^2}{a_j^2} \quad (\text{A.10})$$

Equation (2.2) expresses the relation between  $\tau_j$  and  $\tau_j^d$ . Multiplying both sides of this equation by  $\dot{q}_j$  yields

$$\tau_j \dot{q}_j = -m_j n_j^2 \ddot{q}_j \dot{q}_j - (b_j n_j^2 + \frac{a_j^2}{R_j}) \dot{q}_j^2 + \tau_j^d \dot{q}_j \quad (\text{A.11})$$

The kinetic energy of the actuator is expressed as  $K_j = \frac{1}{2} m_j (n_j \dot{q}_j)^2$ . The above equation can be simplified as

$$\tau_j \dot{q}_j = -\frac{dK_j}{dt} - (b_j n_j^2 + \frac{a_j^2}{R_j}) \dot{q}_j^2 + \tau_j^d \dot{q}_j \quad (\text{A.12})$$

Replacing  $\frac{a_j^2}{R_j} \dot{q}_j^2$  from Eq. (A.10) and rearranging the result gives

$$\tau_j^d \dot{q}_j - \frac{R_j (\tau_j^d)^2}{a_j^2} = -\tau_j \dot{q}_j - \frac{dK_j}{dt} - P_{Rj} - b_j n_j^2 \dot{q}_j^2 \quad (\text{A.13})$$

Taking the integral from  $t_1$  to  $t_2$  of both sides of this equation, Eq. (2.12) is obtained as

$$\Delta E_{sj} = \int_{t_1}^{t_2} \left( \tau_j^d \dot{q}_j - \frac{R_j (\tau_j^d)^2}{a_j^2} \right) dt = \int_{t_1}^{t_2} \left( -\tau_j \dot{q}_j - \frac{dK_j}{dt} - P_{Rj} - b_j n_j^2 \dot{q}_j^2 \right) dt \quad (\text{A.14})$$



Equation (2.13) is obtained by taking the sum of the above equation over all semi-active joints.

To derive Eq. (2.14), we start by writing the overall energy balance for the robotic manipulator:

$$\int_{t_1}^{t_2} \sum_{j=1}^e \tau_j \dot{q}_j dt + \int_{t_1}^{t_2} \sum_{j=e+1}^n \tau_j \dot{q}_j dt - \int_{t_1}^{t_2} \sum_{j=1}^n \mathcal{T}_j \dot{q}_j dt = \Delta E_m^\circ + \Sigma_m^\circ \quad (\text{A.15})$$

where the first term on the left hand side is the work done by the semi-active joints, the second term is the work done by the fully active joints ( $W_{act}$ ), and the third term is the work done by the external forces and moments ( $W_{ext}$ ).  $\Delta E_m^\circ$  is the change in mechanical energy, and  $\Sigma_m^\circ$  is the dissipated mechanical energy in the system.

$$W_{act} + \int_{t_1}^{t_2} \sum_{j=1}^e \tau_j \dot{q}_j dt - W_{ext} = \Delta E_m^\circ + \Sigma_m^\circ \quad (\text{A.16})$$

By replacing for  $\int_{t_1}^{t_2} \tau_j \dot{q} dt$  from Eq. (A.14), Eq. (2.14) results:

$$W_{act} = W_{ext} + \Delta E_m^T + \Sigma_m^T + \Delta E_{cap} + \Sigma_e \quad (\text{A.17})$$

where  $\Delta E_m^T = \Delta E_m^\circ + \sum_{j=1}^e \Delta K_j$  is the total mechanical energy of the manipulator and actuators,  $\Sigma_m^T = \Sigma_m^\circ + \int_{t_1}^{t_2} \sum_{j=1}^e (b_j n_j^2) \dot{q}_j^2 dt$  is the total mechanical dissipation of the manipulator and actuators,  $\Sigma_e = \sum_{j=1}^e \int_{t_1}^{t_2} P_{Rj} dt$  is the electrical dissipation in the actuators, and  $\Delta E_{cap}$  is the total energy stored in the capacitors of the semi-active joints. Note that for the star configuration  $\Delta E_{cap} = \Delta E_s$  and for the distributed configuration  $\Delta E_{cap} = \sum_{j=1}^e \Delta E_{sj}$ .

## Optimum gear ratio

This section explains the derivation of Eq. (3.26). We start by substituting for  $\tau_j^d$  in the energy regeneration equation (Eq. (3.3)), from Eq. (3.2). Taking the derivative with respect to  $n_j$  results in

$$\begin{aligned} \frac{d\Delta E_{sj}}{dn_j} &= \int_{t_1}^{t_2} \left( 2m_j n_j \ddot{q}_j + \left( 2b_j n_j + \frac{2\alpha_j^2 n_j}{R_j} \right) \dot{q}_j \right) \dot{q}_j dt - \\ &\int_{t_1}^{t_2} \frac{2R_j}{\alpha^2} \left( \frac{(Y_j \theta + \mathcal{T}_j)}{n_j} + m_j n_j \ddot{q}_j + \left( b_j n_j + \frac{\alpha^2 n_j}{R_j} \right) \dot{q}_j \right) \\ &\times \left( \frac{-(Y_j \theta + \mathcal{T}_j)}{n_j^2} + m_j \ddot{q}_j + \left( b_j + \frac{\alpha^2}{R_j} \right) \dot{q}_j \right) dt = 0 \end{aligned} \quad (\text{A.18})$$

By factoring out  $1/n_j^3$  we have

$$\begin{aligned} &\frac{1}{n_j^3} \left( \int_{t_1}^{t_2} \left( 2m_j n_j^4 \ddot{q}_j \dot{q}_j + 2 \left( b_j + \frac{\alpha_j^2}{R_j} \right) \dot{q}_j^2 n_j^4 \right) dt \right. \\ &- \int_{t_1}^{t_2} \frac{2R_j}{\alpha^2} \left( Y_j \theta + \mathcal{T}_j + m_j n_j^2 \ddot{q}_j + \left( b_j + \frac{\alpha^2}{R_j} \right) \dot{q}_j n_j^2 \right) \\ &\left. \times \left( -Y_j \theta - \mathcal{T}_j + m_j \ddot{q}_j n_j^2 + \left( b_j + \frac{\alpha^2}{R_j} \right) \dot{q}_j n_j^2 \right) dt \right) = 0 \end{aligned} \quad (\text{A.19})$$

Since  $1/n_j^3 \neq 0$  the above equation can be simplified as

$$\begin{aligned} &\int_{t_1}^{t_2} \left( 2m_j n_j^4 \ddot{q}_j \dot{q}_j + 2 \left( b_j + \frac{\alpha_j^2}{R_j} \right) \dot{q}_j^2 n_j^4 \right) dt \\ &- \int_{t_1}^{t_2} \frac{2R_j}{\alpha^2} \left( \left( m_j \ddot{q}_j + \left( b_j + \frac{\alpha^2}{R_j} \right) \dot{q}_j \right)^2 n_j^4 - (Y_j \theta + \mathcal{T}_j)^2 \right) dt = 0 \end{aligned} \quad (\text{A.20})$$

From the above equation, the optimum gear ratio can be found as

$$n_j^4 = \frac{- \int_{t_1}^{t_2} \frac{2R_j}{\alpha^2} (Y_j \theta + \mathcal{T}_j)^2 dt}{\int_{t_1}^{t_2} 2m_j \ddot{q}_j \dot{q}_j + 2 \left( b_j + \frac{\alpha^2}{R_j} \right) \dot{q}_j^2 - \frac{2R_j}{\alpha^2} \left( m_j \ddot{q}_j + \left( b_j + \frac{\alpha^2}{R_j} \right) \dot{q}_j \right)^2 dt} \quad (\text{A.21})$$

## APPENDIX B

### SYSTEM MODELS

#### Double Pendulum and Cart System

The regressor matrix  $Y$  and the parameter vector  $\theta$  for the double inverted pendulum and cart system are given below using a shorthand notation for trigonometric functions ( $c_i = \cos(q_i)$ ;  $s_i = \sin(q_i)$ ;  $c_{ij} = \cos(q_i + q_j)$ ;  $s_{ij} = \sin(q_i + q_j)$ ).

$$Y = \begin{bmatrix} \ddot{q}_3 s_2 - g c_2 & Y_{12} & \ddot{q}_2 & Y_{14} & Y_{15} & 0 & \dot{q}_1 & 0 & 0 \\ 0 & Y_{22} & 0 & Y_{24} & Y_{25} & 0 & 0 & \dot{q}_2 & 0 \\ c_2 \dot{q}_2^2 + \ddot{q}_2 s_2 & Y_{33} & 0 & 0 & 0 & \dot{q}_3 & 0 & 0 & \ddot{q}_3 \end{bmatrix}$$

where  $Y_{12} = Y_{22} = g c_{12} - \ddot{q}_3 s_{12}$ ,  $Y_{14} = -s_2(\ddot{q}_2^2 - 2\dot{q}_1\dot{q}_2) + c_2(2\ddot{q}_1 + \ddot{q}_2)$ ,  $Y_{15} = \ddot{q}_3 s_1 - g c_1$ ,  $Y_{33} = -c_{12}(\dot{q}_1 + \dot{q}_2)^2 - s_{12}(\ddot{q}_1 + \ddot{q}_2)$ ,  $Y_{24} = s_2 \dot{q}_1^2 + c_2 \ddot{q}_1$  and  $Y_{1,5} = Y_{25} = \ddot{q}_1 + \ddot{q}_2$ .

$$\theta = \begin{bmatrix} \theta_1 & h_2 M_2 & \theta_3 & l_1 M_2 h_2 & \theta_5 & B_3 & B_1 & B_2 & \theta_9 \end{bmatrix}$$

where  $\theta_1 = h_1 M_1 - l_1(M_1 + M_2)$ ,  $\theta_3 = I_1 + M_1(l_1 - h_1)^2 + l_1^2 M_2$ ,  $\theta_9 = M_1 + M_2 + M_3$  and  $\theta_5 = M_2 h_2^2 + I_2$ .

## PUMA 500 Robot

The  $3 \times 10$  regressor matrix for the three main joints of the PUMA 500 robot (excluding the robot wrist) is given below where  $Y_{ij}$  is the  $i$ -th row and  $j$ -th column element of the regressor matrix,  $c_i = \cos(q_i)$ ,  $s_i = \sin q_i$ ,  $c_{ij} = \cos(q_i + q_j)$ , and  $s_{ij} = \sin(q_i + q_j)$ .

$$\begin{aligned}
 Y_{11} &= \ddot{q}_1 & Y_{25} &= \ddot{q}_1 s_{23} \\
 Y_{12} &= \ddot{q}_1 c_2^2 - 2\dot{q}_1 \dot{q}_2 c_2 s_2 & Y_{26} &= \ddot{q}_2 \\
 Y_{13} &= \ddot{q}_1 c_{23}^2 - 2\dot{q}_1 (\dot{q}_2 + \dot{q}_3) s_{23} c_{23} & Y_{27} &= \ddot{q}_3 \\
 Y_{14} &= 2(\ddot{q}_1 - \dot{q}_1 \dot{q}_2) c_{23} c_2 - 2(\dot{q}_1 \dot{q}_2 \\
 &\quad + \dot{q}_1 \dot{q}_3) s_{23} c_2 & Y_{28} &= \ddot{q}_1 s_2 \\
 Y_{15} &= (\dot{q}_2 + \dot{q}_3)^2 c_{23} + (\ddot{q}_2 + \ddot{q}_3) s_{23} & Y_{29} &= -c_{23} \\
 Y_{16} &= Y_{17} = Y_{19} = 0 & Y_{31} &= Y_{32} = Y_{36} = Y_{38} = 0 \\
 Y_{110} &= Y_{112} = Y_{113} = 0 & Y_{310} &= Y_{311} = Y_{312} = 0 \\
 Y_{18} &= \dot{q}_2^2 c_2 + \ddot{q}_2 s_2 & Y_{33} &= \dot{q}_1^2 s_{23} c_{23} \\
 Y_{22} &= \dot{q}_1^2 c_2 s_2 & Y_{34} &= \dot{q}_1^2 s_{23} c_2 + \dot{q}_2^2 s_3 + \ddot{q}_2 c_3 \\
 Y_{23} &= \dot{q}_1^2 c_{23} s_{23} & Y_{35} &= \ddot{q}_1 s_{23} \\
 Y_{21} &= Y_{211} = Y_{213} = 0 & Y_{37} &= \ddot{q}_2 + \ddot{q}_3 \\
 Y_{24} &= (c_{23} s_2 + s_{23} c_2) \dot{q}_1^2 - (2\dot{q}_3 \dot{q}_2 \\
 &\quad + \dot{q}_3^2) s_3 + (2\ddot{q}_2 + \ddot{q}_3) c_3 & Y_{39} &= -c_{23}
 \end{aligned}$$

The  $10 \times 1$  parameter vector  $\theta$  is given below, where  $M_i$  is the mass of the  $i$ -th robot link,  $I_{ij}$  is the moment of inertia of the  $i$ -th link with respect to the  $j$  axis of the coordinate frame located at the center of mass of link  $i$  and parallel to frame  $i$ ,  $C_{ij}$  is the distance from the center of mass of link  $i$  along the  $j$  axis of frame  $i$ , to the origin of frame  $i$ , and  $g$  is the gravity constant. Refer to Fig. 6 and Fig. 29a for the

definitions of the coordinate frames and other parameters.

$$\theta_1 = M_2 d_2^2 + M_3 (d_3 - d_2)^2 + I_{1y} + I_{2x} + I_{3x} + m_1 n_1^2$$

$$\theta_2 = M_2 (\mathcal{C}_{2x} + A_2)^2 + M_3 A_2^2 - I_{2x} + I_{2y}$$

$$\theta_3 = M_3 \mathcal{C}_{3x}^2 - I_{3x} + I_{3y}$$

$$\theta_4 = \mathcal{C}_{3x} A_2 M_3$$

$$\theta_5 = \mathcal{C}_{3x} M_3 (d_3 - d_2)$$

$$\theta_6 = M_2 (\mathcal{C}_{2x} + A_2)^2 + M_3 (\mathcal{C}_{3x}^2 + A_2^2) + I_{2z} + I_{3z} + m_2 n_2^2$$

$$\theta_7 = I_{3z} + M_3 \mathcal{C}_{3x}^2 + m_3 n_3^2$$

$$\theta_8 = -d_2 M_2 (\mathcal{C}_{2x} + A_2) + A_2 M_3 (d_3 - d_2)$$

$$\theta_9 = \mathcal{C}_{3x} g M_3$$

$$\theta_{10} = g M_2 (\mathcal{C}_{2x} + A_2) + A_2 g M_3$$